TECHNISCHE UNIVERSITÄT WIEN

ATOMINSTITUT

DIPLOMARBEIT

Time-resolved postselection and the violation of a Leggett–Garg inequality in thermal neutron interferometry

zur Erlangung des akademischen Grades

Diplom-Ingenieurin

im Rahmen des Studiums

Technische Physik

eingereicht von

Elisabeth Sophie Kreuzgruber
Matrikelnummer 1227350

ausgeführt am

Atominstitut
der Fakultät für Physik
der Technischen Universität Wien

unter der Anleitung von

Priv.-Doz. Dipl.-Ing. Dr. Stephan Sponar
Associate Prof. Dipl.-Ing. Dr. Yuji Hasegawa
Mag.rer.nat. Dr. Richard Wagner

Wien, am 05.09.2022

Unterschrift Verfasserin

Unterschrift Betreuer

Abstract

In 1974, H. Rauch successfully measured neutron interference fringes for the first time, using thermal neutrons and a single-crystal three-plate silicon interferometer at the Atominstitut in Vienna. This concept was developed further and found numerous applications in fundamental physics and material science. M. Zawisky et al. extended the original experiment by recording the additional information of neutron arrival times in 1995, presenting a technique for the enhancement of the interferometric contrast.

This thesis focuses on the expansion of these measurements, using an improved setup with small ^{3}He detectors in both the direct and the reflected beams, implementing a dedicated program on an FPGA card for the acquisition of arrival times, and taking measurements both at the Atominstitut as well as at S18 of the Institut Laue–Langevin (ILL) in Grenoble, France. Improved statistics and neutron count rates of a factor 10^2 higher than in Vienna allowed for a more precise determination of model parameters for interferograms both with and without arrival-time post-selection. The predicted contrast enhancement could be clearly shown with the measured data.

Furthermore, the setup at the ILL was used to investigate the violation of a Leggett–Garg inequality (LGI). This class of inequalities, introduced by A.J. Leggett and A. Garg in 1985, can be thought of as temporal Bell inequalities, and uses the postulates of macrorealism and non-invasive measurability. Since classical mechanics fulfill LGI whereas quantum mechanics violates it, these measurements present valuable insight into the limits between classical and quantum mechanics. Measurements for this thesis demonstrated the violation of a LGI with thermal neutrons for the first time.

Kurzfassung

1974 gelang H. Rauch am Reaktor des Atominstituts in Wien die erste erfolgreiche Aufzeichnung von Neutroneninterferenzkurven, unter der Verwendung eines Drei-Platten-Silizium-Einkristall-Interferometers mit thermischen Neutronen. Das Konzept der Neutroneninterferometrie wurde vielfach weiterentwickelt und fand Anwendungen in Grundlagenforschung und Materialwissenschaft. Das ursprüngliche Experiment wurde 1995 von M. Zawisky et al. um die zusätzliche Messung der Neutron-Ankunftszeiten ausgedehnt, was eine Methode zur Vergößerung des Kontrastes im Interferogramm durch Postselektion erlaubt.

Die vorliegende Arbeit erweitert diese Messungen mit einem verbesserten Setup, das kleine ^{3}He-Detektoren in sowohl direktem als auch reflektiertem Strahl sowie die automatisierte Aufnahme der Neutron-Ankunftszeiten beinhaltet. Die Messungen wurden sowohl am Atominstitut als auch am S18 des Institut Laue-Langevin (ILL) in Grenoble durchgeführt. Höhere Zählraten um einen Faktor 10^2 und verbesserte Statistik am ILL im Vergleich zu Wien erlaubten eine präzisere Bestimmung von Modellparametern sowohl mit als auch ohne Postselektion. Die vorhergesagte Kontrastverbesserung konnte mit den aufgenommenen Messdaten klar gezeigt werden.

Zudem wurden am ILL-Strahlplatz Messungen zur Untersuchung der Verletzung einer Leggett–Garg-Ungleichung (LGI) durchgeführt. Diese Klasse an Ungleichungen, 1985 von A.J. Leggett und A. Garg eingeführt, entspricht zeitlichen Bell–Ungleichungen und stützt sich auf Makrorealismus und nichtinvasive Messbarkeit. Da klassische Mechanik die LGI erfüllt, während Quantenmechanik sie verletzt, erlaubt eine Untersuchung Aufschluss über die Grenze zwischen klassischer und Quantenmechanik. Im Zuge der Messungen für die vorliegende Arbeit wurde eine Verletzung der LGI mit thermischen Neutronen erstmals gezeigt.

Abbreviations

ANuBIS	Austrian Neutron Beam Interferometer Station
CCD	Charge-coupled device
CDF	Cumulative distribution function
EPS	European Physical Society
ESS	European Spallation Source
FCC	Face-centered cubic
FPGA	Field programmable gate array
FWHM	Full width at half maximum
HFR	High-Flux reactor
ILL	Institut Laue–Langevin
LGI	Leggett–Garg inequality
LLL	Triple-Laue
MZI	Mach–Zehnder interferometer
nEDM	Neutron electric dipole moment
PMF	Probability mass function
SQUID	Superconducting quantum interference device
TRIGA	Training, Research, Isotope production, General Atomics

Table of Contents

1 Introduction

Matter-wave interferometry with neutrons is a powerful tool that allows the visualisation of the quantum nature of the neutron. Discovered in 1932 [1], the neutron is the second lightest baryon and electrically neutral, which, with its accessibility from reactors or spallation sources, lends itself to investigate quantum effects on matter. Neutrons are affected by all four fundamental interactions, giving rise to nuclear, gravitational and magnetic phase shifts in the neutron's wave function. These phase shifts can be observed by using neutron optical components in various experiments.

Neutron interferometry The first successful demonstration of neutron interference fringes was performed in 1974 at the Atominstitut in Vienna by H. Rauch et al. [2]. A three-plate single-crystal silicon interferometer was used to observe the self-interference of thermal neutrons, demonstrating matter-wave duality. During the macroscopic spatial separations achieved inside the interferometer, a neutron's wave function can be modified in phase and amplitude by applying different methods. Since 1974, many experimental improvements have been made and neutron interferometry has found a wide range of applications studying fundamental concepts of quantum mechanics. For instance, the neutron interferometer has been used to investigate the 4π spinor symmetry [3] and superposition [4, 5], scattering lengths of different materials [6, pp. 56–78], effects of magnetic fields [7], non-inertial frames [8], and to test the equivalence principle [9]. In more recent times, experiments addressing topics such as entanglement and weak values have been performed [10–14]. The original three-plate structure has been expanded to four and more plates, and, most recently, split crystal experiments [15].

Time-resolved measurements Rauch's original measurement opened up a new era of investigations concerning quantum phenomena using matter waves. In 1994, Zawisky et al. used the acquisition of neutron arrival time data on top of the total neutron counts in a given time interval, to allow the enhancement of fringe visibility (contrast) and the reduction of phase uncertainty in postselection. This is achieved via statistical manipulation, which utilises certain properties of the Poissonian distribution of neutrons from the reactor. The present work used an improved setup for postselection in not only the transmitted but also the reflected beam, smaller detectors, and more advanced software for higher time resolution in the recording of arrival times. These measurements were performed not only at the 'original' 250 kW reactor at the Atominstitut but also at the high-flux 58 MW reactor of the Institut Laue–Langevin (ILL) in Grenoble, France, where higher count rates and a more stable setup allowed for a more in-depth analysis of the behaviour of the postselected data.

Leggett–Garg inequality The Bell inequality is a well-known tool to investigate the limits between our everyday classical world and the quantum mechanical one. A similar ansatz, proposed by A. J. Leggett and A. Garg in 1985 [16], can be thought of as a Bell inequality on the time domain: the Leggett–Garg inequality (LGI). It is based on the two assumptions of macrorealism (that a system is always in a defined state, even between measurements) and non-invasive measurability (that it is in principle possible to determine the state of a system without disturbing it). These assumptions are obvious for the classical world, but as obviously contradicted by quantum mechanics. A violation of the LGI therefore implies a quantum mechanical system. In this thesis, such a violation is shown via the implementation of a non-50:50 beam splitter (first plate in the interferometer) by adding an absorber into one of the partial beams. Negative result measurements, which have been suggested by Garg [17] as a major improvement to current LGI tests, have been used. The experimental results obtained in this thesis mark the first violation of an LGI with neutrons.

The structure of this thesis Firstly, the main theoretical background for this thesis is given in CHAPTER 2. A short overview of neutrons, their sources and detections is followed by the basics of neutron interferometry with a three-plate perfect-crystal Si interferometer as well as counting statistics and the Poissonian distribution. Next, CHAPTER 3 describes the setup for the measurements both at the Atominstitut in Vienna and the ILL in Grenoble as well as the respective reactors and instrument components which were used.

Measurements are presented in two chapters, both with a theoretical introduction to the specific experiment: CHAPTER 4 for the time-resolved interferograms and the different results for selected short and long time intervals both in Vienna and in Grenoble which show a clear enhancement of the observed contrast, and lastly, CHAPTER 5 presents an outline of the LGI and the achieved violation, proving that the quantum system of the neutron interferometer is, indeed, quantum.

2 Theoretical background

In this chapter, an overview over the theoretical background in neutron interferometry is given. First, properties of the neutrons itself are discussed, followed by a discussion of triple-Laue interferometry. An introduction to counting statistics is presented as well.

2.1 Neutron physics

2.1.1 Properties of the neutron

The neutron was discovered by J. Chadwick in 1932 [1]. It consists of three quarks, one up and two down quarks, thus belonging to the hadron family in the standard model of particle physics, more precisely, the baryons. With the electric charges of $2/3\,e$ for the up quark and $-1/3\,e$ for each of the two down quarks, the net electric charge of the neutron results to 0. This has been confirmed by charge measurements that lead to values of $-0.2 \pm 0.8 \times 10^{-21}\,e$ [18].

As a fermion, the neutron has a spin of $\frac{1}{2}$. The neutron has a magnetic moment of $\mu_\mathrm{n} = -9.662 \times 10^{-27}\,\mathrm{JT}^{-1}$ and a mass of $m_\mathrm{n} = 1.675 \times 10^{-27}\,\mathrm{kg}$ or $939.6\,\mathrm{MeV/c^2}$ [19]. However, the free neutron is not stable. With a mean life time of $879.4 \pm 0.6\,\mathrm{s}$ [18], it decays into a proton (which has a lower rest mass of $938.3\,\mathrm{MeV/c^2}$ [19]), an electron and an electron antineutrino with the reaction [20]

$$\mathrm{n} \rightarrow \mathrm{p}^+ + \mathrm{e}^- + \bar{\nu}_\mathrm{e} + 0.78\,\mathrm{MeV}\,. \tag{2.1}$$

Due to the negative charge of the emitted β particle (i.e. the electron), this process is called the β^- decay. Another interesting property is the Neutron electric dipole moment (nEDM), as its existence would violate CP symmetry. The current upper limit on the nEDM is $|d_\mathrm{n}| < 3.0 \times 10^{-26}\,e\,\mathrm{cm}$ [18] at 90% CL.

The neutron is subjected to all four of the fundamental forces: the strong force, due to its composition of quarks; the weak force, as can be seen from the β^- decay in eq. (2.1); the electromagnetic force due to its magnetic moment μ_n; and gravity, since it has mass.

In his 1924 PhD thesis [21], Louis de Broglie suggested a duality between matter-like and wave-like behaviour for quantum-scale objects. The relation between the momentum of a particle and the wavelength of the respective matter wave is given as

$$\lambda = \frac{h}{p} = \frac{h}{\sqrt{2mE}}\,, \tag{2.2}$$

with Planck's constant $h = 6.626 \times 10^{-34}\,\mathrm{J\,s}$ [19] and taking into account that for a nonrelativistic

particle of mass m, its energy can be expressed as $E = \frac{p^2}{2m}$. The kinetic energy of a neutron is calculated according to [6]

$$E = \frac{m v_p^2}{2} = k_\mathrm{B} T \,, \tag{2.3}$$

with Boltzmann's constant $k_\mathrm{B} = 8.617 \times 10^{-5}\,\mathrm{eV\,K^{-1}}$ [19] and the velocity v_p the mode of the Maxwell–Boltzmann distribution[1] at temperature T. It is convention [22, p. 4, 6, p. 3] to use the mode (i.e., the most probable velocity) as opposed to the mean square velocity $\langle v^2 \rangle$, which would result in the more familiar $E = \frac{3}{2} k_\mathrm{B} T$.

At room temperature (20 °C), the neutron energy results in $E \simeq 25\,\mathrm{meV}$, corresponding to a wavelength of $\lambda = 1.8\,\text{Å}$ and a velocity of about $2.2\,\mathrm{km\,s^{-1}}$. These are the so-called 'thermal' neutrons that this thesis will focus on. TABLE 2.1 gives an overview of different neutron energy ranges and their corresponding classifications.

TAB. 2.1 – Overview of the neutron energy ranges and their respective classifications. This compilation uses values taken from references [20], [23], and [24].

Classification	Energy range
fast	$> 1\,\mathrm{MeV}$
intermediate	$100\,\mathrm{eV} - 1\,\mathrm{MeV}$
resonance	$1 - 100\,\mathrm{eV}$
slow	$< 1\,\mathrm{eV}$
epithermal	$25\,\mathrm{meV} - 1\,\mathrm{eV}$
thermal	$\simeq 25\,\mathrm{meV}$
cold	$< 25\,\mathrm{meV}$
ultra cold	$\lesssim 300\,\mathrm{neV}$

2.1.2 Neutron sources

There are three possible sources for free neutrons: nuclear reactions, nuclear fission in reactors and spallation. Due to the aforementioned limited lifetime of about 15 min, each experiment has to be reasonably close to the corresponding neutron source.

2.1.2.1 Nuclear reactions

In FIG. 2.1, the binding energy per nucleon E_B/A is depicted over increasing nucleon number A. The peaks in this curve for low values of A indicate more strongly bound nuclei, for example the α particle ^{4}He, ^{8}Be or ^{12}C. Adding another particle to such a nucleus upsets this balance, resulting in loosely bound neutrons. The collision energy of such nuclides with fast protons, neutrons or α particles as well as γ rays can induce nuclear reactions and separate these neutrons. An example for such a nuclide is the only stable beryllium isotope ^{9}Be, which has a high cross section for (α,n) reactions. The reaction

$$^9\mathrm{Be} + \alpha \rightarrow {}^{12}\mathrm{C} + \mathrm{n} + 5.71\,\mathrm{MeV} \tag{2.4}$$

results in a continuous neutron spectrum from 0 to 13 MeV with a mean around 5 MeV. In neutron sources, ^{9}Be is commonly combined with α emitters such as ^{210}Po or ^{241}Am [20, 25].

[1] $f(v)\,\mathrm{d}v = \sqrt{\frac{m\beta}{2\pi}}^3 4\pi v^2\, \mathrm{e}^{-\beta\frac{mv^2}{2}}\,\mathrm{d}v$ with $\beta = \frac{1}{k_\mathrm{B}T}$. The mode v_p is calculated from $\frac{\mathrm{d}f(v)}{\mathrm{d}v} \stackrel{!}{=} 0 \Rightarrow v_p = \sqrt{\frac{2k_\mathrm{B}T}{m}}$.

These sources are mostly used for detector calibration due to their rather low flux in comparison to other sources.

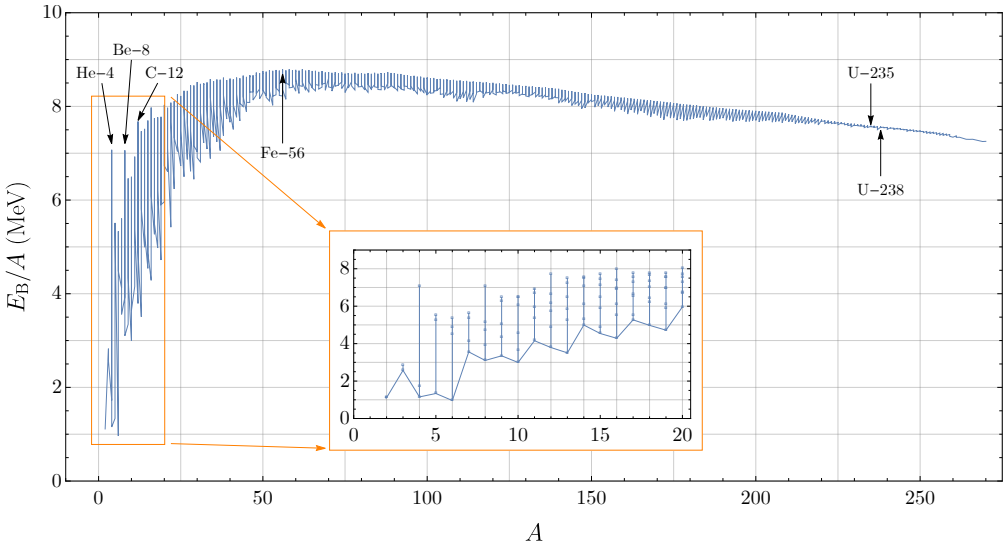

FIG. 2.1 – Binding energy per nucleon in MeV. Significant nuclei are indicated: fusionable nuclei lie to the left, fissionable nuclei to the right of the most tightly bound nucleus ^{56}Fe. The inset shows details of the peaks for small nucleon numbers A. Data taken from [26].

2.1.2.2 Nuclear fission

The binding energy per nucleon (FIG. 2.1) shows a maximum for ^{56}Fe, meaning that nuclei to the left can gain energy through fusion, and nuclei on the right through nuclear fission. In a neutron-induced fission process of a heavy element, the incoming neutron deposits its kinetic energy inside the nucleus, which starts to oscillate and finally ruptures due to the proton-proton repulsion. The products of this breaking process are mostly two smaller nuclei and 2–3 additional neutrons due to the higher abundance of neutrons with respect to protons for heavier nuclei. Since the excess binding energy of the mother nucleus is released into kinetic energies of the fission products, resulting neutron velocities are high: around 5 MeV in total are divided among the neutrons.

In order to maintain this chain reaction, the neutrons have to be moderated (i.e. slowed down via a number of inelastic collisions) to the thermal range. Nuclear research reactors typically use ^{235}U as fuel, where the average neutron yield for incoming thermal neutrons is 2.43. These neutrons then either decay, leave the reactor or can induce a fission process in one of the other surrounding fissile ^{235}U nuclei. The majority of the outcoming neutrons are so-called 'prompt' neutrons, emitted immediately (as opposed to 'delayed' neutrons which are emitted after a preceding β decay of the daughter nucleus of the chain reaction), and their spectrum can be approximated by a Maxwell–Boltzmann distribution [27].

In this thesis only neutrons obtained in continuous mode were used, although the operation of a reactor is possible both in continuous and in pulsed mode. The research reactors at which the measurements in this thesis were performed are described in SEC. 3.1 for the TRIGA reactor at the Atominstitut TU Wien and SEC. 3.2 for the High-Flux reactor (HFR) of the Institut Laue–Langevin (ILL) in Grenoble.

2.1.2.3 Spallation

In a spallation neutron source, a proton beam with high kinetic energy is shot onto a target. This target which constitutes the actual neutron source, an atomic nucleus, shatters into many small particles. Among them are several fast neutrons, which are then slowed down. For the target itself, tungsten is most commonly used, due to the high neutron yield per incoming proton. Aside from the target, the most important component of a spallation source is the accelerator which generates the fast proton beam. This accelerator can be a linear accelerator (as in the European Spallation Source (ESS), which is currently under construction in Sweden), a synchrotron in combination with a linear accelerator (as in the ISIS neutron source in the United Kingdom), or a cyclotron (as in the Paul Scherrer Institute in Switzerland). Due to the nature of the acceleration process, spallation sources are operated in pulsed mode [28].

2.1.3 Neutron detection

To reliably detect neutrons, materials with high cross sections for (n,$*$) reactions with prompt energetic charged particles are used. Since these reactions capture the incoming neutron, they are classified by the neutron absorption cross section σ_a. In an active detection device, a target (for example a counting gas) serves as conversion medium for the neutron, and the resulting current signal or pulse is read out by a detector.

A critical feature in neutron detection is the ability of discrimination of the γ radiation background. For this, the Q-value, which determines the amount of energy released by the reaction following a neutron capture, is a good indicator: the higher the Q-value, the more kinetic energy is transferred to the products of the reaction and the easier the amplitudes can be separated from background events. Detector geometry is equally important, as the reaction products need to be able to deposit their entire energy within the detector volume, otherwise leading to the so-called 'wall-effect' which shifts the pulse spectrum towards lower energies [29, pp. 505–506]. In addition, size and gas pressure influence the efficiency of a neutron detector.

In the following sections, the three main modes of slow neutron detection – (n,α) reactions for ^{10}B and ^{6}Li as well as the (n,p) reaction for ^{3}He – are discussed, each followed by a more detailed description of the behaviour for thermal neutrons. The behaviour of the neutron detection cross sections σ_a of these three reactions over a wide range of neutron energies are shown in FIG. 2.2. Since σ_a depends strongly on the energy of the incoming neutron, a slow neutron detector will not provide satisfying results for neutrons of higher energies. See [29, pp. 537–576] for a discussion of detectors for intermediate and fast neutrons.

2.1.3.1 ^{10}B-based detectors

The first kind of commonly used neutron detectors are BF_3 counting tubes, comprising a cylindrical outer cathode and inner wire anode. A schematic of a simple counting tube is shown in FIG. 2.3. In these detectors, boron triflouride is both the target and the counting gas, using the reaction

$$^{10}\mathrm{B} + \mathrm{n} \rightarrow {}^{7}\mathrm{Li} + \alpha + Q\,, \tag{2.5}$$

where Q is 2.792 MeV for the ground state, and 2.310 MeV for the excited state ^{7}Li*, which decays to the ground state via the emission of a γ ray with a half-life of $\sim 10^{-13}$ s. This γ escapes and does not contribute to the detector response. The cross section σ_a shows a $1/v$ behaviour for the velocity of the incoming neutron v, and is 3840 b for thermal neutrons [29, p. 507].

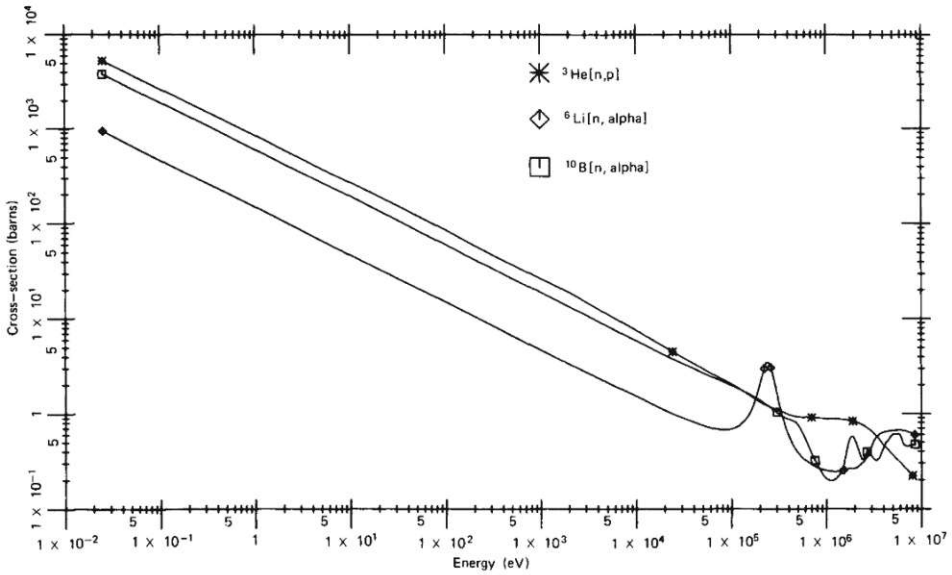

FIG. 2.2 – Detection cross section versus neutron energy for the most common materials used in neutron detectors [29, p. 508].

Due to the aforementioned wall-effect, which at typical pressures in BF_3 counting tubes plays an important role, the pulse height spectrum shows a continuum and therefore gives no information except of the detector geometry. The counting gas is enriched in ^{10}B and can be mixed with other gases (for example argon) to the effect of a much more stable counting behaviour and sharper pulse height spectrum at the expense of lowered efficiency. For thermal neutrons, the efficiency of these types of detector lies around 92 %. The discrimination against ionising γ rays is possible with an amplitude discriminator because BF_3 has low stopping power for possibly created secondary electrons. At high γ rates, however, discrimination problems can arise due to pulse pile-up [29, pp. 509–515].

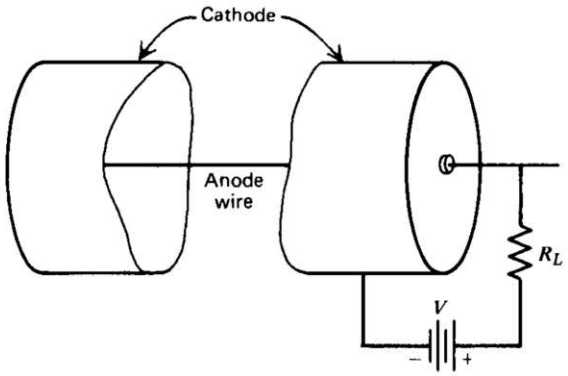

FIG. 2.3 – Schematic of a counting tube consisting of anode wire and cylindrical outer cathode, with load resistance R_L and high voltage V. Picture taken from [29, p. 162].

2.1.3.2 ^{6}Li-based detectors

Though the cross section for the ^{6}Li(n,α)^{3}H reaction lies below σ_a for the boron reaction, as can be seen in FIG. 2.2, lithium-based detectors have the advantage of a higher Q-value, making discrimination against γ rays easier. The resulting triton is always in the ground state, meaning a single peak in the pulse height spectrum as opposed to two peaks in the boron reaction. The reaction itself is

$$^6\mathrm{Li} + \mathrm{n} \rightarrow {}^3\mathrm{H} + \alpha + Q\,, \tag{2.6}$$

with $Q = 4.78\,\mathrm{MeV}$ and a thermal neutron cross section of 940 b [29, pp. 507–508].

There is no stable ^{6}Li-containing proportional gas, so there is no direct equivalent to the BF_3 counting tube. Instead, scintillators containing ^{6}Li are used, for example in thin layers of LiF and ZnS(Ag). γ ray discrimination is very effective in thin layers, since the electrons can escape without depositing all of their energy [29, pp. 517–518].

2.1.3.3 ^{3}He-based detectors

Another gas counting tube uses ^{3}He with the reaction

$$^3\mathrm{He} + \mathrm{n} \rightarrow {}^3\mathrm{H} + \mathrm{p} + Q\,, \tag{2.7}$$

where $Q = 0.765\,\mathrm{MeV}$ and a cross section of 5330 b for thermal neutrons. This cross section also shows the $1/v$ behaviour like σ_a for boron, and though it is significantly larger, the high cost of ^{3}He compared with BF_3 makes this less readily available [29, pp. 508–509].

Like for the BF_3 detectors, ^{3}He detectors also show a wall-effect continuum in their pulse height spectrum; even more distinct due to the lower atomic mass. Methods to circumvent this problem are using larger counting tube diameters or higher gas pressures within the tube. Compared with BF_3 detectors, ^{3}He detectors are therefore operated at much higher gas pressures. γ ray distinction is also more difficult than for BF_3 detectors because of the lower Q value. Therefore, Ar or CO_2 can be added into the counting tube to speed up electron drift times and as a result allow shorter shaping time in the processing electronics. Since ^{3}He only acts as an acceptable proportional counter gas when it has sufficient purity, measures must be taken to prevent leaks and the subsequent contamination of the counting gas [29, pp. 518–520].

2.1.4 Neutron absorption

The scattering length b in neutron-nucleus reactions is a complex number, with the real part describing the scattering, and the imaginary part describing the absorption. Expressed as a reaction cross section σ_t, this leads to $\sigma_t = \sigma_s + \sigma_a$, with σ_s and σ_a the scattering and absorption cross sections, respectively. For strong absorbers, b will have a large imaginary part, while for silicon, absorption can be neglected since $\sigma_a \ll \sigma_s$ [30, p. 4, 22, p. 9].

When a neutron beam passes through a material, its intensity is diminished according to the Beer–Lambert law

$$I(d) = I_0\,\mathrm{e}^{-\Sigma d}\,, \tag{2.8}$$

where I_0 is the initial beam intensity, d the thickness and Σ the macroscopic cross section of the absorber material. This macroscopic cross section can be expressed as

$$\Sigma = \sigma_t N = \sigma_t \frac{\rho}{M} N_A\,, \tag{2.9}$$

with N the number density, ρ the density and M the molar weight of the material, and $N_A = 6.022 \times 10^{23}\,\mathrm{mol}^{-1}$ [6, p. 60]. The following sections discuss beam intensity diminution for neutron shielding and for controlled beam attenuation.

2.1.4.1 Shielding

To shield the experimental setup from unwanted neutrons, materials with high σ_a are used. This can be for example concrete, paraffin, heavier elements like lead or tungsten, steel, and boron-containing materials. Since the various cross sections depend strongly on the energy of the incident neutron, moderation effects have to be taken into account, as well as the possibility of γ rays resulting from the neutron capture process, making layering of absorbers important [29, pp. 770–771]. As an example, paraffin stops thermal neutrons but slows down fast neutrons.

Thermal neutrons are stopped by cadmium, whereas fast neutrons will pass through it without being moderated [27, p. 63]. At around 0.5 eV, σ_a in ^{113}Cd drops rapidly – the so-called Cadmium cut-off, a border between slow and fast neutrons (see also TAB. 2.1) [29, p. 505]. With a molar weight of $M_{Cd} = 112.41\,g\,mol^{-1}$, density of $\rho_{Cd} = 8.69\,g/cm^3$ [31] and the cross sections for thermal neutrons $\sigma_{a,Cd} = 2520\,b$, $\sigma_{s,Cd} = 6.5\,b$ [32], the macroscopic cross section of cadmium becomes $\Sigma_{Cd} = 117.32\,cm^{-1}$. A cadmium sheet with a thickness of 1 mm reduces the initial intensity of a thermal neutron beam to 8.1×10^{-6}. Cadmium therefore effectively blocks thermal neutron beams.

2.1.4.2 Beam attenuation

In a neutron experiment, not only a complete shielding but also the controlled attenuation of a neutron beam can be important. Generally, one distinguishes between stochastic and deterministic absorbers. In a stochastic absorber, every neutron can in principle be absorbed, for example, in a foil like indium. As a consequence, the intensity in the neutron beam is diminished. In a deterministic absorber, only neutrons within a specific time or space interval are absorbed, for example, a rotating chopper disc or absorbing lattice [6, pp. 122–126].

For indium, with cross sections for thermal neutrons of $\sigma_a = 193.8\,b$, $\sigma_s = 2.6\,b$ [32], $M = 114.82\,g\,mol^{-1}$, and density of $\rho = 7.31\,g/cm^3$ at 20 °C [31], the macroscopic cross section results in $\Sigma = 7.43\,cm^{-1}$. When passing through an indium foil with a thickness of 1 mm, an incoming thermal neutron beam is diminished to 47.1%. Indium is a practically available candidate for the controlled reduction of neutron beam intensity.

2.2 Neutron interferometry

When a monochromatic wave of wavelength λ hits a perfect solid crystal, it is scattered by the atoms in the crystal lattice. Beams reflected in the different lattice planes travel paths of different lengths and they acquire a phase shift. This situation is illustrated in FIG. 2.4.

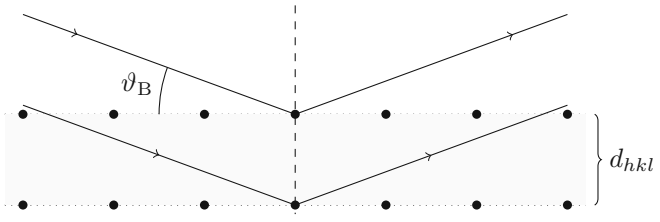

FIG. 2.4 – Bragg diffraction: incoming waves are scattered by crystal lattice atoms.

Bragg's formula

$$n\lambda = 2\, d_{hkl} \sin \vartheta_{\mathrm{B}} \tag{2.10}$$

is the well-known condition for constructive interference in the reflected beams. Here, d_{hkl} designates the interplanar distance of the crystal lattice (with h, k, l being the Miller indices), ϑ_{B} is the angle of incidence, and n a counting index. In case of matter waves, the wavelength λ is given by the de Broglie wavelength. Only neutrons with a specific wavelength will fulfill the condition for constructive interference. This behaviour is used in monochromators, when the selection of a certain wavelength is needed.

Depending on the position of the reflected beam compared to the incoming beam, one can distinguish between two cases: Bragg and Laue geometries. In the Bragg case, only the transmitted beam passes through the material (see FIG. 2.4). Laue diffraction refers to the case that the transmitted and reflected beam both pass through the crystal, leaving it on the opposite side from the incoming beam. Perfect crystal interferometry uses Laue geometry. The designations 'O' and 'H' beam have been established for the transmitted and reflected beams. Equivalent to the Bragg equation (2.10), the Laue condition can be formulated as

$$\Delta\vec{k} = \vec{k}_{\mathrm{H}} - \vec{k} = \vec{G}\,, \tag{2.11}$$

where the scattering vector $\Delta\vec{k}$, which describes the change between the incoming ($\vec{k}$) and reflected ($\vec{k}_{\mathrm{H}}$) wave vector, must equal the reciprocal lattice vector $\vec{G}$. $\vec{G}$ contains the Miller indices, as it can be written as $\vec{G} = h\vec{g}_1 + k\vec{g}_2 + l\vec{g}_3$ with the primitive reciprocal lattice vectors $\vec{g}_i$.

An illustration of the Laue geometry is presented in FIG. 2.5. γ and γ_{H} denote the angles of the symmetry axis to the incoming ($\vec{k}$) and reflected ($\vec{k}_{\mathrm{H}}$) wave, respectively [30, p. 16].

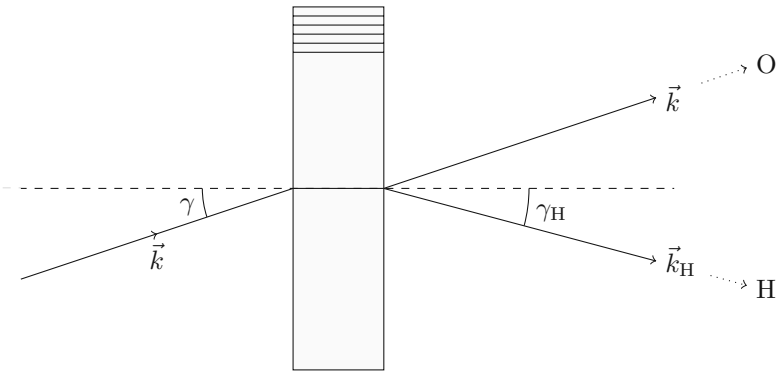

FIG. 2.5 – Laue geometry: both reflected and transmitted beam pass through the crystal. Crystal planes (horizontal lines) are indicated.

2.2.1 The perfect silicon crystal interferometer

In general, two kinds of neutron interferometry are possible: wave-front division (as in Young's type interferometers) and amplitude division (as in a Mach–Zehnder interferometer (MZI)). This thesis discusses the latter type, realised in a perfect silicon crystal three-plate interferometer in Triple-Laue (LLL) geometry. Interferometers of monolithic structures, produced from silicon perfect crystals cut out of a single ingot, allow for a precise lattice plane alignment. Due to the advances of semiconductor technology, the production of such devices is made possible: first, the rough structure of three vertical plates, connected by a common base, is cut from the perfect crystal, followed by a chemical etching process to remove cutting-induced lattice damage. A detailed description of the preparation process can be found in literature [33].

Silicon crystal has a diamond cubic structure with eight atoms per unit cell and belongs to the $Fd\bar{3}m$ space group. It can be understood as the overlay of an Face-centered cubic (FCC) unit cell with a second one shifted by $\frac{1}{4}$ along the space diagonal. This structure is depicted in FIG. 2.6, with conventional and primitive unit cell to the left and in the centre, with the lattice vectors $\vec{a}_i$ shown in red. The right-hand side emphasises the initial FCC unit cell (starting at the grey atom) and the shifted unit cell (starting at the red atom). Silicon has a lattice constant a_{Si} of 5.43 Å [31].

The setup for this thesis uses the $\{2,2,0\}$ reflection of this lattice, with $d_{220} = \frac{1}{\sqrt{8}} a_{\mathrm{Si}} = 1.92\,\text{Å}$. The advantage of this choice is that all the atoms in the unit cell partake in the reflection, with no additional atoms acting as perturbators. In FIG. 2.7, the unit cell (left) and top view with Bragg angle ϑ_{B} and planes $\{2,2,0\}$ and $\{1,1,0\}$ (which is a subset of $\{2,2,0\}$) are shown, as well as an illustration of the fact that not all atoms in the unit cell take part in $\{1,1,1\}$ reflections (on the right).

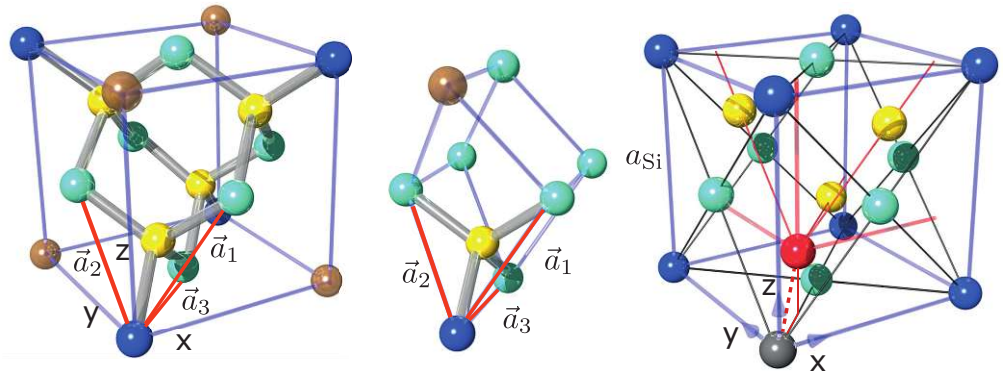

FIG. 2.6 – Unit cell of the Si crystal (left) and primitive cell (centre) with lattice vectors $\vec{a}_i$ shown in red. Right: overlay of first unit cell (starting point in grey) and second (starting point in red), which is shifted along the space diagonal (dashed red line).

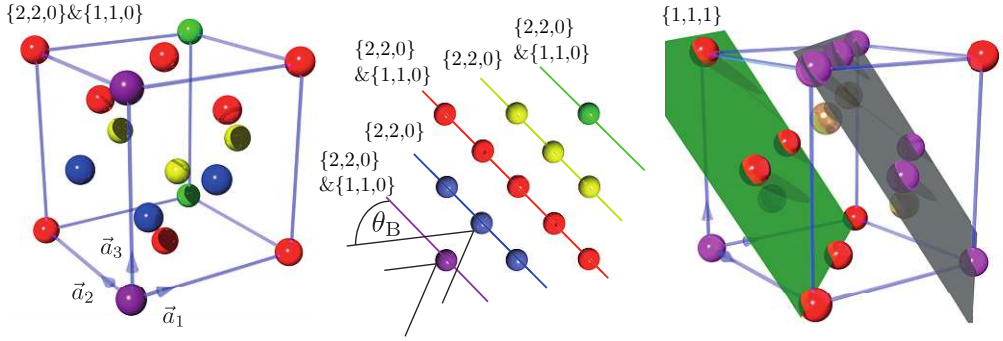

FIG. 2.7 – Reflection planes in the Si crystal: unit cell (left), top view of the unit cell with $\{1,1,0\}$ and $\{2,2,0\}$ planes (centre). Right: not all unit cell atoms take part in $\{1,1,1\}$ reflections.

Typical setup values in neutron interferometry are a plate thickness of a few mm and a length of 10 to 15 cm. A coherent beam separation of around 5 cm can be reached in the interferometer. Interferometry with cold neutrons and other materials used for beam handling is possible as well (see [6, pp. 39–46] for further discussion).

The operating principle of the LLL interferometric setup is displayed in FIG. 2.8. For each of the three plates, a beam split ratio of 50:50 is assumed. At the first plate, the 'splitter', the incoming neutron beam (ψ_0) is split into two parts, where the transmitted beam is designated 'path I' (ψ_I) and the reflected beam 'path II' (ψ_II). The second plate, or 'mirror', reflects the beams, and the transmitted fraction leaves the interferometer. Finally, at the third plate, or 'analyser', the partial beams are recombined and interfere. Detectors in O and H direction measure the resulting intensities. An additional homogeneous slab as a phase flag in both paths introduces a phase shift that differs for the two partial beams. Upon rotating the phase flag, interference fringes become visible.

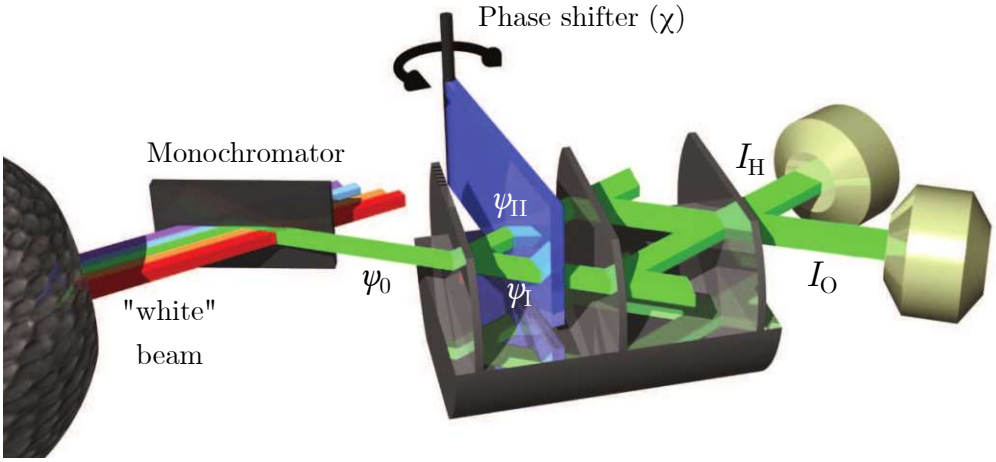

FIG. 2.8 – Schematic representation of the triple-Laue interferometer. The monochromatised incoming wave ψ_0 (left) is split into a transmitted wave ψ_I and a reflected wave ψ_II. After the interferometer, intensities I_O and I_H are measured by the detectors (right).

It is important to emphasize that neutron interferometry is single-particle interference. The time between two neutron counts in the detector is much longer than the time it takes a neutron to pass through the interferometer, so that at almost any given instance only a single neutron is inside the interferometer. At sources with low count rates, like the reactor of the Atominstitut Vienna, this is clearly verified. Interference fringes appear because the partial waves of the two possible neutron paths ψ_I, ψ_II form a superposition. This shows the wave-like properties of the neutron as described in the framework of quantum mechanics. The neutron interferometer thus constitutes a rather simple system that allows to investigate fundamental quantum mechanical behaviour.

2.2.1.1 Interferometric contrast

The waves in the two paths show a fundamental asymmetry [6, p. 27]. Waves arriving in the O detector both experience reflection (r) twice and transmission (t) once, giving a total intensity of

$$I_\mathrm{O} = |\psi_\mathrm{I,O} + \psi_\mathrm{II,O}|^2 = \left|trr\,\psi_0\,\mathrm{e}^{\mathrm{i}\chi_1} + rrt\,\psi_0\,\mathrm{e}^{\mathrm{i}\chi_2}\right|^2 , \tag{2.12}$$

with the amplitude of the incident wave ψ_0 and phases χ_i. In the H detector, however, the wave in path I experiences two transmissions and one reflection, while the wave in path II is reflected three times, giving an intensity

$$I_\mathrm{H} = |\psi_\mathrm{I,H} + \psi_\mathrm{II,H}|^2 = \left|trt\,\psi_0\,\mathrm{e}^{\mathrm{i}\chi_1} + rrr\,\psi_0\,\mathrm{e}^{\mathrm{i}\chi_2}\right|^2 . \tag{2.13}$$

With the definition of the difference between the acquired phases of the two beams, $\chi = \chi_2 - \chi_1$, the resulting intensities can be written as

$$\begin{aligned} I_{\mathrm{O}}(\chi) &= A\,(1 + \cos\chi) \\ I_{\mathrm{H}}(\chi) &= B - A\cos\chi\,, \end{aligned} \tag{2.14}$$

where $A = 2\,|\psi_0|^2|t|^2|r|^4$ and $B = |\psi_0|^2\left(|t|^4|r|^2 + |r|^6\right)$. Due to particle conservation, $I_{\mathrm{O}} + I_{\mathrm{H}} =$ const. [6, p. 27]. A derivation for eq. (2.14) is given in SEC. A.1.

This phase difference χ between the two beams is induced by a phase flag which extends over both partial beams and is rotated about a vertical axis outside the interferometer by angle δ. ψ_{I} and ψ_{II} therefore acquire slightly different phase shifts χ_i. For a phase flag of thickness D_{PS}, particle density N and coherent scattering length of the nuclei b_{c}, χ is calculated as

$$\chi = -N b_{\mathrm{c}}\, D_{\mathrm{PS}}\, \lambda = (n-1)\, k\, D_{\mathrm{PS}}\,, \tag{2.15}$$

with $\lambda = 2\pi/k$ the wavelength of the incoming neutron beam and the complex index of refraction [6, p. 10]

$$n = 1 - \frac{1}{2\pi}\lambda^2\, N b_{\mathrm{c}}\,. \tag{2.16}$$

For small phase flag rotation angles with respect to an orientation parallel to the interferometer plates, the absolute path length difference for the beams,

$$\Delta D(\eta) = \left(\frac{1}{\cos(\theta_{\mathrm{B}} + \eta)} - \frac{1}{\cos(\theta_{\mathrm{B}} - \eta)}\right) D_{\mathrm{PS}}\,, \tag{2.17}$$

is nearly linear in η. That is, the phase shifter position is proportional to the phase shift χ [6, 34].

In a non-ideal MZI, it is useful to introduce an additional quantity to qualify its function, the contrast, or fringe visibility, C. It is smaller than unity due to unavoidable imperfections in the experimental setup, caused by the weight of the interferometer itself, possible lattice defects, and external influences like vibrations or fluctuations in the surrounding temperature during a measurement. A discussion of the behaviour interferometric contrast under different external influences can be found in [35]. The intensity in the detector can then be written as [36]

$$I(\chi) = \bar{I}\,(1 + C\cos\chi)\,, \tag{2.18}$$

with the mean intensity $\bar{I}$ modulated by a cosine term weighted by C. This contrast is defined via the maximum and minimum intensity, $I_{\max}$ and $I_{\min}$, respectively, as

$$C = \frac{I_{\max} - I_{\min}}{I_{\max} + I_{\min}}\,. \tag{2.19}$$

For the O detector, this quantity could in theory reach $C = 1$, since the symmetry of the beam paths of the partial beams allows for a complete cancellation of the intensity. Due to the asymmetry of the beam paths, however, the contrast in the H detector cannot reach $C = 1$, even in a hypothetical ideal interferometer. This issue is shown in FIG. 2.9: due to the different number of reflections and transmissions in the two paths for the H detector (eq. (2.13); shown in orange), the partial waves can never fully interfere destructively, resulting in a larger mean intensity than the O detector (eq. (2.12); shown in blue), where complete destructive interference is possible (for an ideal MZI).

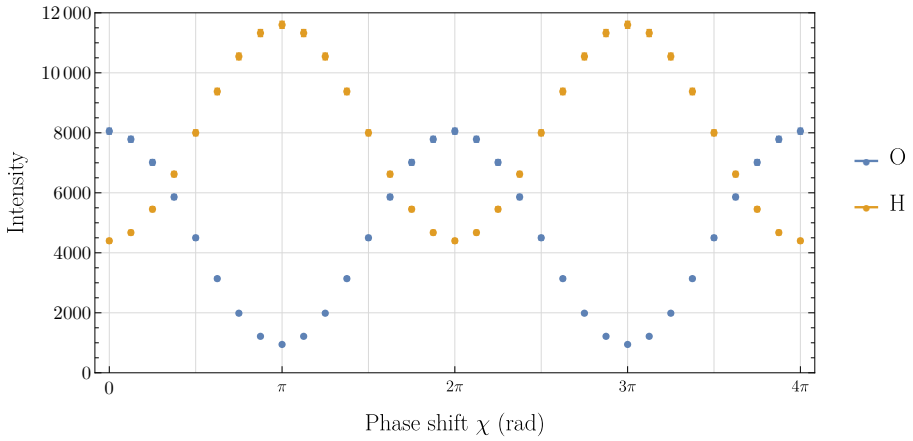

FIG. 2.9 – Simulation of interference curves in a non-ideal MZI. Blue points denote the O detector, orange points the H detector.

2.2.1.2 Neutron interferometer with blocked paths

If one of the two paths within the interferometer is blocked, for example with a cadmium foil (see FIG. 2.10), the interference fringes vanish, since there are no longer two wave amplitudes that can overlap. In order for the neutron to reach a detector, it has to take the unblocked path and a superposition of both paths does not exist anymore.

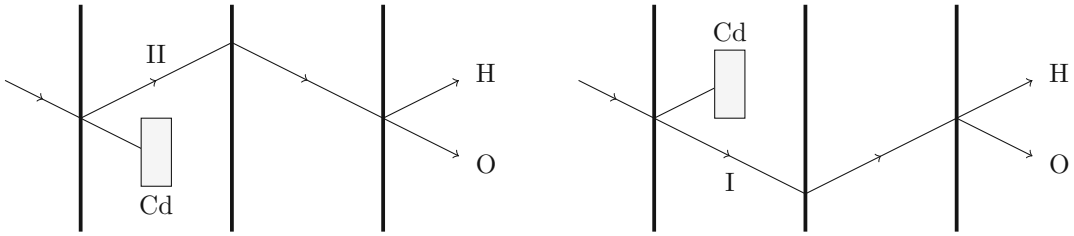

(A) Cadmium blocker in path I. (B) Cadmium blocker in path II.

FIG. 2.10 – Mach–Zehnder interferometer with one of the paths blocked. Neutrons have to take the other path in order to reach one of the detectors O or H.

Depending on which of the two paths is blocked, the ratio of the counting rates in both detectors changes, due to the aforementioned asymmetry in the number of reflections and transmissions.

TAB. 2.2 – Detection intensities for blocked paths in the neutron interferometer, normalised to the total intensity in the empty interferometer [37].

	O beam	H beam	O + H beam
empty interferometer	9/16	7/16	1
path I blocked	9/64	15/64	3/8
path II blocked	9/64	31/64	5/8

In TAB. 2.2, results of the detected intensities for blocked paths in an interferometer with three plates of exactly the same thickness are presented. A detailed analysis of neutron wave behaviour

in the interferometer is possible with the methods of dynamical diffraction theory. As a further discussion lies beyond the scope of this thesis, please refer to [30, 37]. Also see SEC. A.2 for a short overview of reflection curves in a MZI.

2.2.2 Applications of neutron interferometry

Applications of neutron interferometry include tests of gravitational effects on elementary particles (the Colella-Overhauser-Werner experiment [9]), 4π spinor symmetry [3] and superposition of fermion spins [4, 5] as well as the determination of scattering lengths of different materials [6, pp. 56–78]. Intra-particle entanglement (e.g. spin-particle entanglement) [38, 39], the quantum Cheshire Cat effect, [14] and other weak value measurements [10–13] have also been realised.

In this thesis, two experiments are discussed: the enhancement of interferometric contrast via the use of neutron arrival time information (CHAPTER 4), and the violation of a Leggett–Garg inequality (CHAPTER 5).

2.3 Counting statistics

In a neutron counting experiment, we are interested in the binary process whether a neutron is or is not detected at a given time. These events (detections) can be modelled with the Poisson process if the following assumptions are true: the events are independent from one another, cannot occur at the same time, and the mean rate in a given time interval is constant [40]. The neutron beam in our interferometer experiments meets these requirements: the reactor produces a constant thermal flux of uncorrelated neutrons; when a neutron passes through the interferometer setup, the next neutron is in most cases still inside the reactor core and hence completely independent from the former. This is also emphazised by the fact that in perfect crystal interferometry, the coherence time is about 10^{-11} s [36]. One neutron constitutes a coherent state which is uncorrelated with the coherent state of the next neutron. The arrival times of these neutrons are randomly distributed. This distribution is exponential, which is shown in SEC. 2.3.1.

The situation in a neutron detector is depicted in FIG. 2.11: the total measuring time T is split into n intervals Δt, and in each of these the neutron (represented by the black dot) can be detected. With the constant probability p of detecting the neutron in a single Δt, the probability of detecting one neutron in T is $n\,(1-p)^{n-1}\,p$: in $n-1$ intervals, no neutron is detected, and the detection can happen in any of the Δt. Extended to N neutrons, the probability of detecting N neutrons in T is the binomial[2] probability with probability mass function (PMF)

$$P_{\text{bin}}(N) = \binom{n}{N} p^N\,(1-p)^{n-N}\,. \tag{2.20}$$

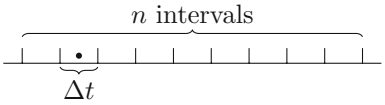

FIG. 2.11 – Detector time binning: the neutron (black dot) can be detected in any of the n intervals Δt during the measuring time $T = n\Delta t$.

[2] The binomial coefficient is $\binom{n}{k} = \frac{n!}{k!(n-k)!}$.

To simplify this expression, some approximations can be made. With low countrates and a high detector resolution, the detector binning is much finer, i.e. the number n of subintervals Δt gets large ($n \to \infty$) while the probability p of a successful detection in one of these Δt becomes small ($p \to 0$). With the additional condition that $np = \text{const} = \lambda$ (a constant number of detections), the binomial PMF can be rewritten to the Poissonian PMF as follows:

$$\begin{aligned}
\lim_{n\to\infty} P_{\text{bin}}(N) &= \lim_{n\to\infty} \frac{n!}{N!(n-N)!} \left(\frac{np}{n}\right)^N \left(1-\frac{np}{n}\right)^{n-N} \\
&= \lim_{n\to\infty} \frac{n(n-1)(n-2)\cdots(n-N+1)}{N!} \frac{\lambda^N}{n^N} \left(1-\frac{\lambda}{n}\right)^{n-N} \\
&= \lim_{n\to\infty} \frac{\lambda^N}{N!} \underbrace{\left(1-\frac{1}{n}\right)\left(1-\frac{2}{n}\right)\cdots\left(1-\frac{N-1}{n}\right)}_{\to 1} \underbrace{\left(1-\frac{\lambda}{n}\right)^n}_{\to \mathrm{e}^{-\lambda}} \underbrace{\left(1-\frac{\lambda}{n}\right)^{-N}}_{\to 1} \\
&= \frac{\lambda^N}{N!}\,\mathrm{e}^{-\lambda} \;=\; P_{\text{P}}(N)\,.
\end{aligned} \tag{2.21}$$

For the Poissonian distribution

$$P_{\text{P}}(N) = \frac{\lambda^N}{N!}\,\mathrm{e}^{-\lambda}\,, \tag{2.22}$$

the first and second moments (i.e., expectation value $\langle N\rangle$ and variance σ^2)[3] are both given by λ. Since the true value of λ is unknown, N is used as an estimator [41]. Thus for a counting experiment where N neutrons are observed, the 1σ confidence interval is given by

$$N \pm \sqrt{N}\,. \tag{2.23}$$

This important property means that longer measuring times (and therefore higher neutron counts N) decrease the relative error of the corresponding measurement. For a large number of detected neutrons N, the Poisson distribution can be further simplified to the normal (Gaussian) distribution with $\mu = \lambda$ and $\sigma = \sqrt{\lambda}$,

$$P_{\text{G}}(N) = \frac{1}{\sqrt{2\pi\lambda}}\,\mathrm{e}^{-\frac{(N-\lambda)^2}{2\lambda}}\,. \tag{2.24}$$

2.3.1 Distribution of arrival time intervals

For a Poissonian distribution of N events in a fixed time interval T, the waiting times between two detection events follow the exponential distribution. This can be calculated as follows: assume the first neutron arrives at t_0, and the next neutron arrives at time t. At times τ between t_0 and t, no further neutron has arrived, so the counts N_{t_0} and $N_{t_0+\tau}$ have to be the same:

$$t_0 < \tau < t \;\Rightarrow\; N_{t_0+\tau} = N_{t_0}\,. \tag{2.25}$$

Using the complement rule of probability (since the neutron can in principle arrive either at a time τ smaller or larger than t), this can be written as

$$P(\tau \geq t) = 1 - P(\tau < t) = 1 - P(0)\,, \tag{2.26}$$

[3] For n discrete events x_i with probabilities p_i, the expected value is $\langle x\rangle = \mu = \sum_{i=1}^n p_i x_i$, and the variance $\langle (x-\mu)^2\rangle = \sigma^2 = \langle x^2\rangle - \langle x\rangle^2 = (\sum_{i=1}^n p_i x_i^2) - \mu^2$.

because no neutron arrives at times $\tau < t$. $P(0)$ is the probability for 0 detection events and uses the definition of the Poissonian distribution eq. (2.22), giving

$$P_{\mathrm{P}}(0) = \frac{\lambda^0}{0!}\,\mathrm{e}^{-\lambda} = \mathrm{e}^{-\lambda}\,, \tag{2.27}$$

with $\lambda = I\tau$, a counting intensity per unit time I multiplied by the considered time τ. With eq. (2.26), it follows that

$$P(\tau \geq t) = 1 - \mathrm{e}^{-I\tau}\,, \tag{2.28}$$

which is the cumulative distribution function (CDF)[4] of the exponential distribution

$$P_{\mathrm{exp}}(\tau) = I\,\mathrm{e}^{-I\tau}\,. \tag{2.29}$$

This fact can be used in postselection of neutron arrival times, as will be discussed in SEC. 4.1. From eq. (2.27) one can see that this procedure only works for neutrons that follow the Poisson distribution; were they for example uniformly distributed, postselection of arrival time data would yield no further information.

A similar derivation of the simple decay form of the detection probability within a certain time interval, eq. (2.29), uses photon counting statistics and is given by Glauber [42]. For a pure coherent state, the generating function for the distribution of counts in time τ is written as

$$Q(\beta,\tau) = \mathrm{e}^{-\beta I\tau} = \sum_{N=0}^{\infty}(1-\beta)^N\,p(N,\tau)\,, \tag{2.30}$$

with an average rate I and an arbitrary parameter β. The probabilities $p(N,\tau)$ are the coefficients of the power series expansion of $Q(\beta,\tau)$ about $\beta = 1$, and result to

$$p(N,\tau) = \frac{(I\tau)^N}{N!}\,\mathrm{e}^{-I\tau}\,, \tag{2.31}$$

forming the Poisson distribution. If no neutrons are recorded in time τ, the probability is $p(0,\tau) = Q(1,\tau)$. For an initial count in the interval Δt_0 about t_0 and nothing detected until time τ, the probability is $\Delta t_0 \frac{\mathrm{d}}{\mathrm{d}t_0}\,p(0,\tau - t_0)$. Assuming the first subsequent count occurs in the interval $\Delta\tau$ about τ, and with the conditional probability $W(\tau|t_0)$ that after an initial count at t_0, the next count happens at τ,

$$-\,\Delta t_0 \frac{\mathrm{d}}{\mathrm{d}t_0}\frac{\mathrm{d}}{\mathrm{d}\tau}\,p(0,\tau-t_0)\,\Delta\tau = \Delta t_0 \frac{\mathrm{d}^2}{\mathrm{d}\tau^2}\,p(0,\tau-t_0)\,\Delta\tau = I\Delta t_0\,W(\tau|t_0)\,\Delta\tau\,. \tag{2.32}$$

From this, it follows that

$$W(\tau|t_0) = \frac{1}{I}\frac{\mathrm{d}^2}{\mathrm{d}\tau^2}\,Q(1,\tau-t_0)\,, \tag{2.33}$$

and since $Q(1,\tau - t_0) = \mathrm{e}^{-I\tau}$, the interval density $W(\tau|t_0)$ becomes

$$W(\tau|t_0) = I\,\mathrm{e}^{-I\tau}\,. \tag{2.34}$$

The preceding section has presented the tools necessary to analyse data of neutron arrival times. An important result is that the number of neutron counts N can be used to quantify both mean value and error of the underlying Poisson distribution. With a Poisson distribution of neutron detection events, the neutron arrival times follow the exponential distribution. This manipulation will be applied to measurement data in CHAPTER 4.

[4] The cumulative distribution function $F(x)$ for a probability mass function $P(x)$ is given as $F(x) = \sum_{x_i \leq x} P(x_i)$.

3 Experimental setup

This chapter discusses the experimental setups at two research reactors: the 250 kW TRIGA Mark II reactor of the Atominstitut in Vienna, Austria, and the 58 MW high-flux reactor at the Institut Laue–Langevin in Grenoble, France. First, the respective reactors are discussed, followed by the experimental components.

3.1 Atominstitut, Vienna

The Atominstitut of the University of Technology Vienna is the host of Austria's only operating nuclear reactor. Constructed by `General Atomics`, the Training, Research, Isotope production, General Atomics (TRIGA) Mark II reactor reached first criticality in 1962. It is a pool-type reactor with a continuous thermal power of 250 kW. The 83 fuel elements each consist of zirconium hydride with about 8% of weight fissile uranium and reach a core temperature of about 300 °C at maximum power. Due to the low reactor power compared to other research reactors, the burnup of these elements is small. Neutrons are moderated both by the water surrounding the fuel elements and mainly by the ZrH, which has a negative void coefficient, that is, its neutron moderation ability decreases with increasing temperature, leading to a break in the chain reaction when the reactor becomes over-critical. Therefore it also constitutes an important safety feature, effectively stabilising the reactor. The TRIGA reactor can be operated in pulsed mode, allowing for a 250 MW pulse of about 40 ms. Three boron carbide absorber rods control the chain reaction in the reactor core [43].

In FIG. 3.1 a schematic overview of the beamlines of the TRIGA reactor of the Atominstitut is given. Three radial beamlines, one tangential beam port, a thermal column and an irradiation facility with a neutron flux of $10^{-13}\,\mathrm{cm}^{-1}\,\mathrm{s}^{-2}$ allow for a variety of experiments. The neutron interferometry station is located at beamline 'C'. Measurements at this station for this thesis were conducted from December 2018 to June 2019.

In May 2019, the Atominstitut was distinguished as a 'historic site' by the European Physical Society (EPS), due to the work of Helmut Rauch, who observed interference of a neutron beam at the neutron interferometer station for the first time in 1974 [2].

3.1.1 The neutron interferometry station

At radial beamline 'C' of the reactor of the Atominstitut, the Austrian Neutron Beam Interferometer Station (ANuBIS) instrument is located at only a few metres' distance to the reactor core. The thermal neutron beam is monochromatised to $\lambda = 1.9\,\text{Å}$ with a vertically focussing pyrolytic graphite mosaic crystal. This consists of a number of perfect crystals which are not

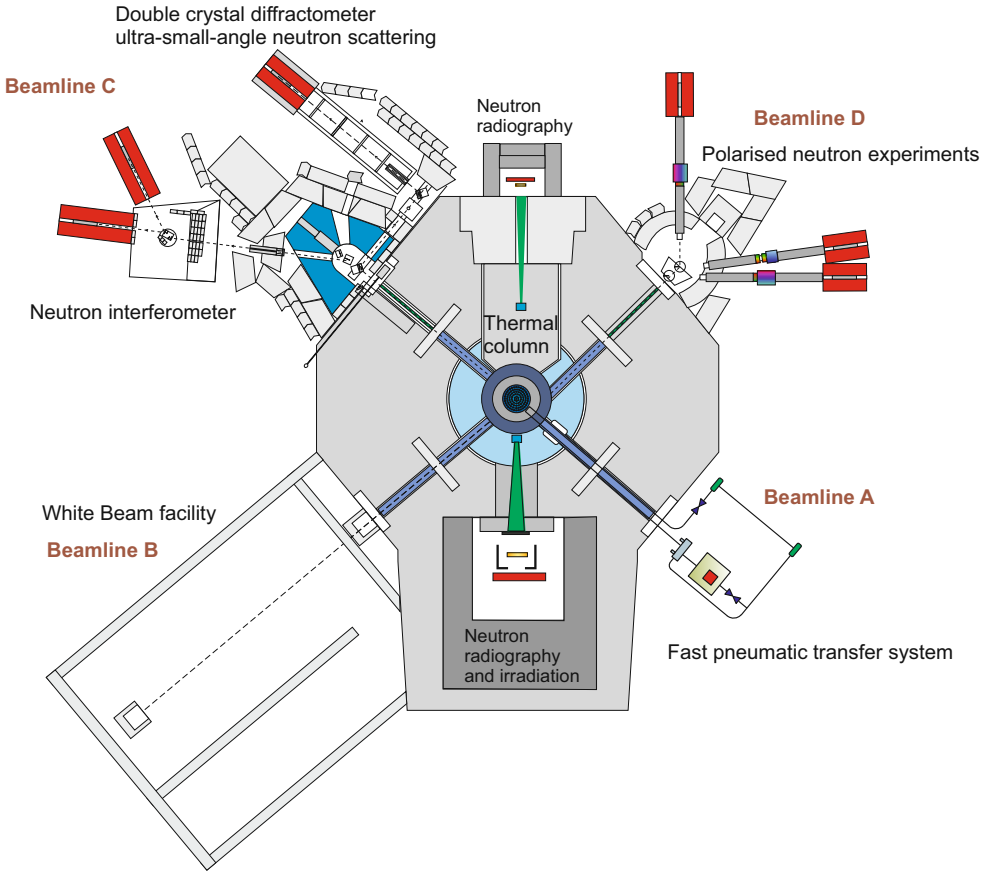

FIG. 3.1 – Schematic of the various beamlines of the TRIGA reactor at the Atominstitut Wien. The neutron interferometry station is located at beamline 'C'. Graphic by M. Villa and E. Jericha.

oriented around the same axis. Since the monochromator uses the Bragg condition (2.10), this arrangement results in a wider wavelength spread when compared to a single crystal monochromator. However, this leads to a higher integrated intensity, which is an important advantage due to the low count rates of this instrument. See [44] for more details on the monochromator.

3.1.1.1 Housing and aperture

A protective housing surrounds the sensitive instrument, shielding it from both fluctuations in the surrounding temperature (due to the exposure of the reactor hall to sunlight as well as reactor hall heating) and convection currents (due to reactor hall ventilation). Shielding from outside and scattered neutrons is achieved by an inner layer of the wall, consisting of white paraffin blocks. The inside view of this protective chamber is shown in FIG. 3.2. Through a hole in the wall on the right hand side, the monochromatised neutron beam enters the chamber between two borated polyethylene blocks that can be moved in front of the opening to shield the neutron beam during adjustments to the setup. Then, the beam passes an aperture of variable size, which is connected to two motors that allow for adjustment in z (height) and y (horizontal, perpendicular to the neutron beam) directions. For the measurements in this thesis, an aperture cross section of $10 \times 10\,\mathrm{mm}^2$ was used.

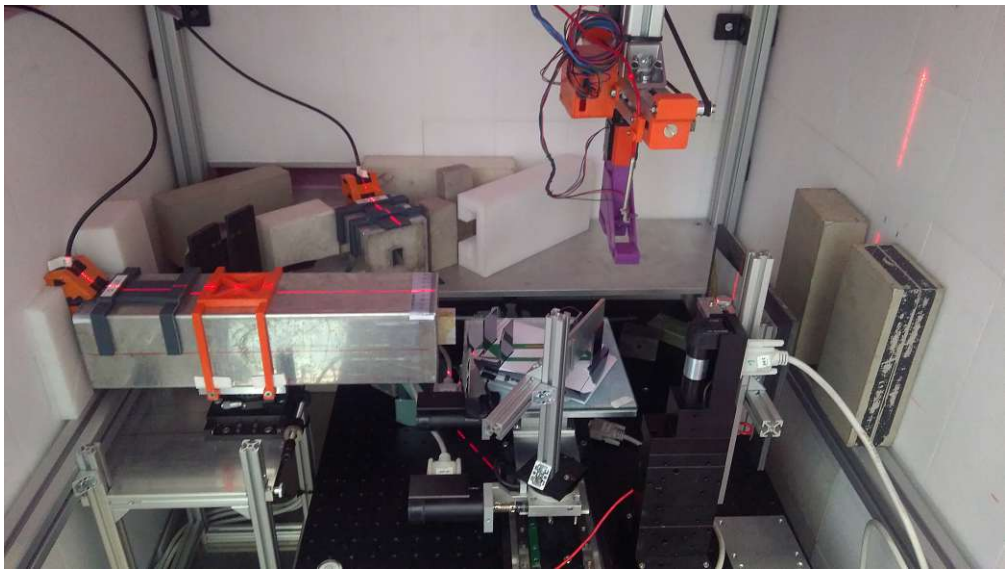

FIG. 3.2 – Setup of the ANuBIS instrument at the Atominstitut with aperture, interferometer, phase shifter, collimators and ^{3}He pencil detectors in 3D-printed mounts. Neutrons move from right to left.

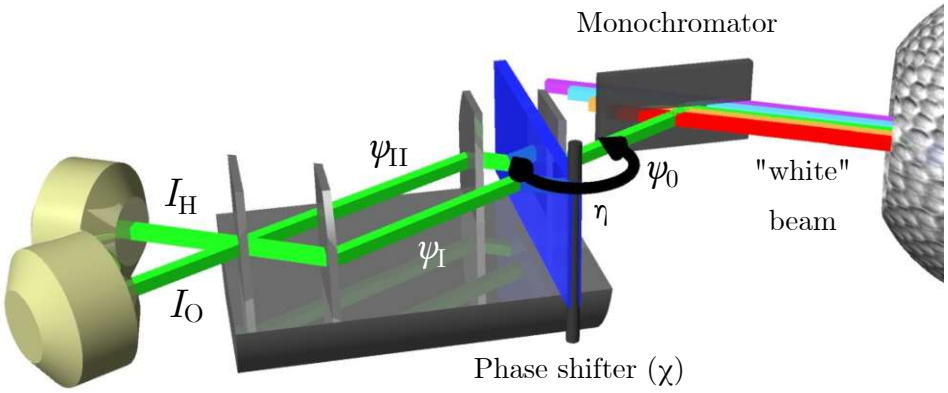

FIG. 3.3 – Schematic of the ANuBIS setup. The monochromatised incoming wave ψ_0 (right) is split into a transmitted wave ψ_I and a reflected wave ψ_{II}. After the interferometer, intensities I_O and I_H are measured by the detectors (left). The phase shifter (blue) is moved by angle η to introduce a phase difference χ between the two beam paths.

3.1.1.2 Interferometer and phase shifter

After the aperture, the neutron beam reaches the interferometer itself. ANuBIS uses a skew-symmetric silicon perfect crystal interferometer, where the 'mirror' plate described in SEC. 2.2.1 is split into two parts, with each half plate moved outwards, thus providing more space in the centre of the interferometer, allowing the investigation of larger samples. A schematic of this setup is presented in FIG. 3.3. The interferometer measures 140 mm in length and has a plate thickness of 3 mm. It sits on a glass plate on a smaller table which can be moved horizontally perpendicular to the beam direction, rotated about the vertical axis, as well as tilted.

A maximum contrast of about 50% has been observed with this setup. This is due to the intense direct beam from the mosaic crystal monochromator, which is difficult to separate from the O-beam in the interferometer, resulting in a high background. The close proximity to the reactor contributes to this background as well. In FIG. 3.4 a close-up of the interferometer is shown. The green lines on the sheet of paper in the interferometer serve as guides to the eye for a coarse adujstment. Also visible is the phase flag, a 5 mm thick aluminium slab.

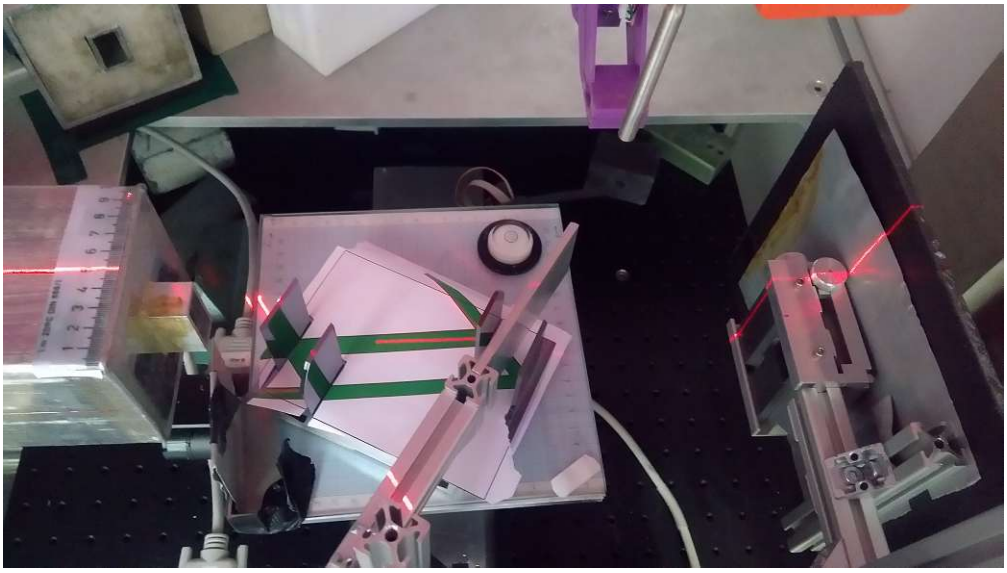

FIG. 3.4 – Close-up of the skew-symmetric interferometer with phase shifter, aperture (right) and collimators (left). Neutrons move from right to left.

Aperture, interferometer table and phase shifter are all mounted on an optical bench. This in turn is situated on a 10 mm thick aluminium plate on top of a granite block (not visible in FIG. 3.2), in order to reduce vibrations of mainly acoustic frequencies (due to people moving within the reactor hall, conversations, and nearby traffic), which have a negative impact on the interferometric contrast. This constitutes a simple passive anti-vibration system typical for optical setups. Four Pt100 sensors monitor the temperature at various places within the chamber, along with a fifth sensor in the reactor hall. For details of the housing and optical bench setup, please refer to [33].

Over the course of the measurements for this thesis, an alteration to this setup was made necessary. Since mechanical vibrations (like from a stepper motor) reduce the contrast, the phase shifter, together with its rotation stage and motor, was uncoupled from the optical bench and instead affixed to the frame of the protective housing with an aluminium plate. A close-up of the phase shifter after rebuilding is shown in FIG. 3.5. The interferometer in this picture is a

3D-printed dummy, used in order to avoid damages to the 'real' silicon interferometer during the assembly process. A robot arm with 3D-printed sample holder is also visible (top), but was not used for measurements in this thesis.

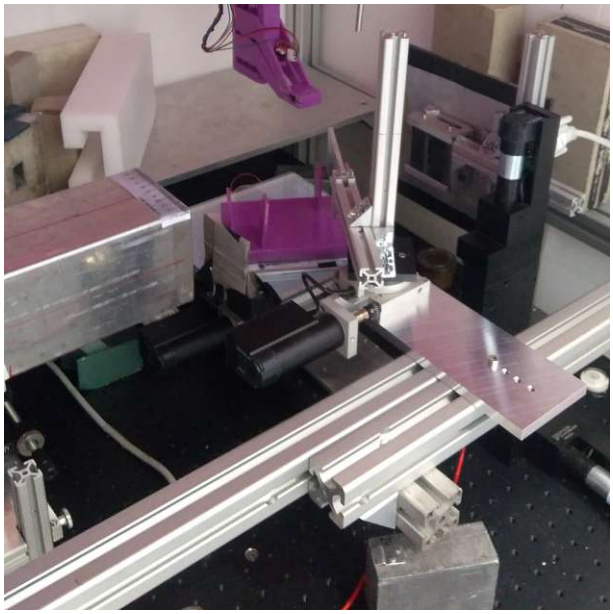

FIG. 3.5 – Close-up of the phase shifter mount after rebuilding. Note that this picture shows a 3D-printed dummy interferometer (violet).

3.1.1.3 Collimators and detectors

At the back of the interferometer, the resulting direct and diffracted beams are collimated. In direct (O) direction, a long collimator is mounted on a linear translation stage, allowing for a manual adjustment perpendicular to the neutron beam. It can also be turned about the vertical axis, likewise manually via a precision screw. In diffracted (H) direction, a smaller collimator was introduced in the course of the measurement progress. It stands on a boron carbide mat on top of an aluminium sheet affixed to the housing structure and is, as of yet, not mounted to a translation or rotation stage, thus making for a tedious alignment process. Alignment is further made complicated by the low count rates in the setup; the intensity in the O-beam for optimal adjustment of aperture, interferometer and collimators is about one count per second. A useful tool in the alignment process is the `ND&M` handmonitor, a ZnS(Ag)+LiF scintillator as described in SEC. 2.1.3.2. It is a position sensitive detector with a pixel size of $40\,\mu$ and a diameter of $\sim 4\,\text{cm}$. This allows for a direct observation of the neutron beam, and although the detection efficiency for thermal neutrons lies around 12 %, this is sufficient for a coarse first arrangement of the experimental components.

Having passed the collimators, the neutrons then leave the protective housing of the ANUBIS setup and are detected in large BF_3 barrel counter tubes (not shown in FIG. 3.2), designated 'O' and 'H' detectors in the following, operating at 1400 V. For a description of the operating principle, see SEC. 2.1.3.1. 3D-printed mounts for smaller, 'pencil' detectors, are affixed onto the collimators. These pencil detectors, ^{3}He proportional counters with a diameter of 0.25 inch or 6.35 mm (see SEC. 2.1.3.3), manufactured by `Toshiba`, have a much smaller volume than the BF_3 barrels, which is crucial for the precision of the time-resolved measurements performed over the course of this thesis. They also present an important extension to the existing ANUBIS setup. One of these detectors, together with its preamplifier module, is shown in FIG. 3.6.

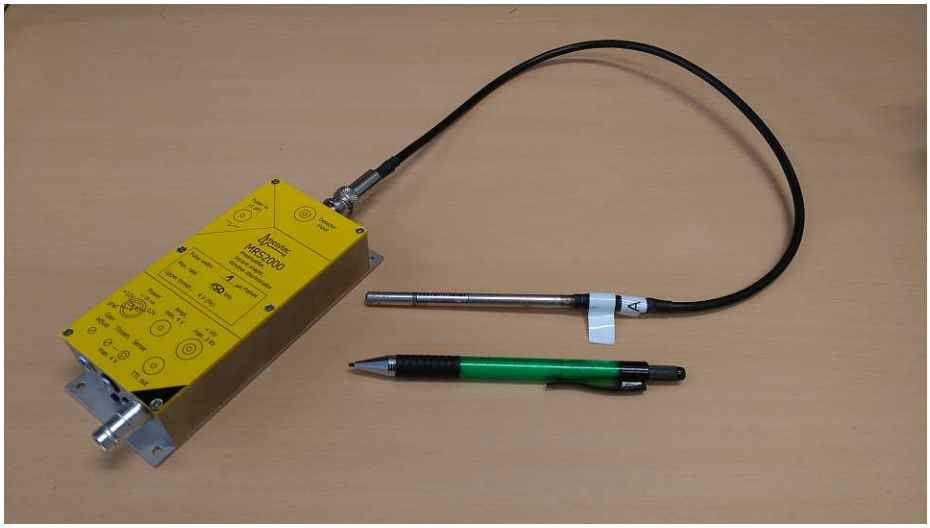

FIG. 3.6 – `Toshiba` pencil detector with preamplifier module (yellow box) and pen for comparison.

To eliminate background, the 3D-printed mounts are clad in cadmium and boron carbide mats, leaving only a small window through which the neutrons can pass. In FIG. 3.7 a closer look at the shielding of such a mount is given: clearly visible is the window, smaller in the Cd foil (silver) than in the BC_4 mat (black). The pencil detectors are called 'O aux' and 'H aux' and operate at 15 bar and a high voltage of 1320 V and 1500 V, respectively.

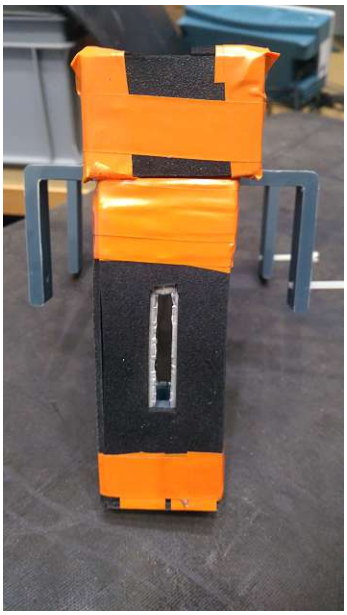

FIG. 3.7 – Front view of the shielding of a pencil detector mount (empty).

The control of the motors as well as the execution of measurement scripts are made with an extensive `LabVIEW` program. The time-resolved measurements discussed in CHAPTER 4 were realised using a 40 MHz FPGA card from `National Instruments`, type `PXI-7842R`. See SEC. 4.2 for a more detailed description of these measurements.

3.2 Institut Laue–Langevin, Grenoble

Founded in 1967, the Institut Laue–Langevin (ILL) in Grenoble, France, is home to one of the world's brightest neutron sources, the High-Flux reactor (HFR) with a neutron flux of $1.5 \times 10^{15}\,\mathrm{s^{-1}\,cm^{-2}}$ and a thermal power of 58.3 MW. In `cycle 185`, during which the measurements for this thesis were performed in July and August 2019, the reactor was operating at 52 MW.

A single highly-enriched 10 kg uranium fuel element constitutes the reactor core, which is contained within a heavy-water pressure vessel. The chain reaction is controlled by an absorber rod, and the reactor has five additional safety rods. Collisions with the deuterium in the heavy-water tank moderate the neutrons to speeds of around $2.2\,\mathrm{km\,s^{-1}}$, thus both sustaining the chain reaction and providing neutrons to the instruments working with thermal neutrons. Two cold sources and a hot source present the possibility to experiment with neutrons over a wide range of energies on top of the thermal regime. On one of the around twenty user instruments, the S18 CRG instrument is located in guide hall 1 at the thermal beam line H25 [45].

3.2.1 The S18 instrument

The S18 setup is essentially the same as the ANuBIS setup. Since the ILL reactor has a much higher flux, for a decent alignment of the components, about 100 counts per second can be reached in the O detector for an aperture of $3 \times 3\,\mathrm{mm^2}$, two orders of magnitude more than at the Austrian TRIGA reactor setup (even with the larger aperture of $1\,\mathrm{cm^2}$). Like ANuBIS, the S18 setup uses a three-plate interferometer. Two housings surround the instrument both to ensure temperature stability with an additional air conditioning unit, and to shield the outside area from neutrons and γ rays.

Inside the chamber, the interferometer is set up on a glass block on top of a table that can be rotated about the vertical axis on a vibration-isolated optical bench. Bragg angle orientations between 45° and 30° are possible for the setup. Measurements for this thesis used the 30° configuration for the (2,2,0) reflection of the silicon crystal (as schematically illustrated in FIG. 2.7), corresponding to a wavelength of 1.9 Å [46]. Besides the obvious difference in reactor power, there are three further main variations in comparison to the Vienna setup: the monochromator, the interferometer and the detectors, which will be discussed in the following sections. An overview of the setup is given in FIG. 3.8.

3.2.1.1 Monochromator and aperture

The monochromator at the S18 instrument is a silicon perfect crystal (as opposed to the pyrolytic graphite mosaic crystal in Vienna). The monochromator and the interferometer platform are rigidly connected, which is required when using single crystal monochromators. Due to the higher flux of the ILL reactor, the loss of intensity at the gain of a much narrower Bragg peak (smaller FWHM) is acceptable. To further enhance the precision of the interferometric measurements, two silicon prisms are inserted into the neutron beam between monochromator and aperture. These scatter out the higher orders in the Bragg peak, i.e. neutrons with $\lambda/2$. After the prisms, the neutrons pass through an aperture of variable size, which was set to $3 \times 3\,\mathrm{mm^2}$ for the experiments at the S18.

3.2.1.2 Interferometer and phase shifters

For measurements in Grenoble, the symmetric 'Kaiser' three-plate interferometer was used. It is 140 mm long and has a plate thickness of 3 mm. A fringe visibility of more than 80% was recorded when precisely aligned. After damages to the interferometer during measurements in

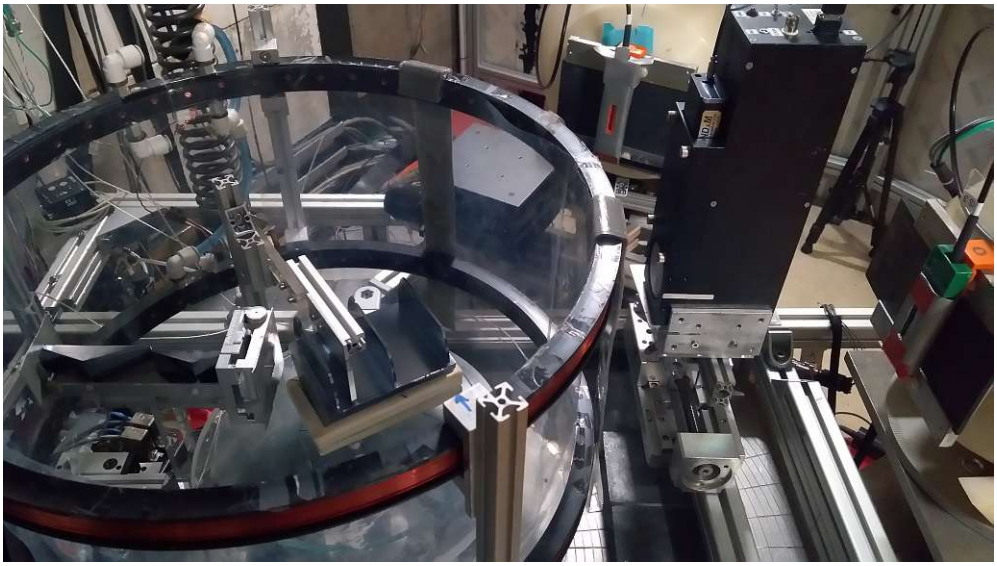

FIG. 3.8 – Setup at the S18 instrument at the ILL in Grenoble. Visible are the silicon prisms in front of the aperture, the interferometer with phase shifter, detectors O (right) and H (back) with Cd-clad pencil detector mounts as well as the neutron camera with handmonitor (black). Neutrons move from left to right.

Grenoble, which significantly lowered the contrast due to internal stress in the crystal lattice, it had to be re-etched in a process described in [33]. It is likely that the ideal condition was not completely restored, a fact also made evident by large variations of the contrast when varying the position of the entrance point of the neutron beam on the interferometer plate.

Three different phase shifters were used for the measurements described in this thesis: a large 5 mm thick aluminium slab visible in FIG. 3.8 and FIG. 3.10B, a 3 mm sapphire slab, and a small 5 mm Al slab. The latter was used for most of the measurements discussed in CHAPTER 5, since its small physical dimensions allow for a placement of both the phase shifter and the path blocker box (described in SEC. 3.2.1.4) between the 'splitter' and 'mirror' (i.e. the first two) plates of the interferometer.

Interferometer, phase shifter, and aperture with silicon prisms are additionally surrounded by two circular guide field coils with hydrogen-free plastic foil in between them, with acrylic glass sheets on top (the latter is not depicted in FIG. 3.8), to further inhibit convection currents around the interferometer and ensuring an even more stable environment. The guide field itself was not applied, as measurements were performed with unpolarised neutrons.

3.2.1.3 Detectors

Like the ANUBIS setup, the S18 setup has two large barrel detectors for the O and H beams. At the S18, these are ^{3}He proportional counters (operational principle discussed in SEC. 2.1.3.3), encased in paraffin to ensure a low background. In addition, pencil detectors for time-resolved measurements were introduced to the setup and mounted in 3D-printed holders hung in front of the large detectors. No collimators were used for the measurements, since the beams at S18 are sufficiently collimated. The pencil detectors used in Grenoble are also ^{3}He counter tubes of diameter 0.25 ± 0.01 mm, manufactured by `Baker Hughes`. They are designated 'RS 1' to 'RS 4' and operate at a pressure of 40 atm at 2100 V. An aluminium foil cap is affixed to the front of the pencil detectors to decrease noise.

For both detector types, `mesytec MRS2000` preamplifier systems are used. These are all-in-one devices that comprise a preamplifier, a square pulse shaper and a window discriminator with an upper threshold of 4 V. Furthermore, it is important to note that compared to the setup in Vienna, the O and H beams are in mirror-inverted positions. This is due to the interferometer in use, as well as geometric limitations to the setup.

The handmonitor, already mentioned in the ANuBIS setup (see SEC. 3.1.1.3), was also used at the S18. Combined with a CCD camera for automatised readout of detected neutrons, this proved a useful tool in the aperture position optimisation process. This system is visible as the black box in FIG. 3.8. A close-up of the O detector with the (not yet cadmium-clad) 3D-printed mount containing the 'RS 3' pencil detector is shown in FIG. 3.9A.

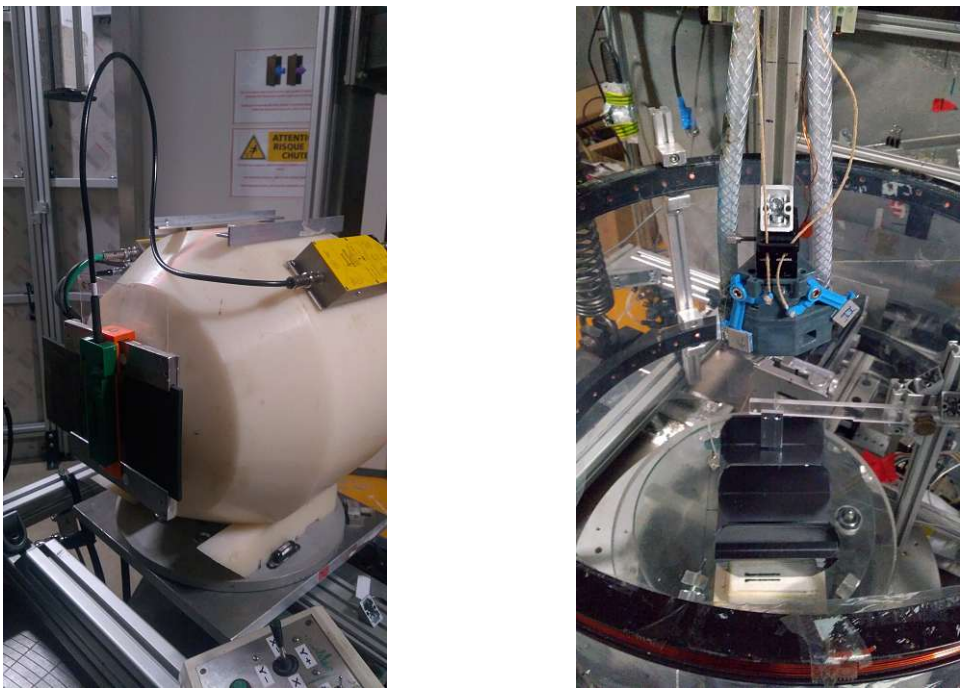

(A) (B)

FIG. 3.9 – Details of instrument components of the S18 setup. (A) – Close-up of the O detector with 'RS 3' pencil detector mounted in the 3D-printed holder (green) in front. Also visible is the preamplifier box for the pencil detector (yellow box). (B) – Front view of the path blocker box with beam blocker for path I in place above the interferometer. The 3 mm Al phase shifter is depicted as well.

3.2.1.4 Path blocker box

For the measurements regarding the Leggett–Garg inequality (LGI) [16] (see CHAPTER 5), a method to automatically block one or the other neutron path in the interferometer was needed. A 3D printed box with pathwise beam blockers driven by an `Arduino` controlled stepper motor was used to achieve this functionality. It is mounted to a robot arm that can be inserted into the interferometer, and has two wings onto which cadmium foil is attached. Designations 'I' and 'II' mark the path that is blocked when the respective arm of the beam blocker is in place. The stepper motor moves the blocker in positions '1', '2' (for blocked paths I and II) and '0' (for both paths unblocked).

On the back side of the windows through which the neutron beam passes, absorbers of variable thickness can be inserted. For measurements in this thesis, an indium foil absorber with thicknesses of 1, 2 and 3 mm was used and inserted in beam path I, leaving beam path II unblocked. In FIG. 3.9B, the path blocker box is shown above the interferometer with shield I closed and shield II open; and FIG. 3.10A shows the path blocker box in its position inside the first half of the interferometer during measurements.

3.2.1.5 Raster setup

For the Leggett–Garg inequality (LGI) measurements, a method to transversally scan the beam profile in both paths was needed, to be able to compare count rates in the partial beams I and II. This was done with pencil detectors affixed to a linear translation stage. When the stage moves, the pencil detectors are guided in the second half of the interferometer, between the 'mirror' and 'analyser' plates, crossing first the direct beam, followed by beams I and II. The adjustment of the detectors for this setup was rather difficult, since the translation stage has a limited range, and neither pencil detectors nor their mounting must touch the interferometer. A further problem was the choice of height and angle, at which the detectors should be mounted, to be both low enough for the active volume of the detector to enter the beam, and high enough so as to still have satisfactory beam separation.

In FIG. 3.10, two configurations for the rastering setup are presented: the top figure shows two parallel pencil detectors, seen from above, and the bottom figure shows a side view of a single rastering detector. Additional shieldings (not shown) made from cadmium foil with a pinhole aperture were later added for a more precise beam profile measurement.

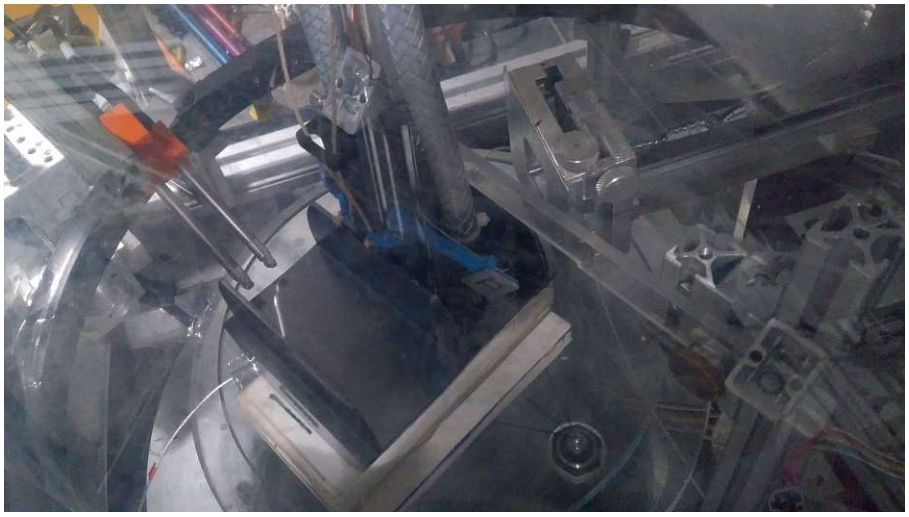

(A)

(B)

FIG. 3.10 – Details of the raster setups with one and two pencil detectors and path blocker box. (A) – Top view of the raster setup with two pencil detectors. The path blocker box is inserted into the first half of the interferometer, blocking the view of the phase shifter. (B) – Side view of the raster setup with a single detector. Visible are the silicon prisms next to the aperture, the 'Kaiser' interferometer with the inserted 5 mm aluminium phase shifter, the rastering pencil, and the large H detector in the background.

4 Time-resolved measurements

This chapter discusses time-resolved neutron interference measurements that were performed both at the Atominstitut Wien from December 2018 to June 2019, and at the Institut Laue–Langevin (ILL), Grenoble, in July 2019. After the general concept of these measurements, the differences and similarities of the results obtained at the two reactors are described.

4.1 Theoretical background

On top of the total neutron counts in a given time interval, their absolute arrival times in the detector can also be recorded. They represent additional information which can be used for time-selective postselection in data analysis. Two applications of this procedure are the enhancement of interferometric contrast and reduction of phase uncertainty. Zawisky et al. investigated this effect for the first time in 1994 [36]. This theoretical background follows in large parts the derivations and discussions in their paper.

4.1.1 Contrast enhancement

Starting from the initial intensity $I(\chi)$ dependent on the phase χ, and introducing C_{in} which denotes the initial contrast of the recorded interferogram before postselection, eq. (2.18) becomes

$$I(\chi) = \bar{I}(1 + C_{\text{in}} \cos \chi)\,. \tag{4.1}$$

The initial contrast is defined according to eq. (2.19), but with the additional condition of a fixed phase for the O beam, $I_{\max} = I(\chi = 0)$ and $I_{\min} = I(\chi = \pi)$. Conversely, the H beam intensity is at its minimum for $\chi = 0$, and at its maximum for $\chi = \pi$, equivalent to a π-shift in χ between the two detectors. This results in

$$\begin{aligned} C_{\text{in,O}} &= \frac{I_{\text{O}}(0) - I_{\text{O}}(\pi)}{I_{\text{O}}(0) + I_{\text{O}}(\pi)} \\ C_{\text{in,H}} &= \frac{I_{\text{H}}(\pi) - I_{\text{H}}(0)}{I_{\text{H}}(\pi) + I_{\text{H}}(0)}\,, \end{aligned} \tag{4.2}$$

and is an important quantity in the comparison of achieved contrast values, which will be made clear later (see FIG. 4.23 and discussion).

To put selected times in relation, mean arrival times for given phase positions χ are defined

by

$$\bar{\tau}(\chi) = \frac{1}{I(\chi)} \tag{4.3}$$

and a phase-independent mean arrival time of the whole interference pattern by $\bar{\tau}_D = \bar{I}_D^{-1}$. The total number of counts for a given phase shifter position χ results in $N_D(\chi) = I_D(\chi)\,T$, with the measuring time T per point and the index D denoting the O or H detector.

Time interval densities $W(\tau)$ describe the probability for a neutron pair event within a time interval τ, and can be calculated using the identity from [42],

$$W(\tau) = \frac{1}{\bar{\tau}(\chi)}\, \mathrm{e}^{-\frac{\tau}{\bar{\tau}(\chi)}} = I(\chi)\, \mathrm{e}^{-\tau I(\chi)}\,. \tag{4.4}$$

The expectation value for the number of pair events in such a time interval τ then becomes $NW(\tau)$, and of course, since it is a probability function, $\int_0^\infty W(\tau)\,\mathrm{d}\tau = 1$.

In FIG. 4.1, the time interval densities for the maximum (blue curve) and minimum (orange curve) intensity in the respective detector, with typical contrast and intensity values for the setup at the Atominstitut, are shown. The point of intersection of the two curves is at

$$\tau_{\mathrm{int}} = \frac{1}{I_{\max} - I_{\min}} \ln\left(\frac{I_{\max}}{I_{\min}}\right)\,, \tag{4.5}$$

which is slightly larger than the respective $\bar{\tau}_D$. The area between the curves corresponds to the observed neutron pairs. At smaller times, the contribution from the maximum dominates, while at larger times $\tau > \bar{\tau}_D$ the contribution from the minimum is higher. $\bar{\tau}_D$ presents a useful parameter to separate these two contributions.

With eq. (4.4), the number of detected neutrons with arrival times in the interval $[\tau_1, \tau_2]$ can be calculated as

$$N(\chi, \tau_1, \tau_2) = N(\chi) \int_{\tau_1}^{\tau_2} W(\tau)\,\mathrm{d}\tau = N(\chi)\left[\mathrm{e}^{-\frac{\tau_1}{\bar{\tau}(\chi)}} - \mathrm{e}^{-\frac{\tau_2}{\bar{\tau}(\chi)}}\right]\,. \tag{4.6}$$

To determine the analytical form of the contrast curves for selected time intervals one starts with eq. (4.2) and eq. (4.6). For easier calculation, the initial (pre-postselected) fit curve of the interferogram is denoted $g(\chi) = y_0 + a\ \cos\chi$ ($y_0, a > 0$), with $g(0) \to \max$ and $g(\pi) \to \min$, as well as $T_i = \tau_i/T$. In the following sections, the resulting contrast enhancement is calculated explicitly for the O detector.

4.1.1.1 Selection of short arrival times

For short time intervals $[0, \tau_2]$, eq. (4.6) becomes

$$N(\chi, \tau_2, T) = g(\chi)\left(1 - \mathrm{e}^{-T_2 g(\chi)}\right)\,. \tag{4.7}$$

At $\chi = 0$ and $\chi = \pi$, this becomes

$$\begin{aligned} N(0, \tau_2, T) &= (y_0 + a)\left(1 - \mathrm{e}^{-T_2(y_0+a)}\right) \\ N(\pi, \tau_2, T) &= (y_0 - a)\left(1 - \mathrm{e}^{-T_2(y_0-a)}\right)\,. \end{aligned} \tag{4.8}$$

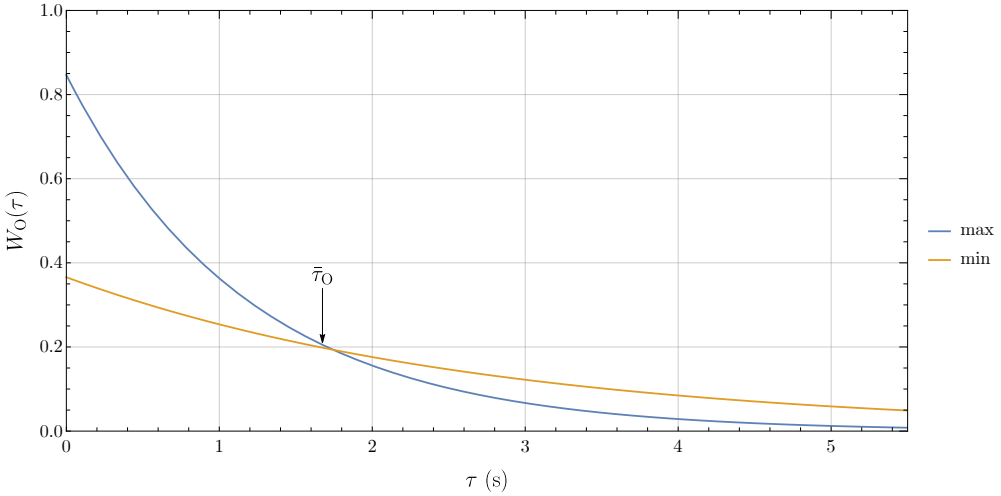

(A) O detector

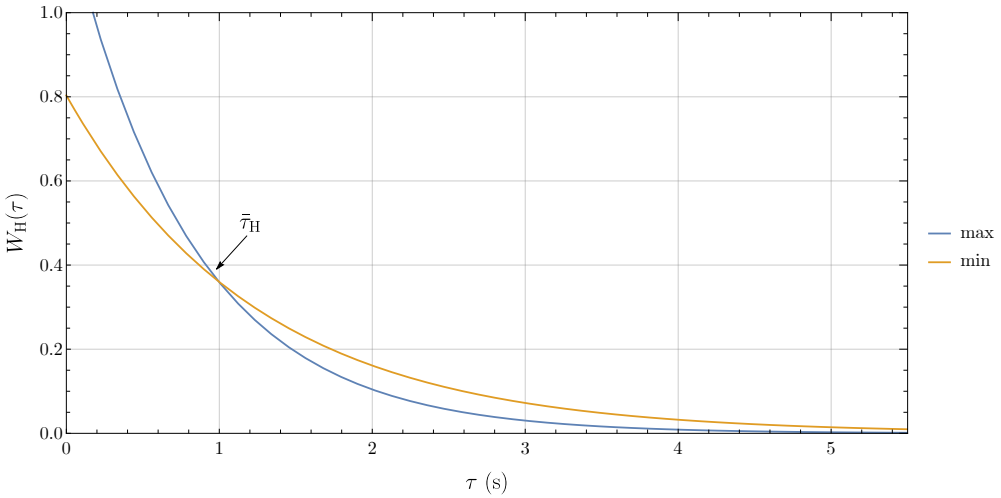

(B) H detector

FIG. 4.1 – Time interval densities for maximum (blue) and minimum (orange) intensity in a typical interferogram at the ANuBIS setup. Minimum and maximum curves intersect near the respective mean arrival time for the given detector $\bar{\tau}_D$. (A) O detector, with $C_{\mathrm{in,O}} = 0.4$ and $\bar{\tau}_O = 1.67\,\mathrm{s}$. (B) H detector, with $C_{\mathrm{in,H}} = 0.22$ and $\bar{\tau}_H = 0.98\,\mathrm{s}$.

Putting this into the definition eq. (4.2) gives

$$C_O(\tau_2) = \frac{(y_0+a)\left(1-\mathrm{e}^{-T_2(y_0+a)}\right)-(y_0-a)\left(1-\mathrm{e}^{-T_2(y_0-a)}\right)}{(y_0+a)\left(1-\mathrm{e}^{-T_2(y_0+a)}\right)+(y_0-a)\left(1-\mathrm{e}^{-T_2(y_0-a)}\right)} := \frac{A}{B}\,, \tag{4.9}$$

with the numerator

$$\begin{aligned} A &= (y_0+a)(1-\mathrm{e}^{-T_2(y_0+a)})-(y_0-a)(1-\mathrm{e}^{-T_2(y_0-a)}) \\ &= 2a+\mathrm{e}^{-T_2y_0}\left(\mathrm{e}^{T_2a}(y_0-a)-\mathrm{e}^{-T_2a}(y_0+a)\right) \\ &= 2a+2\,\mathrm{e}^{-T_2y_0}\left(y_0\sinh(T_2a)-a\cosh(T_2a)\right) \end{aligned} \tag{4.10}$$

and denominator

$$\begin{aligned} B &= (y_0 + a)\left(1 - \mathrm{e}^{-T_2(y_0+a)}\right) + (y_0 - a)\left(1 - \mathrm{e}^{-T_2(y_0-a)}\right) \\ &= 2y_0 - \mathrm{e}^{-T_2 y_0}\left(\mathrm{e}^{T_2 a}(y_0 - a) + \mathrm{e}^{-T_2 a}(y_0 + a)\right) \\ &= 2y_0 + 2\,\mathrm{e}^{-T_2 y_0}\left(a\,\sinh(T_2 a) - y_0\,\cosh(T_2 a)\right)\,, \end{aligned} \tag{4.11}$$

giving the end result of

$$C_{\mathrm{O}}(\tau_2) = \frac{a\,\mathrm{e}^{T_2 y_0} + y_0\,\sinh(T_2 a) - a\,\cosh(T_2 a)}{y_0\,\mathrm{e}^{T_2 y_0} + a\,\sinh(T_2 a) - y_0\,\cosh(T_2 a)},\quad T_2 = \frac{\tau_2}{T}\,. \tag{4.12}$$

The derivative with respect to χ, indicated by $N'(\chi, \tau_2, T)$,

$$\begin{aligned} \frac{\mathrm{d}}{\mathrm{d}\chi}N(\chi,\tau_2,T) &= g'(\chi)\left(1 - \mathrm{e}^{-T_2 g(\chi)}\right) + g(\chi)\,T_2\,g'(\chi)\,\mathrm{e}^{-T_2 g(\chi)} \\ &= g'(\chi)\left(1 - \mathrm{e}^{-T_2 g(\chi)}\left(1 - T_2\,g(\chi)\right)\right)\,, \end{aligned} \tag{4.13}$$

results in the familiar zeroes $\chi = n\pi$, i.e. for selected short times, the definition of the contrast via fixed phase angles eq. (4.2) would not have been necessary. This changes for selected long arrival times.

4.1.1.2 Selection of long arrival times

Analogously to the previous section, for arrival times in the interval $[\tau_1, T]$, eq. (4.6) becomes

$$N(\chi,\tau_1,T) = g(\chi)\left(\mathrm{e}^{-T_1 g(\chi)} - \underbrace{\mathrm{e}^{-g(\chi)}}_{\to 0}\right) = g(\chi)\,\mathrm{e}^{-T_1 g(\chi)} \tag{4.14}$$

since $\tau_1 \ll T$, and the second term vanishes, which means we basically treat arrival times in the interval $[\tau_1, \infty)$. At $\chi = 0$ and $\chi = \pi$, this is

$$\begin{aligned} N(0,\tau_1,T) &= (y_0 + a)\,\mathrm{e}^{-T_1(y_0+a)} \\ N(\pi,\tau_1,T) &= (y_0 - a)\,\mathrm{e}^{-T_1(y_0-a)}\,, \end{aligned} \tag{4.15}$$

and eq. (4.2) gives

$$C_{\mathrm{O}}(\tau_1) = \frac{(y_0 + a)\,\mathrm{e}^{-T_1(y_0+a)} - (y_0 - a)\,\mathrm{e}^{-T_1(y_0-a)}}{(y_0 + a)\,\mathrm{e}^{-T_1(y_0+a)} + (y_0 - a)\,\mathrm{e}^{-T_1(y_0-a)}}\,, \tag{4.16}$$

which can also be expressed as

$$C_{\mathrm{O}}(\tau_1) = \frac{-y_0\,\sinh(T_1 a) + a\,\cosh(T_1 a)}{y_0\,\cosh(T_1 a) - a\,\sinh(T_1 a)}\,. \tag{4.17}$$

Beside the familiar zeroes at $\chi = n\pi$, the derivation $N'(\chi, \tau_1, T)$,

$$\frac{\mathrm{d}}{\mathrm{d}\chi}N(\chi,\tau_1,T) = \mathrm{e}^{-T_1 g(\chi)} g'(\chi)\left(1 - T_1 g(\chi)\right)\,, \tag{4.18}$$

has additional zeroes for $T_1 g(\chi) = 1$, corresponding to a shift in the positions of minima and maxima, which legitimises the definition of the contrast with fixed phases, eq. (4.2).

4.1.1.3 Limits of contrast enhancement

For time intervals $\tau \in [0, \tau_2]$, the intensity is

$$I(\chi, 0, \tau_2) = I(\chi) \left(1 - \mathrm{e}^{-\tau_2 I(\chi)}\right) , \tag{4.19}$$

and with the expansion $\mathrm{e}^{-\tau_2 I(\chi)} = 1 - \tau_2 I(\chi) + \dots$ for $\tau_2 \to 0$ becomes $I(\chi) \approx \tau_2 I^2(\chi)$. With this, the maximum reachable contrast for small time intervals is

$$\lim_{\tau_2 \to 0} C(0, \tau_2) = \frac{2\, C_{\mathrm{in}}}{1 + C_{\mathrm{in}}^2} \leq 2\, C_{\mathrm{in}} . \tag{4.20}$$

This means that for small initial contrast, an increase to values twice as large as C_{in} is possible. On the other hand, for already large C_{in}, the relative gain is small. Even with postselection, the contrast can never exceed 1.

For long time intervals, $\tau \in [\tau_1, \tau_2 \to \infty)$, the intensity is

$$I(\chi, \tau_1, \infty) = I(\chi)\, \mathrm{e}^{-\tau_1 I(\chi)} . \tag{4.21}$$

The contrast undergoes a phase inversion and, according to eq. (4.2), becomes negative, with a maximum value of -1 [36]. This is also made clear in FIG. 4.1: for longer times τ, the minimum intensity curve (orange) is higher than the maximum (blue), which results in the sign change, since eq. (4.2) has defined fixed angle positions for contrast calculation. Furthermore, the maximum intensity curve approaches zero faster than the minimum. For the total time interval $[0, T \to \infty]$, $W(\tau) = 1$ and thus the intensity $I(\chi)$ takes the familiar form of eq. (2.18).

In addition to these mathematical constraints on the obtainable contrast values, the loss of intensity due to external vibrations, changes to the surrounding temperature, etc. has to be considered. For a good improvement to the contrast, τ_2 has to become small, which means that only a fraction of the detected neutrons are used for further analysis, resulting in the need for much longer measurement times. This can also be made difficult by limitations of the experimental setup.

4.1.2 Reduction of phase uncertainty

Another property to consider is the phase resolution. In Poissonian statistics, $\Delta N = \sqrt{N}$, and the phase uncertainty becomes

$$\Delta\chi\left(\chi, \tau_1, \tau_2\right)^2 = \frac{N\left(\chi, \tau_1, \tau_2\right)}{\left(\frac{\partial}{\partial\chi} N\left(\chi, \tau_1, \tau_2\right)\right)^2} . \tag{4.22}$$

Using again eq. (4.6) and the same shorthand as above $g(\chi) = N(\chi) = y_0 + a\, \cos\chi$ $(y_0, a > 0)$, with $g'(\chi)$ denoting the derivation with respect to χ, the initial phase uncertainty is

$$\Delta\chi\left(\chi\right)^2 = \frac{N\left(\chi\right)}{\left(\frac{\partial}{\partial\chi} N\left(\chi\right)\right)^2} = \frac{g'(\chi)^2}{g(\chi)^2} . \tag{4.23}$$

The interesting property is the behaviour of the phase uncertainty, and how postselection of arrival time intervals allows for a reduction in comparison to the initial $\Delta\chi(\chi)$. Introducing another shorthand, $\xi = g(\chi)\ \tau_2/T$, the phase uncertainty for short time intervals $(0, \tau_2)$ in comparison to the initial one becomes

$$\frac{\Delta\chi(\chi, 0, \tau_2)^2}{\Delta\chi(\chi)^2} = \frac{g(\chi)\left(1 - \mathrm{e}^{-\xi}\right)}{g(\chi)} \frac{g'(\chi)^2}{\left(g'(\chi)\left(1 - \mathrm{e}^{-\xi}\right) + g'(\chi)\xi\, \mathrm{e}^{-\xi}\right)^2} = \frac{1 - \mathrm{e}^{-\xi}}{\left(1 - \mathrm{e}^{-\xi} + \xi\, \mathrm{e}^{-\xi}\right)^2} , \tag{4.24}$$

which has a minimum at $\xi = 1.249$. Therefore an optimal selection interval with minimal phase uncertainty exists at $[0, \tau_2 = 1.249\ \bar{\tau}]$.

Similarly, for long time intervals $[\tau_1, T]$, with $\zeta = g(\chi)\ \tau_1/T$, the phase uncertainty relative to the initial one is

$$\frac{\Delta\chi(\chi, \tau_1, T)^2}{\Delta\chi(\chi)^2} = \frac{\mathrm{e}^{-\zeta}}{(\mathrm{e}^{-\zeta} - \zeta\,\mathrm{e}^{-\zeta})^2} = \frac{\mathrm{e}^{-\zeta}}{(1-\zeta)^2}\,. \tag{4.25}$$

Here no improvement to the phase resolution is possible, and there is a singularity at $\zeta = 1 \rightarrow \tau_1 = \bar{\tau}$, which coincides with the loss of contrast in selection intervals $[\bar{\tau}, T]$.

The behaviour of the phase uncertainty $\Delta\chi(\tau_1, \tau_2)$ in relation to the initial value $\Delta\chi_{\mathrm{in}}$ is displayed in FIG. 4.2 for the O detector of a typical interferogram recorded at the Atominstitut, where $\bar{\tau} \sim 1.67\,\mathrm{s}$ and $\bar{I} \sim 0.60\,\mathrm{s}^{-1}$. For short time intervals, an improvement to the phase resolution is possible, with the minimum value of $\tau_2 \sim 2\,\mathrm{s}$ (see FIG. 4.2A). Consequently, for selected small times, both a gain in the contrast as well as in phase resolution is possible. When longer times are selected (see FIG. 4.2B), the phase resolution cannot be enhanced.

The phase resolution can also be calculated via the uncertainty between the canonical variables phase χ and particle number N, $\Delta\chi^2\Delta N^2 = 1$ [47], and expressed in terms of the initial contrast C_{in} of the interferogram [6],

$$(\Delta\chi)^2 N = \frac{1}{1 - \sqrt{1 - C_{\mathrm{in}}^2}}\,. \tag{4.26}$$

For visibilities considerably smaller than unity, the right hand side of the above equation can be approximated using Taylor expansion to $2/C_{\mathrm{in}}^2$, resulting in

$$(\Delta\chi)^2 N = \frac{2}{C_{\mathrm{in}}^2}\,. \tag{4.27}$$

For further discussion of phase-particle number uncertainties, please see for example [48].

The reduction in phase uncertainty has useful applications when the count rates or initial contrast of the recorded interferogram are low [49, 50], for measurements of the geometric phase [51], Laue phase [52], scattering lengths [53] or thin film density [54].

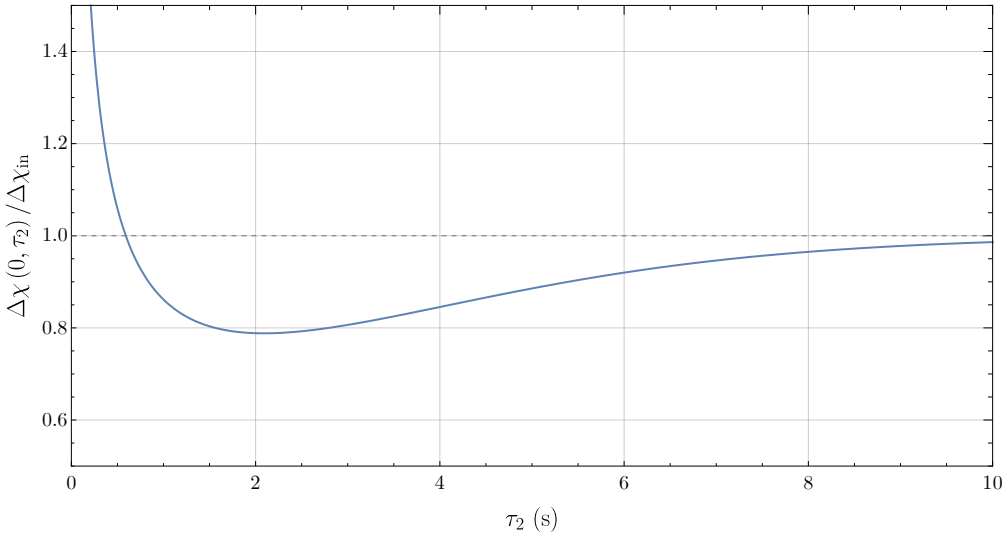

(A) Selection of short times.

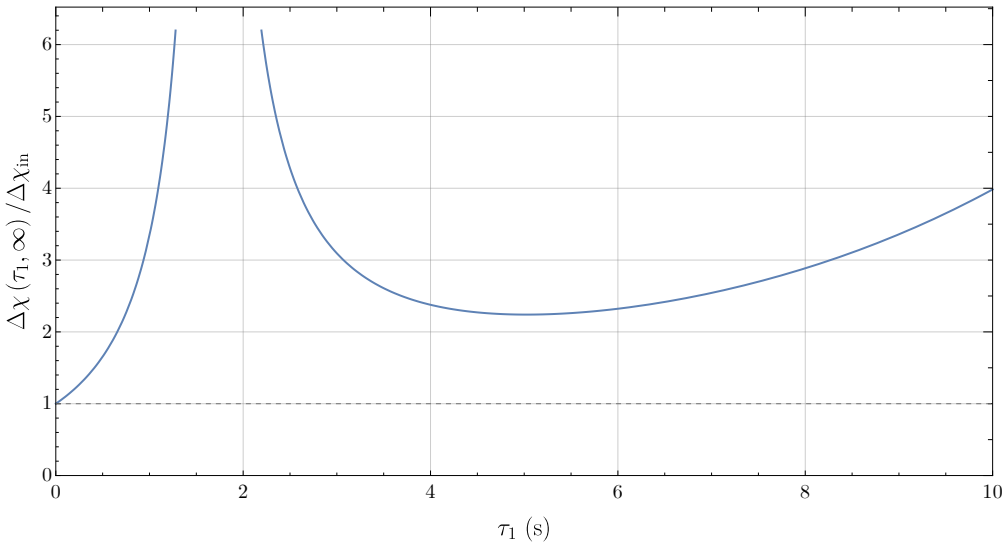

(B) Selection of long times.

FIG. 4.2 – Phase uncertainty $\Delta\chi(\tau_1,\tau_2)$ in relation to the initial $\Delta\chi_{\mathrm{in}}$ for a typical interferogram recorded at the Atominstitut. (A) Selection of short time intervals $[0,\tau_2]$: reduction of phase uncertainty is possible, with a minimum at $\tau_2 \sim 2\,\mathrm{s}$. (B) Selection of long time intervals $[\tau_1,T]$: no reduction in phase uncertainty is possible, with the divergence corresponding to the loss of contrast of the interferogram near $\tau_1 \sim \bar{\tau}$.

4.2 Measurements

In addition to the total neutron counts in a given measuring time (as for a non-time-resolved interferogram), these measurements use the neutron arrival times. This is done using the `National Instruments` FPGA card mentioned in SEC. 3.1.1. With a resolution of 40 MHz, and starting from the system time, the obtained arrival times are written to binary files as follows: One compound file, where the first eight bits denote the detector followed by the arrival time of the observed neutron, and two separate files where only the neutrons arriving in the respective detector are recorded. Currently, only two detectors (O and H) are used, but this structure leaves room for the option of further detectors in future measurements.

For the interference fringes the standard `Mathematica` routine `NonlinearModelFit` was used, with the following options: `ConfidenceLevel` $\rightarrow$ `0.95`, `Method` $\rightarrow$ `LevenbergMarquardt`, `VarianceEstimatorFunction` $\rightarrow$ `(1&)`, `Weights` $\rightarrow$ `1/`σ_{i}^2 (taking into account that the measured data come from a Poisson distribution and therefore each point N carries the statistical error $\sigma_{\mathrm{i}}^2 = \sqrt{N}$). The used cosine model is of the form

$$f(\eta) = y_0 + a\cos\left(f\eta + \varphi\right) , \tag{4.28}$$

with the mean intensity offset y_0, amplitude a, conversion factor f between η in the phase shifter (in deg) and the angle in the cosine function (in rad), dependent on the material and thickness of the phase shifter, and phase offset φ.

For both institutes discussed in the section below, the results are presented in the following order: first, a starting interferogram with no postselection, then an overview of the achieved contrast enhancement, eq. (4.12) for short time intervals for both the O and H detectors, and eq. (4.17) for long time intervals, followed by a selection of interference fringes for different time intervals.

4.2.1 Atominstitut

In addition to the values for the O detector like in [36], these measurements use the H detector as well. Calculations are performed on a typical interferogram recorded on 23.04.2019, with a measuring time of 1200 s per point and 11 phase shifter positions with increments $\Delta\eta = 0.3\,^\circ$. The parameters for the fit function eq. (4.28) are given in TAB. 4.1, and the resulting curves as well as measured neutron counts are shown in FIG. 4.3. The curves for the O and H detector are

$$\begin{aligned} N_{\mathrm{O}}(\eta) &= 729.68 + 294.49\,\cos(4.21\eta + 4.87) \\ N_{\mathrm{H}}(\eta) &= 1206.64 + 270.40\,\cos(4.25\eta + 1.62)\,, \end{aligned} \tag{4.29}$$

giving an initial contrast of

$$\begin{aligned} C_{\mathrm{in,O}} &= 0.4036 \pm 0.0167 \\ C_{\mathrm{in,H}} &= 0.2241 \pm 0.0126\,. \end{aligned} \tag{4.30}$$

With the initial mean intensities $\bar{I}_D$ of $\bar{I}_{\mathrm{O}} = 0.5971\,\mathrm{s}^{-1}$ and $\bar{I}_{\mathrm{H}} = 1.0189\,\mathrm{s}^{-1}$, the mean arrival times $\bar{\tau}_D$ for the two detectors become

$$\begin{aligned} \bar{\tau}_{\mathrm{O}} &= 1.6745\,\mathrm{s} \\ \bar{\tau}_{\mathrm{H}} &= 0.9814\,\mathrm{s}\,. \end{aligned} \tag{4.31}$$

TAB. 4.1 – Resulting fit parameters for the interferogram recorded at the Atominstitut.

	O	H
y_0	729.68 ± 8.36	1206.64 ± 10.60
a	294.49 ± 11.73	270.40 ± 15.01
f	4.21 ± 0.04	4.25 ± 0.06
φ	4.87 ± 0.06	1.62 ± 0.09

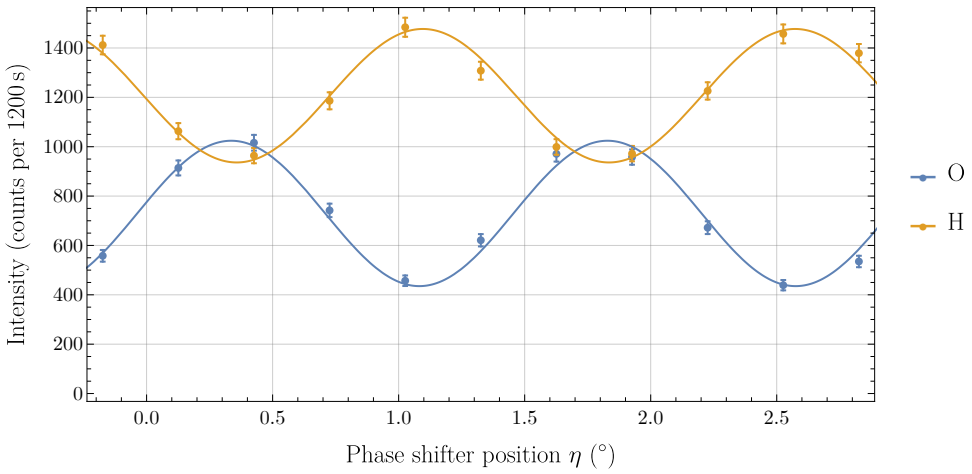

FIG. 4.3 – Starting interferogram for the Atominstitut. Shown are obtained fit curves for O (blue) and H (orange) detectors.

4.2.1.1 Contrast enhancement

From these starting values, a selection of contrast enhancements has been made. An overview of selected short times is given in FIG. 4.4, where shorter times (to the left) achieve a higher improvement to the contrast, and for selected long times in FIG. 4.5, where the reduction of the contrast, zero crossing at approximately $\bar{\tau}_D$, and finally, the achievement of contrast values $\to -1$ after the sign inversion is visible. See also FIG. 4.1 for comparison.

A selection of arrival time intervals causes a reduction of used neutron counts (and therefore higher relative errors). Resulting contrast improvements and the percentage of the used data are presented in TAB. 4.2 for short time intervals, and in TAB. 4.3 for long time intervals.

TAB. 4.2 – Obtained contrast values for selected short times at the Atominstitut as well as the percentage of data used for the given τ_2.

	O detector		H detector	
τ_2	C_O	% used data	C_H	% used data
3 s	0.5321 ± 0.0159	84.07	0.2599 ± 0.0107	95.00
$\bar{\tau}_\mathrm{O}$	0.5945 ± 0.0161	64.24	0.3075 ± 0.0123	81.77
$\bar{\tau}_\mathrm{H}$	0.6335 ± 0.0159	46.19	0.3481 ± 0.0135	63.63
$\frac{1}{2}\bar{\tau}_\mathrm{O}$	0.6421 ± 0.0159	41.16	0.3581 ± 0.0138	57.87
$\frac{1}{2}\bar{\tau}_\mathrm{H}$	0.6633 ± 0.0157	27.07	0.3844 ± 0.0145	40.20
0.1 s	0.6878 ± 0.0154	6.29	0.4177 ± 0.0153	0.99

TAB. 4.3 – Obtained contrast values for selected long times at the Atominstitut as well as the percentage of data used for the given τ_1. For $\bar{\tau}_D$, the contrast in the detector D is almost zero.

	O detector		H detector	
τ_1	C_O	% used data	C_H	% used data
$\bar{\tau}_\mathrm{H}$	0.1849 ± 0.0085	53.81	0.0068 ± 0.0022	36.37
$\bar{\tau}_\mathrm{O}$	0.0170 ± 0.0059	35.76	-0.1483 ± 0.0059	18.23
3 s	-0.2989 ± 0.0083	15.93	-0.4203 ± 0.1430	5.00
5 s	-0.6635 ± 0.0122	5.57	-0.7157 ± 0.0171	0.66

The following figures present the results for selected time intervals. For short arrival time intervals, τ_2 was chosen 3 s (FIG. 4.6), $\bar{\tau}_\mathrm{O} = 1.67$ s (FIG. 4.7), and 0.1 s (FIG. 4.8). For long arrival time intervals, τ_1 was chosen $\bar{\tau}_\mathrm{H} = 0.98$ s (FIG. 4.9), 3 s (FIG. 4.10), and 5 s (FIG. 4.11). In FIG. 4.9 the loss of contrast in the H detector is clearly visible; and in FIG. 4.10 and FIG. 4.11 counts for the H detector are lower than counts in the O detector, which also corresponds to the second domain in FIG. 4.1, where the contribution of the minimum curve dominates.

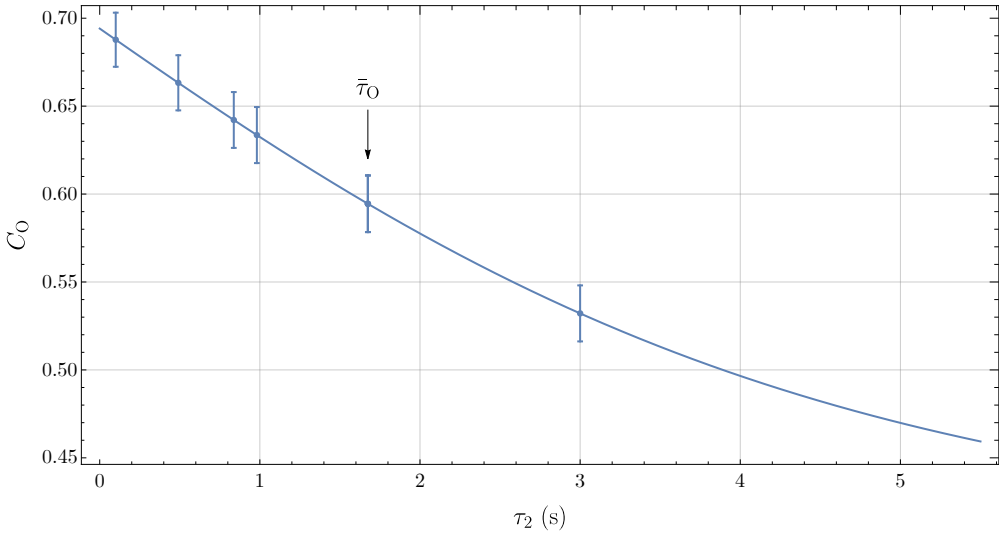

(A) O detector: $C_{\text{in,O}} = 0.40$.

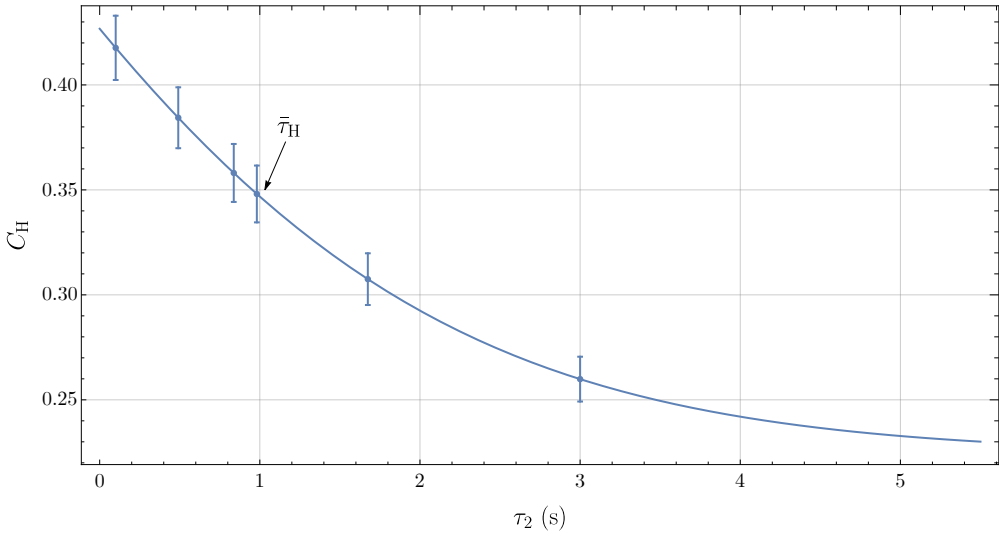

(B) H detector: $C_{\text{in,H}} = 0.22$.

FIG. 4.4 – Possible contrast enhancement curves for selected short time intervals in a typical interferogram recorded at the Atominstitut. Initial contrast values are given, and the curves approach this initial value for longer τ_2. τ_D for the respective detector D is indicated as well. (A) Behaviour for the O detector. (B) Behaviour for the H detector.

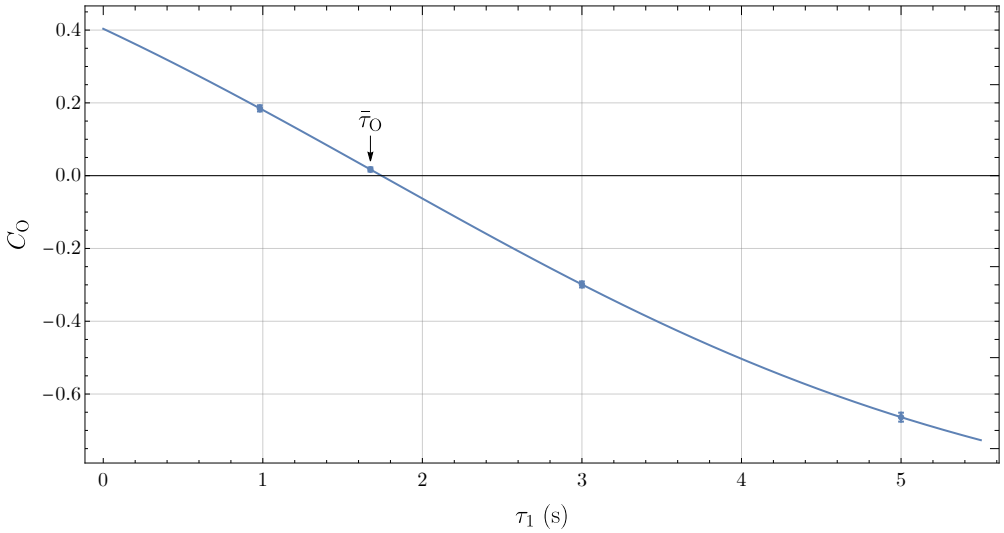

(A) O detector $C_{\mathrm{in,O}} = 0.40$.

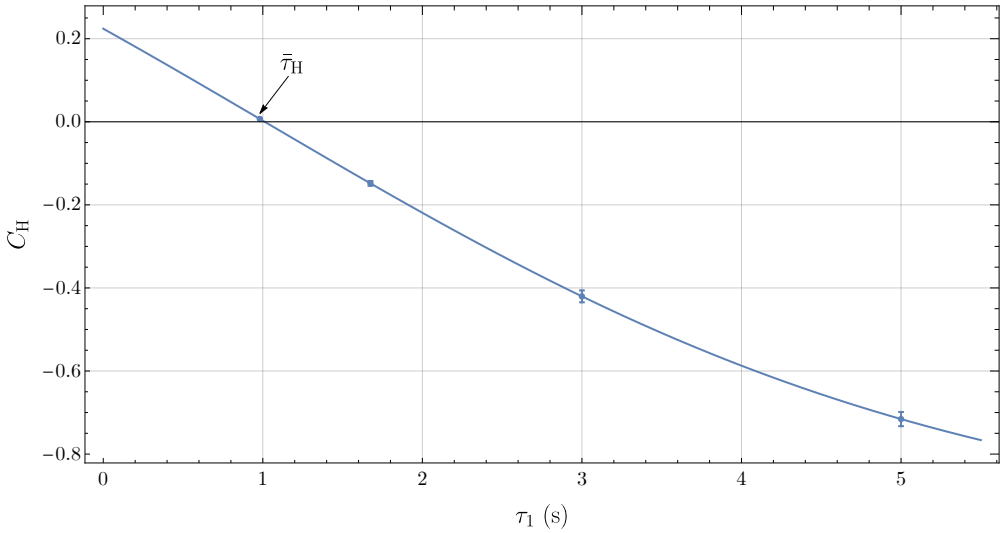

(B) H detector $C_{\mathrm{in,H}} = 0.22$.

FIG. 4.5 – Possible contrast enhancement curves for selected long time intervals in a typical interferogram recorded at the Atominstitut. Initial contrast values are given, and the curves approach this initial value for shorter τ_1. τ_D for the respective detector D is indicated as well and corresponds to the approximate position where the contrast vanishes. For longer τ_1, the contrast approaches values -1. (A) Behaviour for the O detector. (B) Behaviour for the H detector.

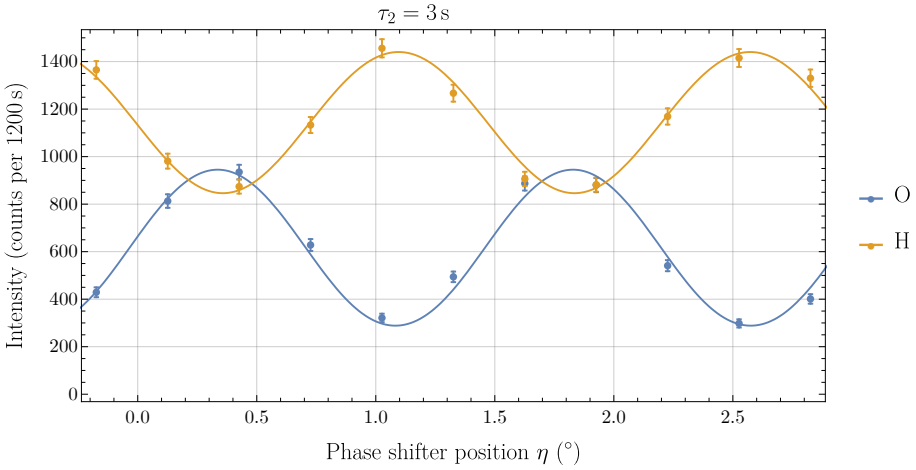

FIG. 4.6 – Selected short arrival time interval with $\tau_2 = 3\,\mathrm{s}$. $C_\mathrm{O} = 0.53$, $C_\mathrm{H} = 0.26$.

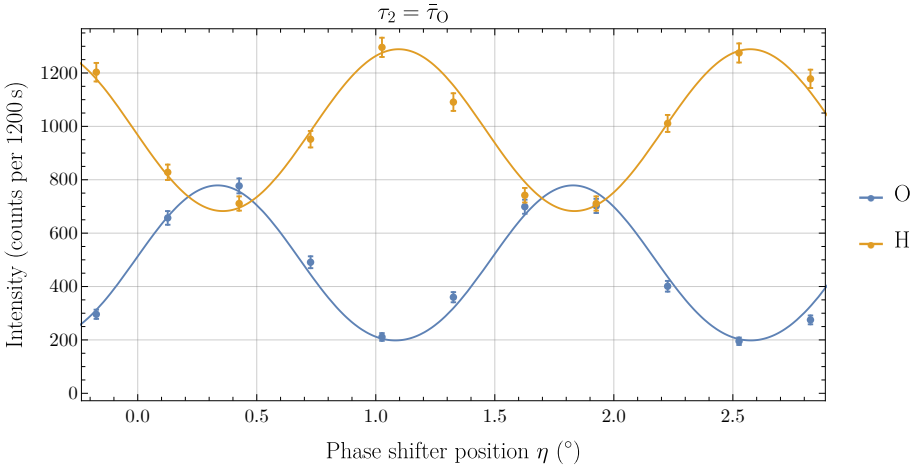

FIG. 4.7 – Selected short arrival time interval with $\tau_2 = \bar{\tau}_\mathrm{O} = 1.67\,\mathrm{s}$. $C_\mathrm{O} = 0.59$, $C_\mathrm{H} = 0.31$.

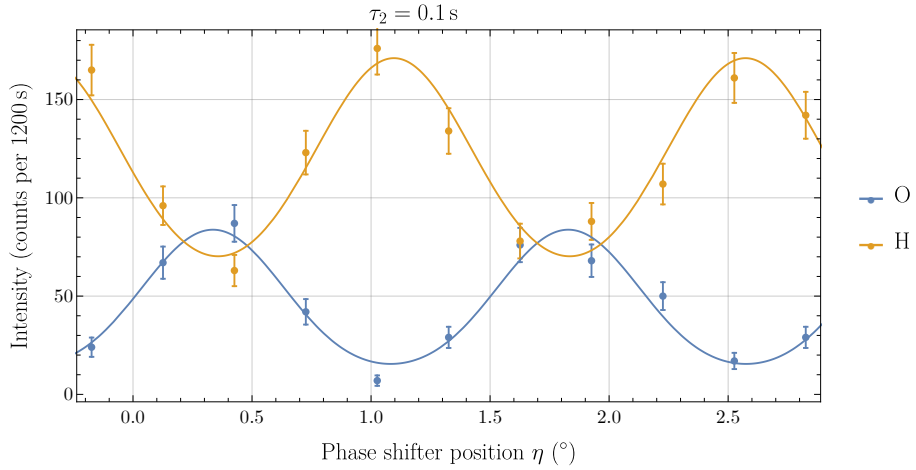

FIG. 4.8 – Selected short arrival time interval with $\tau_2 = 0.1\,\mathrm{s}$. $C_\mathrm{O} = 0.69$, $C_\mathrm{H} = 0.42$.

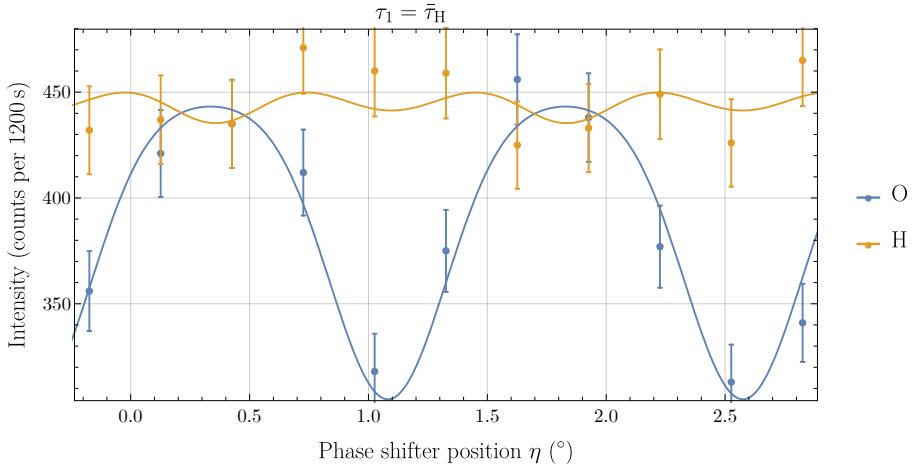

FIG. 4.9 – Selected long arrival time interval with $\tau_1 = \bar{\tau}_H = 0.98\,\text{s}$. $C_O = 0.18$, $C_H = 0.01$.

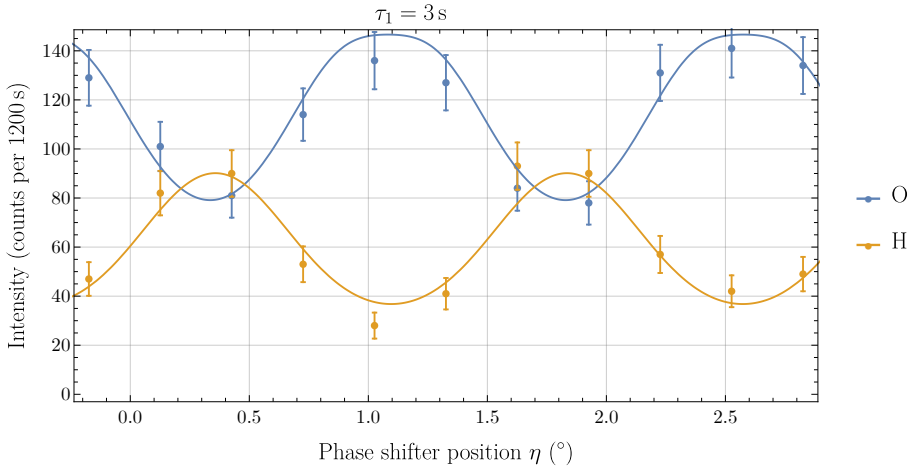

FIG. 4.10 – Selected long arrival time interval with $\tau_1 = 3\,\text{s}$. $C_O = -0.30$, $C_H = -0.42$.

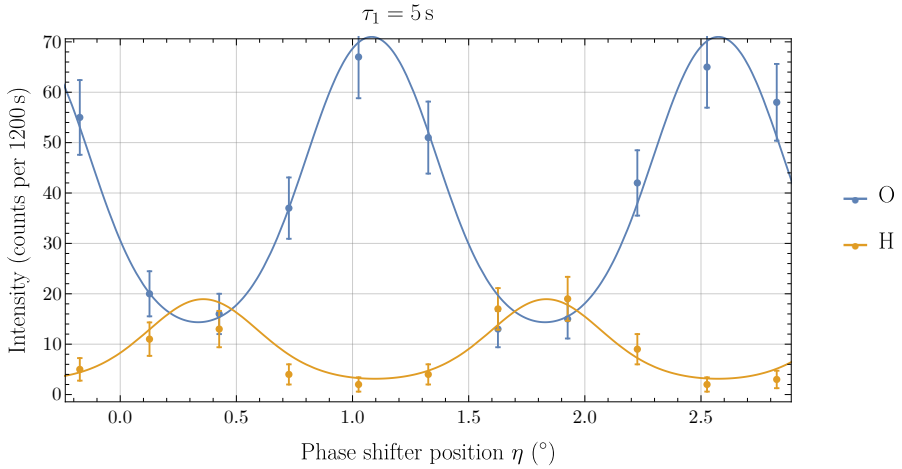

FIG. 4.11 – Selected long arrival time interval with $\tau_1 = 5\,\text{s}$. $C_O = -0.66$, $C_H = -0.72$.

4.2.2 Institut Laue–Langevin

In comparison with the measurements performed at the Atominstitut, measured neutron counts are about a factor 100 higher at the ILL, which allows significantly shorter measuring times. These calculations are performed on a typical interferogram recorded on 16.07.2019, with a measuring time of 600 s per point and 33 phase shifter positions with increments $\Delta\eta = 0.125\,°$. The parameters for the fit function eq. (4.28) are given in TAB. 4.4, and the resulting curves as well as measured neutron counts are shown in FIG. 4.12. The curves for the O and H detector are

$$\begin{aligned} N_{\mathrm{O}}(\eta) &= 34\,522 + 28\,366\,\cos(4.76\eta + 1.47) \\ N_{\mathrm{H}}(\eta) &= 78\,259 + 36\,570\,\cos(4.74\eta + 4.66)\,, \end{aligned} \tag{4.32}$$

giving an initial contrast of

$$\begin{aligned} C_{\mathrm{in,O}} &= 0.8217 \pm 0.0014 \\ C_{\mathrm{in,H}} &= 0.4673 \pm 0.0009\,. \end{aligned} \tag{4.33}$$

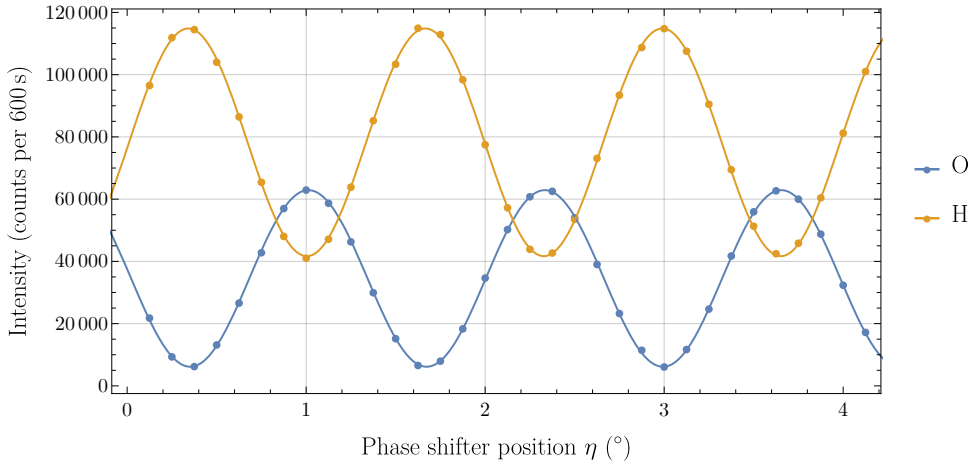

FIG. 4.12 – Starting interferogram for the ILL. Obtained fit curves for O (blue) and H (orange) detectors are shown.

TAB. 4.4 – Resulting fit parameters for the interferogram recorded at the ILL.

	O	H
y_0	$34\,522 \pm 33$	$78\,259 \pm 49$
a	$28\,366 \pm 41$	$36\,570 \pm 67$
f	4.757 ± 0.001	4.745 ± 0.002
φ	1.465 ± 0.003	4.662 ± 0.004

Note that the sum of both detectors also shows a cosine behaviour. A likely explanation is that the H detector was not optimally aligned during measurement.

The difference between the two institutes is further made clear by the fact that $C_{\mathrm{in,H}}$ for the ILL is higher than $C_{\mathrm{in,O}}$ for the Atominstitut; and the maximum reachable contrast for the O detector at the Atominstitut for $\tau_2 \to 0$ according to eq. (4.20) is smaller than the initial O contrast at the ILL: $C^{\mathrm{ATI}}_{\mathrm{max,O}} = 0.80 < C^{\mathrm{ILL}}_{\mathrm{in,O}} = 0.82$. With the initial mean intensities $\bar{I}_D$ of $\bar{I}_{\mathrm{O}} = 56.53\,\mathrm{s}^{-1}$ and $\bar{I}_{\mathrm{H}} = 131.71\,\mathrm{s}^{-1}$, the mean arrival times $\bar{\tau}_D$ for the two detectors become

$$\begin{aligned} \bar{\tau}_{\mathrm{O}} &= 17.689\,\mathrm{ms} \\ \bar{\tau}_{\mathrm{H}} &= 7.592\,\mathrm{ms}\,. \end{aligned} \tag{4.34}$$

4.2.2.1 Contrast enhancement

An overview of selected short times is given in FIG. 4.13, where shorter times (to the left) achieve a higher improvement to the contrast, and for selected long times in FIG. 4.14, where the reduction of the contrast, zero crossing at approximately $\bar{\tau}_D$, and finally, the achievement of contrast values $\to -1$ after the sign inversion is visible. See also FIG. 4.1 for comparison.

Resulting contrast improvements and the percentage of the used data for the ILL are presented in TAB. 4.5 for short time intervals, and in TAB. 4.6 for long time intervals.

TAB. 4.5 – Obtained contrast values for selected short times at the ILL, as well as the percentage of data used for the given τ_2.

	O detector		H detector	
τ_2	C_{O}	% used data	C_{H}	% used data
20 ms	0.9594 ± 0.0006	73.89	0.5641 ± 0.0009	92.25
$\bar{\tau}_{\mathrm{O}}$	0.9622 ± 0.0005	70.13	0.5800 ± 0.0009	89.95
15 ms	0.9654 ± 0.0005	64.95	0.6011 ± 0.0009	86.25
10 ms	0.9710 ± 0.0004	51.77	0.6484 ± 0.0008	74.65
$\bar{\tau}_{\mathrm{H}}$	0.9736 ± 0.0004	43.15	0.6747 ± 0.0008	65.40

TAB. 4.6 – Obtained contrast values for selected long times at the ILL, as well as the percentage of data used for the given τ_1. For $\bar{\tau}_D$, the contrast in the detector D is almost zero.

	O detector		H detector	
τ_1	C_{O}	% used data	C_{H}	% used data
$\bar{\tau}_{\mathrm{H}}$	0.6657 ± 0.0019	56.85	0.0438 ± 0.0004	34.60
$\bar{\tau}_{\mathrm{O}}$	0.3146 ± 0.0028	29.87	-0.5165 ± 0.0005	10.05
30 ms	-0.2508 ± 0.0026	15.12	-0.8673 ± 0.0004	2.72
50 ms	-0.8342 ± 0.0007	6.72	-0.9877 ± 0.0008	0.46

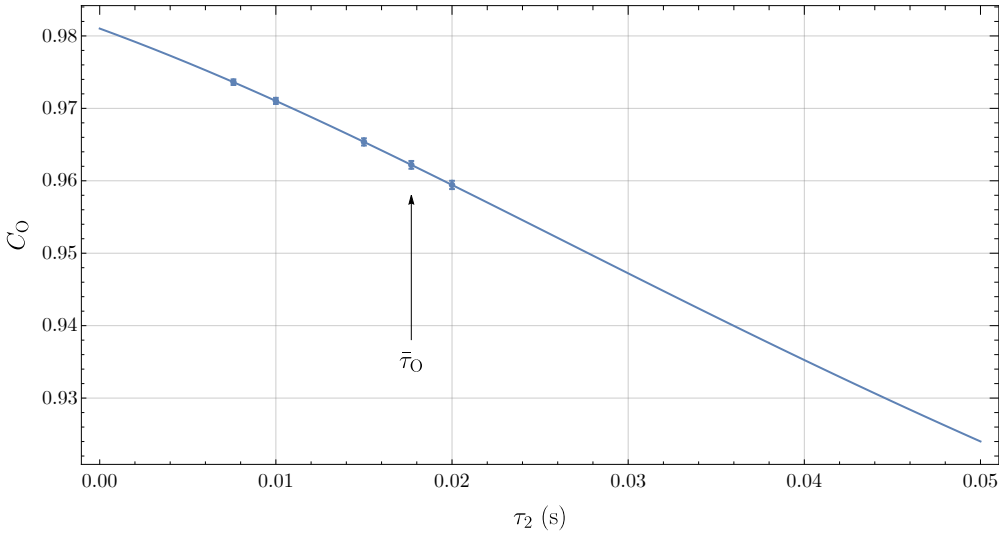

(A) O detector $C_{\mathrm{in,O}} = 0.82$.

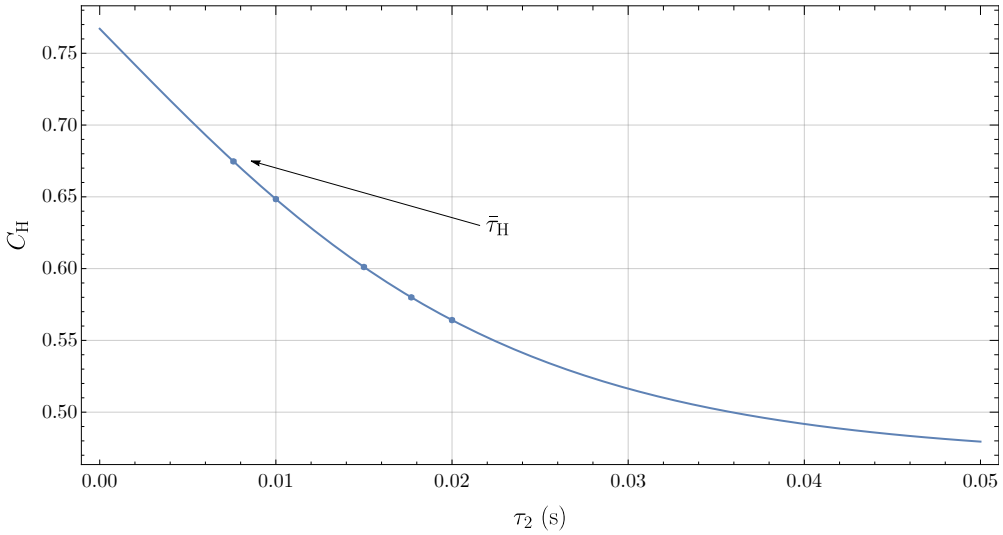

(B) H detector $C_{\mathrm{in,H}} = 0.47$.

FIG. 4.13 – Possible contrast enhancement curves for selected short time intervals in a typical interferogram recorded at the ILL. Initial contrast values are given, and the curves approach this initial value for longer τ_2. τ_D for the respective detector D is indicated as well. (A) Behaviour for the O detector. (B) Behaviour for the H detector.

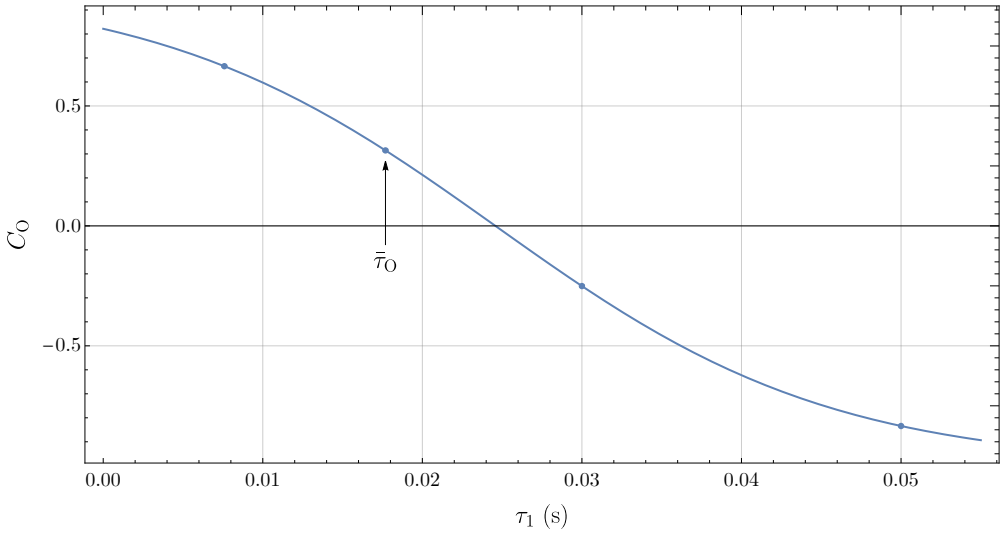

(A) O detector $C_{\text{in,O}} = 0.82$.

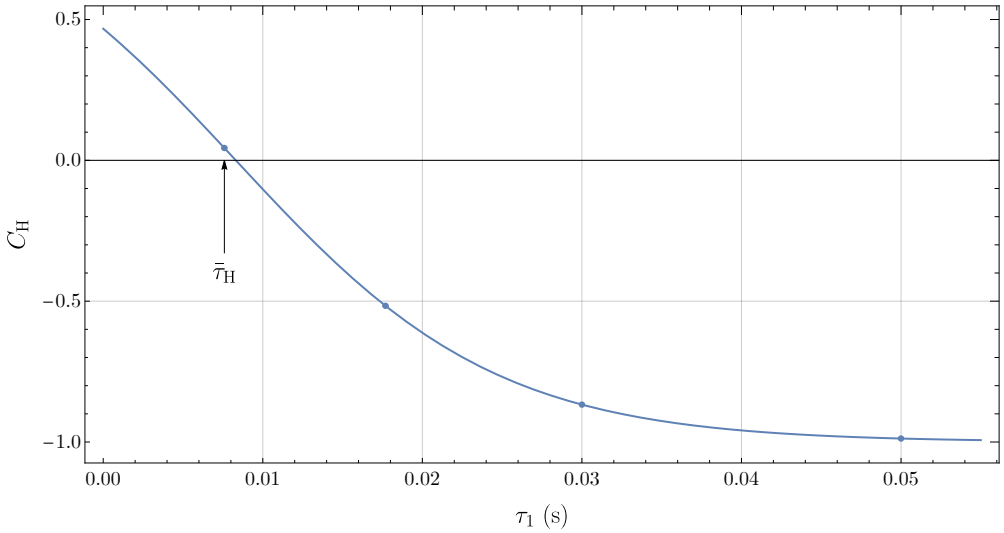

(B) H detector $C_{\text{in,H}} = 0.47$.

FIG. 4.14 – Possible contrast enhancement curves for selected long time intervals in a typical interferogram recorded at the ILL. Initial contrast values are given, and the curves approach this initial value for shorter τ_1. τ_D for the respective detector D is indicated as well and corresponds to the approximate position where the contrast vanishes. For longer τ_1, the contrast approaches values -1. (A) Behaviour for the O detector. (B) Behaviour for the H detector.

The following figures present the results for selected time intervals. For short arrival time intervals, τ_2 was chosen 20 ms (FIG. 4.15), $\bar{\tau}_\mathrm{O} = 17.69$ ms (FIG. 4.16), 15 ms (FIG. 4.17), 10 ms (FIG. 4.18), and $\bar{\tau}_\mathrm{H} = 7.59$ ms (FIG. 4.19).

For long arrival time intervals, τ_1 was chosen $\bar{\tau}_\mathrm{H} = 7.59$ ms (FIG. 4.20), $\bar{\tau}_\mathrm{O} = 17.69$ ms (FIG. 4.21), 30 ms (FIG. 4.22), and 50 ms (FIG. 4.23). Additional zero crossings, corresponding to the case $T_1 g(\chi) = 1$ in eq. (4.18), can be seen, which demonstrates again the usefulness of defining the contrast with fixed phase relations, instead of via minimum and maximum of the respective curve. After the 'phase flip' region in the contrast (clearly visible vor the H detector in FIG. 4.20), the curves for O and H detectors change positions, with H approaching $C \to -1$ faster than O (since the intensity is higher, and therefore the probability for longer waiting times between neutrons lower).

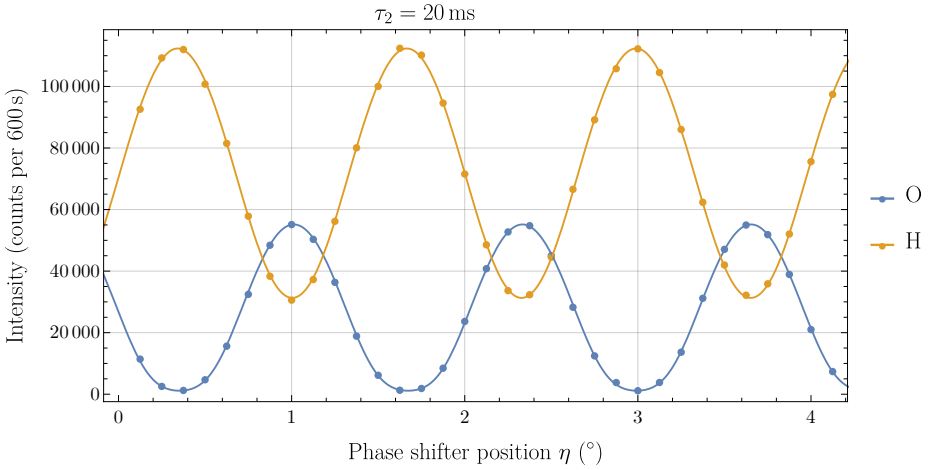

FIG. 4.15 – Selected short arrival time interval with $\tau_2 = 20\,\mathrm{ms}$. $C_\mathrm{O} = 0.96$, $C_\mathrm{H} = 0.56$.

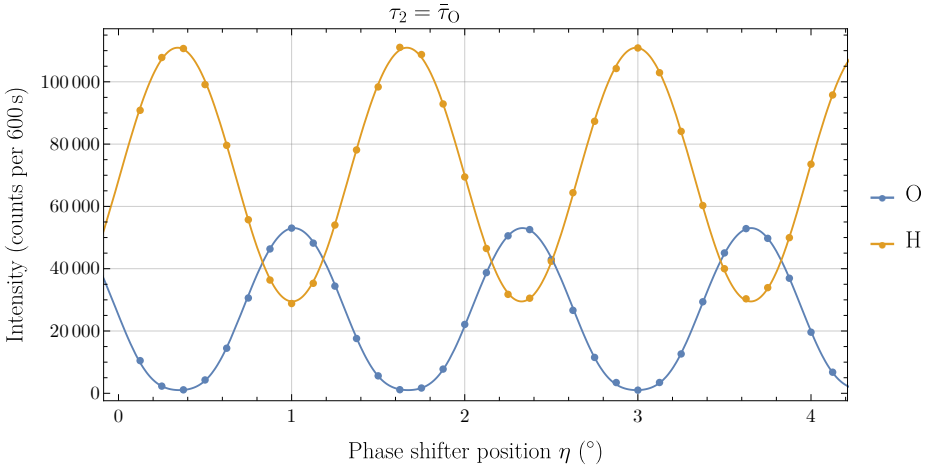

FIG. 4.16 – Selected short arrival time interval with $\tau_2 = \bar{\tau}_\mathrm{O} = 17.69\,\mathrm{ms}$. $C_\mathrm{O} = 0.96$, $C_\mathrm{H} = 0.58$.

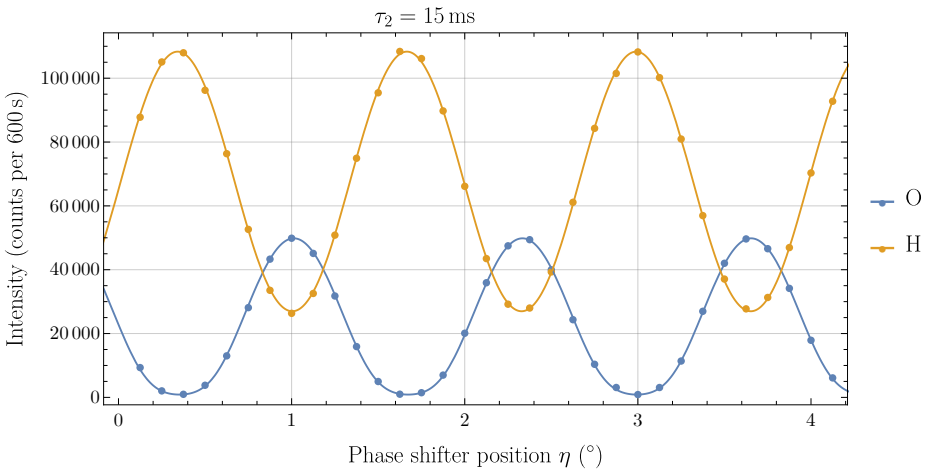

FIG. 4.17 – Selected short arrival time interval with $\tau_2 = 15\,\mathrm{ms}$. $C_\mathrm{O} = 0.97$, $C_\mathrm{H} = 0.60$.

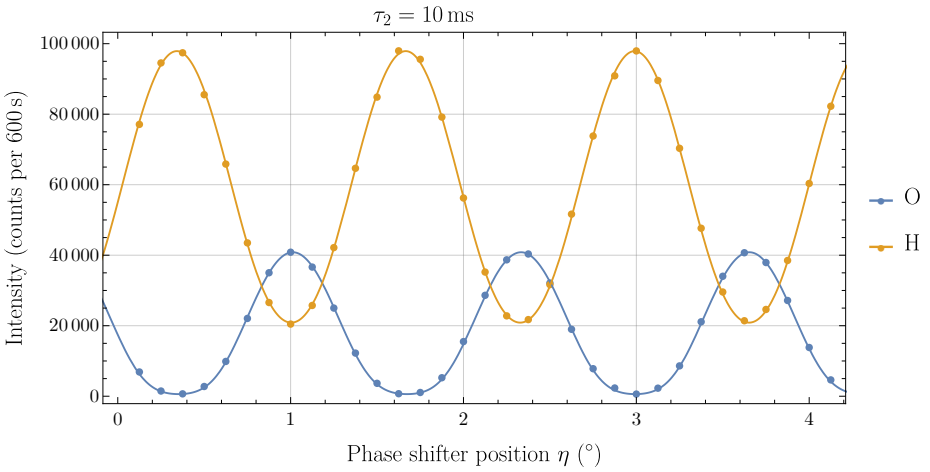

FIG. 4.18 – Selected short arrival time interval with $\tau_2 = 10\,\mathrm{ms}$. $C_\mathrm{O} = 0.97$, $C_\mathrm{H} = 0.65$.

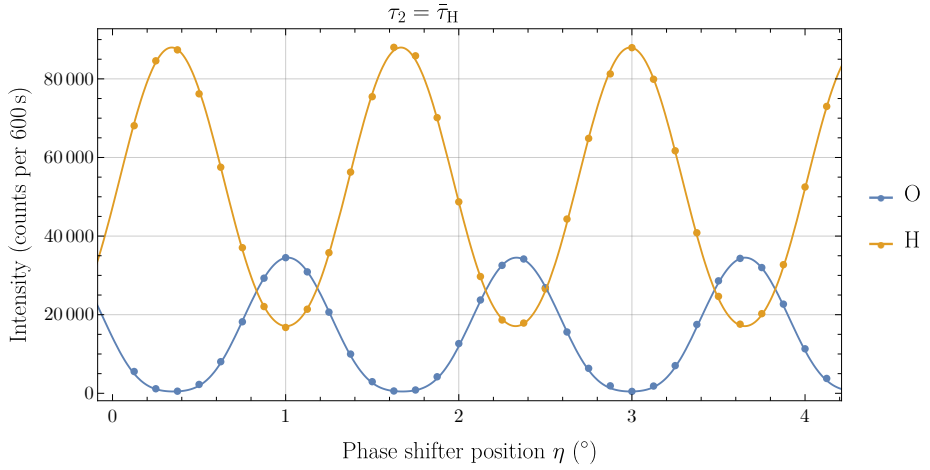

FIG. 4.19 – Selected short arrival time interval with $\tau_2 = \bar{\tau}_\mathrm{H} = 7.59\,\mathrm{ms}$. $C_\mathrm{O} = 0.97$, $C_\mathrm{H} = 0.67$.

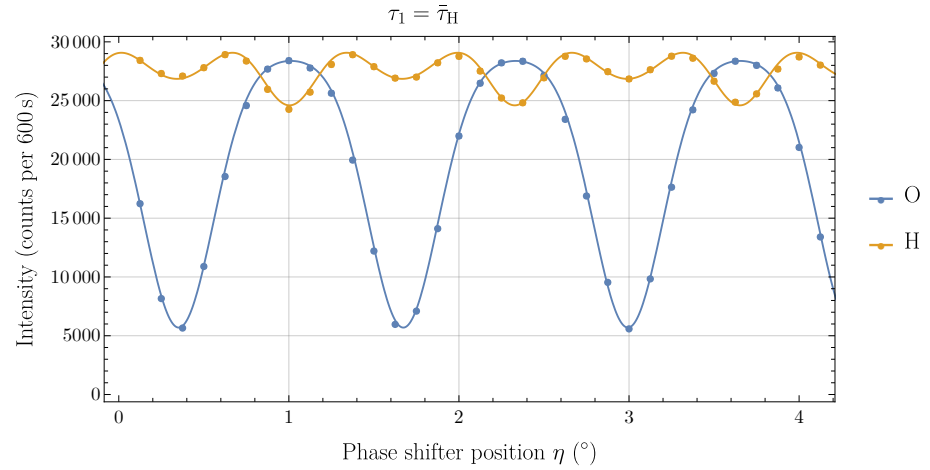

FIG. 4.20 – Selected long arrival time interval with $\tau_1 = \bar{\tau}_\mathrm{H} = 7.59\,\mathrm{ms}$. $C_\mathrm{O} = 0.67$, $C_\mathrm{H} = 0.04$.

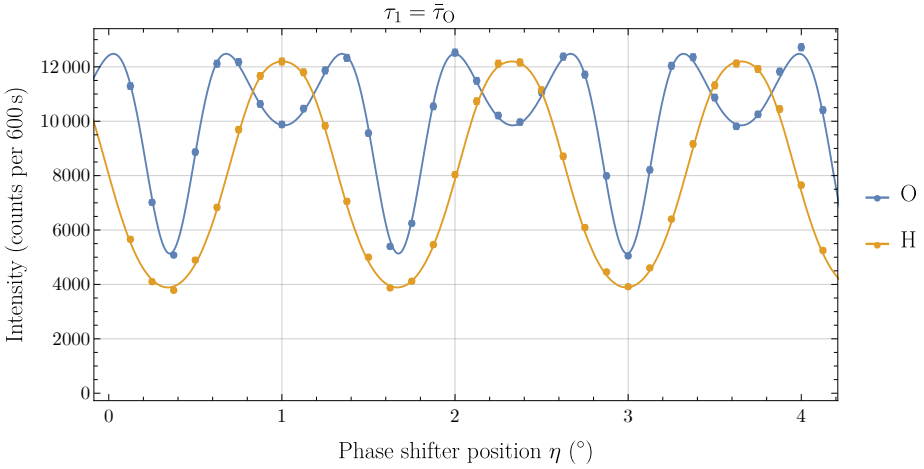

FIG. 4.21 – Selected long arrival time interval with $\tau_1 = \bar{\tau}_O = 17.69\,\text{ms}$. $C_O = 0.31$, $C_H = -0.52$.

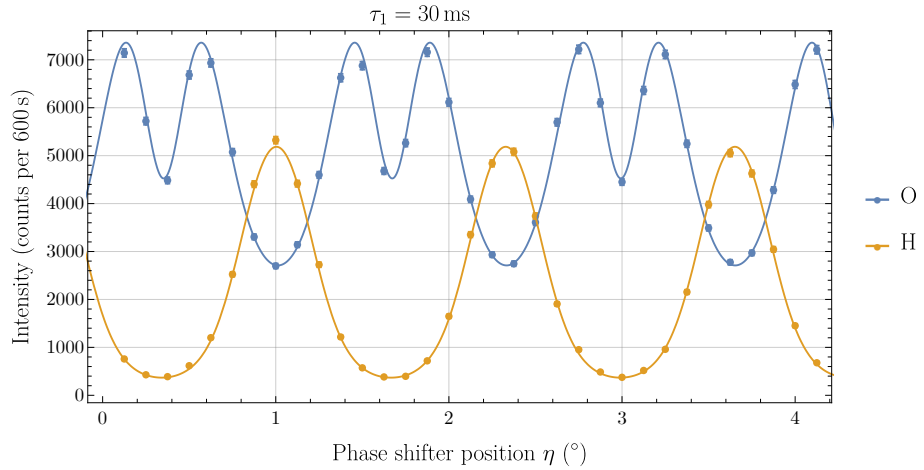

FIG. 4.22 – Selected long arrival time interval with $\tau_1 = 30\,\text{ms}$. $C_O = -0.25$, $C_H = -0.87$.

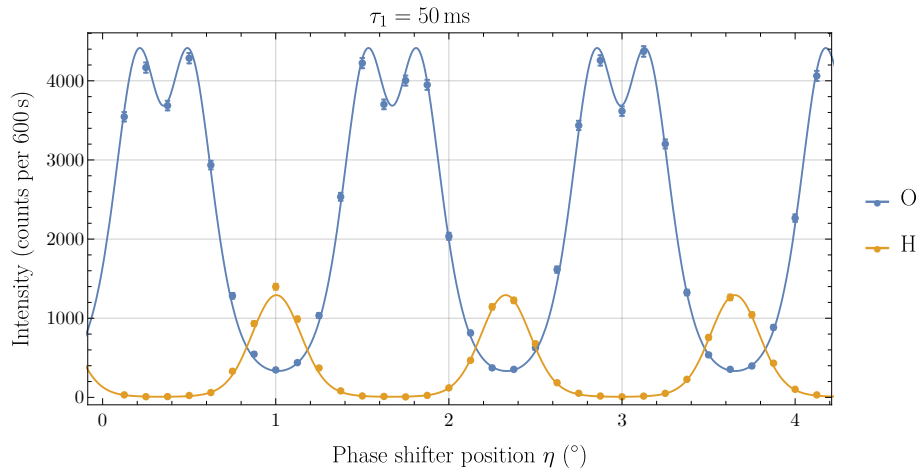

FIG. 4.23 – Selected long arrival time interval with $\tau_1 = 50\,\text{ms}$. $C_O = -0.83$, $C_H = -0.99$.

5 Leggett–Garg inequality

First proposed by Leggett and Garg in 1985 [16], a Leggett–Garg inequality (LGI) provides a tool to measure the 'quantum-ness' of a system and the applicability of quantum mechanical tools in the macroscopic world [55], and can be thought of as a Bell inequality in the time domain.

This chapter discusses the measurement of a violation of an LGI. In [56] Emary et al. proposed an experimental scheme using tunable beam splitters in a Mach–Zehnder interferometer (MZI) to obtain the required correlation functions. In the interferometric approach of this thesis, the non-50:50 beam splitter is realized via the implementation of an absorber in one of the partial beams in the interferometer, thus allowing for a controlled beam attenuation. First, a theoretical overview is presented, followed by a description of measurements and the resulting violation. These measurements were performed in July and August 2019 during `cycle 185/CRG-2643` at the Institut Laue–Langevin (ILL).

5.1 Theoretical background

Analogous to Bell inequalities, where correlations between multiple spatially separated measurement locations of an entangled two-particle system are investigated, LGIs look at temporal correlations within a single system [56]. Analogous to Bell, a formalism is introduced where an inequality is fulfilled by a classical system but violated by a quantum mechanical one. This allows for tests of the 'quantum-ness' (non-classicality) of a system, and presents a tool to investigate the line between classical and quantum physics.

This discussion follows the one given in [57]. To describe how macroscopic objects behave, two assumptions are made to codify reality at the macroscopic level [16, 55]:

> **(A1) Macroscopic realism**
> a macroscopic system with macroscopically distinct states will at all times be in one of the possible states.
>
> **(A2) Non-invasive measurability**
> it is in principle possible to determine the state of that system without any effect on the system or its subsequent dynamics.

A third assumption is often explicitly given as well:

> **(A3) Induction**
> a measurement of the system cannot be affected by what will or will not be measured on the same system later (i.e., it is determined solely by its initial conditions).

These assumptions match the intuition about objects on a classical level, but conflict with quantum mechanics. Assumption **(A1)** contradicts Schrödinger's famous gedankenexperiment wherein the cat is both dead and alive, while **(A2)** contradicts the well-known collapse of the quantum mechanical wave function under measurement [55, 58].

In their 1985 paper, Leggett and Garg examined conditions of the incompatibility of predictions made with the above assumptions with those of quantum mechanics when extrapolated to a macroscopic level, and to what extent these conditions can be met in a realistic experiment. They proposed the investigation of a trapped flux in an rf-SQUID which oscillates between two spatially distinct states in a symmetric potential ("is the flux there when nobody looks?"). The experiment was realised in 2010 by Palacios-Laloy et al [59] – the first experimental violation of an LGI.

The simplest LGI is formulated in the following way:

$$K \equiv C_{21} + C_{32} - C_{31} \leq 1\,, \tag{5.1}$$

with the correlation function

$$C_{\alpha\beta} = \langle Q(t_\alpha) Q(t_\beta) \rangle \tag{5.2}$$

of the dichotomous variable $Q = \pm 1$ at times t_α and t_β. The Leggett–Garg parameter K investigates the question, "how quantum is my system?" [56].

Assumption **(A2)** can be made plausible by introducing ideal negative measurements. The measurement apparatus interacts only for one $Q(t)$ with the system and not at all otherwise. A failure to detect a certain $Q(t)$ means that the system must be in $-Q(t)$, and we suppose that it has also been in this state at t' directly before t (due to macroscopic realism). This holds in the limit for arbitrarily short measuring times, from which follows that the measurement apparatus has not influenced the system [16]. Ideal negative measurements like the ones used for this thesis are a major improvement to Leggett–Garg tests that violate macrorealism while not disturbing the system [17].

Equation (5.1) also has a lower limit, $K \geq -3$. Since each correlator can never exceed the absolute value of 1, this limit can not be violated. The upper limit of $K \leq 1$ can be violated, and it is such a violation that is presented in this thesis.

The following TAB. 5.1 presents an overview of selected LGI test experiments on different systems. This thesis describes a new method of observing LGI violations, using massive particles in an interferometer, which had previously only been discussed theoretically [56, 60].

TAB. 5.1 – Overview of selected LGI experiments. Table taken from [57].

System	Measurement	
superconducting qubit	weak	Palacios-Laloy et al. [59], Groen et al. [61]
nuclear magnetic resonance	projective	Athalye et al.[62], Souza et al. [63]
photons	weak	Goggin et al. [64], Dressel et al. [65]
P impurities in Si	ideal negative	Knee et al. [66]

Proof of the LGI [57] The joint probability $P_{ij}(Q_i, Q_j)$ of obtaining the results $Q_i = Q(t_i)$ and $Q_j = Q(t_j)$ at measurement times t_i, t_j is used to calculate the correlation function

$$C_{ij} = \sum_{Q_i, Q_j = \pm 1} Q_i Q_j P_{ij}(Q_i, Q_j)\,. \tag{5.3}$$

Since Q has to be well-defined at all times, according to assumption **(A1)**, so this two-time probability can be obtained as the marginal of a three-time probability distribution $P_{ij}(Q_3, Q_2, Q_1)$ by adding all contributions of the time between the two measurements,

$$P_{ij}(Q_i, Q_j) = \sum_{Q_k; k \neq i,j} P_{ij}(Q_3, Q_2, Q_1)\,. \tag{5.4}$$

Under assumption **(A2)**, non-invasive measurability, all three $P_{ij}(Q_3, Q_2, Q_1) = P(Q_3, Q_2, Q_1)$, since measurement at different times may not have a different effect on the evolution of the system. With the shorthand $P(+,+,+) = P(+1,+1,+1)$ etc., the correlation functions become

$$\begin{aligned}
C_{21} &= P(+,+,+) - P(+,+,-) - P(-,-,+) + P(-,-,-) \\
&\quad - P(+,-,+) + P(+,-,-) + P(-,+,+) - P(-,+,-) \\
C_{32} &= P(+,+,+) + P(+,+,-) + P(-,-,+) + P(-,-,-) \\
&\quad - P(+,-,+) - P(+,-,-) - P(-,+,+) - P(-,+,-) \\
C_{31} &= P(+,+,+) - P(+,+,-) - P(-,-,+) + P(-,-,-) \\
&\quad + P(+,-,+) - P(+,-,-) - P(-,+,+) + P(-,+,-)\,.
\end{aligned} \tag{5.5}$$

With completeness, $\sum_{Q_3,Q_2,Q_1} = P(Q_3, Q_2, Q_1) \equiv 1$, the Leggett–Garg parameter $K = C_{21} + C_{32} - C_{31}$ results in

$$\begin{aligned}
K =& P(+,+,+) + P(+,+,-) + P(-,-,+) + P(-,-,-) \\
&- 3\,P(+,-,+) + P(+,-,-) + P(-,+,+) - 3\,P(-,+,-) \\
=& 1 - 4\,[P(+,-,+) + P(-,+,-)]\,.
\end{aligned} \tag{5.6}$$

The lower bound of this equation is $K \geq -3$, for $P(+,-,+) + P(-,+,-) = 1$, and the upper bound is $K \leq 1$ for $P(+,-,+) = P(-,+,-) = 0$, giving a range for the parameter K:

$$-3 \leq K \leq 1\,. \tag{5.7}$$

5.1.1 Leggett–Garg inequality in the Mach–Zehnder interferometer

The setup used for the measurements for this thesis is described in [56]: the path which the neutron takes in the MZI defines the variable $Q = \pm 1$. Three regions are defined, which correspond to different regions of the experimental setup: region 1 is before the MZI (incoming neutron beam), region 2 inside (between the first and third plate of the MZI), and region 3 after the MZI, where the O and H detectors are positioned. These three regions form the temporal structure for the experiment that is necessary to generate the correlators.

In FIG. 5.1 the three regions and their corresponding sign conventions are depicted. The incoming wave ψ_{in} is designated 1+ and the detectors O and H get the designations 3− and 3+, respectively. Inside the interferometer (region 2), the upper path (reflected beam, ψ_{II}) is designated 2+, and the lower path (transmitted beam, ψ_{I}) 2−.

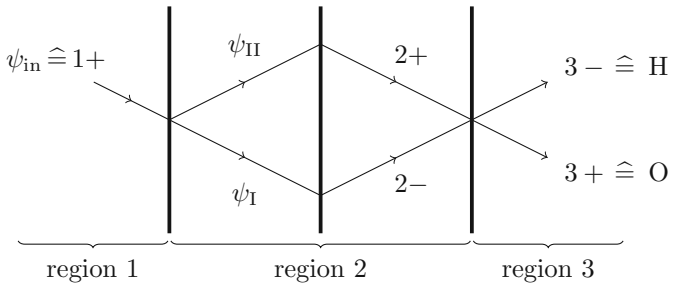

FIG. 5.1 – Sketch of the MZI with the three regions needed for Leggett–Garg measurements. Region 1 is before the interferometer (incoming beam), region 2 inside the interferometer, and region 3 after the interferometer (detectors O and H).

To calculate the three different correlators, $P^D_\alpha(a)$ is defined as the probability that a detector at position α detects ($a = 1$) or does not detect ($a = 0$) the neutron. The correlators C_{31} and C_{21} are more straightforward and take the form

$$C_{31} = P^D_{3+}(1) - P^D_{3-}(1)\,, \tag{5.8}$$

where the neutron is detected in region 3 by the O (3+) or H (3−) detector; and

$$C_{21} = P^D_{2+}(1) - P^D_{2-}(1)\,, \tag{5.9}$$

where a measurement is performed inside the interferometer to determine whether the neutron has taken path I (2−) or path II (2+). For C_{32} the situation is a little more tricky since the measurement in region 2 has to be non-invasive. This is done via an indium absorber in one of the paths, since any neutron that is detected in region 3 has to have taken the non-blocked path. Thus, a measurement can be made without actually observing the neutron. With $q, q' = \pm$, the C_{32} correlator is defined as

$$C_{32} = -\sum_{q,q'=\pm} qq' P^D_{3q,2q'}(1,\cdot)\,, \tag{5.10}$$

where the $\cdot$ represents the fact that no active measurement is performed in region 2.

Note that the signs are chosen differently from [56] – this is an appropriate choice for easier understanding of the different correlators C_{ij}, only the consistency of these signs and their implementation in the calculation of the correlators is important. With the chosen sign convention, C_{31} is the interferogram in the O beam which serves as a definition of $\chi = 0$ (see SEC. 2.2.1 and FIG. 2.9). The signs in region 2 are chosen such that C_{21} is positive, since the In absorber is put in the lower beam.

To calculate the Leggett–Garg parameter K eq. (5.1), the correlations C_{ij} between the different regions in the interferometer are needed. For C_{32}, non-invasive negative measurements are essential for region 2 – but since no subsequent measurement is performed after measuring C_{31} and C_{21}, those measurements need not be non-invasive [56]. The [56] setup does not use time-resolved measurements, but the measurements in the course of this thesis record neutron arrival time as well, which is additional information that can be used to further investigate violations of LGIs.

5.2 Measurements

In this section the setup and measurement process for each of the correlators C_{ij} is discussed for various thicknesses of the In absorber. These results are then combined to calculate the Legget–Garg parameter K. A calculation of the C_{ij} and K via the A and B parameters of the interferometer, when an absorber is present, follows, as well as the description of the Bloch sphere to visualise the loss of contrast.

5.2.1 C_{31}

The correlator C_{31} is dependent on the phase shift χ. To measure this, an interferogram is recorded, from which C_{31} is calculated as follows

$$C_{31} = \frac{N_{3+1+} - N_{3-1+}}{N_{3+1+} + N_{3-1+}}\,, \tag{5.11}$$

in which N_{3+1+} designates the counts in the O detector, and N_{3-1+} the counts in the H detector for a given phase shifter position. The maximum value for C_{31}, leading to the largest violation of the LGI, is reached for minimal counts in O and maximal counts in H, therefore at $(2n+1)\,\pi$ since $\chi = 0$ was defined as the maximum in O.

The results of these measurements at $\chi = (2n+1)\pi$ (maximum violation) are given in TAB. 5.2. For each of the measurements with different In thickness, N_{3+1+} corresponds to the minimal counts in the O detector, and N_{3-1+} to the maximal counts in the H detector. These values are obtained from the cos-fit function to the interferogram, and the respective contrast in the detectors (C_O, C_H) is also shown, along with the resulting correlator C_{31}.

TAB. 5.2 – Results of the C_{31} measurements at $\chi = (2n+1)\pi$ for In absorber of thickness d.

d	N_{3+1+}	C_O	N_{3-1+}	C_H	C_{31}
–	1060 ± 33	80.4%	$14\,442 \pm 120$	44.0%	-0.863 ± 0.004
1 mm	2877 ± 54	74.8%	$31\,236 \pm 177$	37.7%	-0.831 ± 0.003
3 mm	5621 ± 75	37.5%	$22\,681 \pm 151$	17.4%	-0.603 ± 0.005

In the following figures, the measurements for C_{31} are shown for various thickness of In in path I. The first, FIG. 5.2, shows the resulting interferogram and corresponding cos-fit without an absorber, at a measuring time of 60 s. FIGURES 5.3 and 5.4 depict the measurements for 1 mm and 3 mm, respectively, both at a measuring time of 180 s. The loss of intensity due to the absorber is clearly visible in the latter figures. Fit parameters are given in TAB. 5.3. Note that the sum O + H does not show the sin-like behaviour discussed in SEC. 4.2.2, which can be seen from the values of the fit parameter a for O and H for each In thickness d.

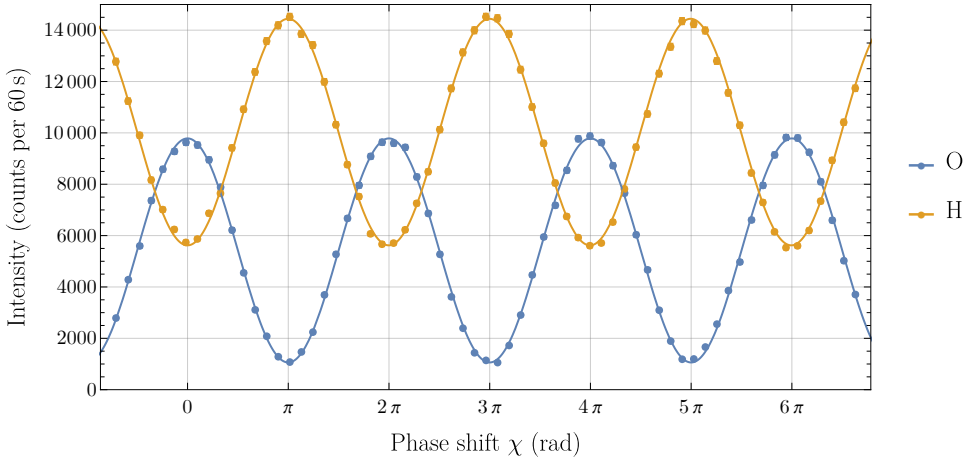

FIG. 5.2 – Interferogram for C_{31} without In absorber: measured counts in 60 s and corresponding fit curves for detectors O (blue) and H (orange).

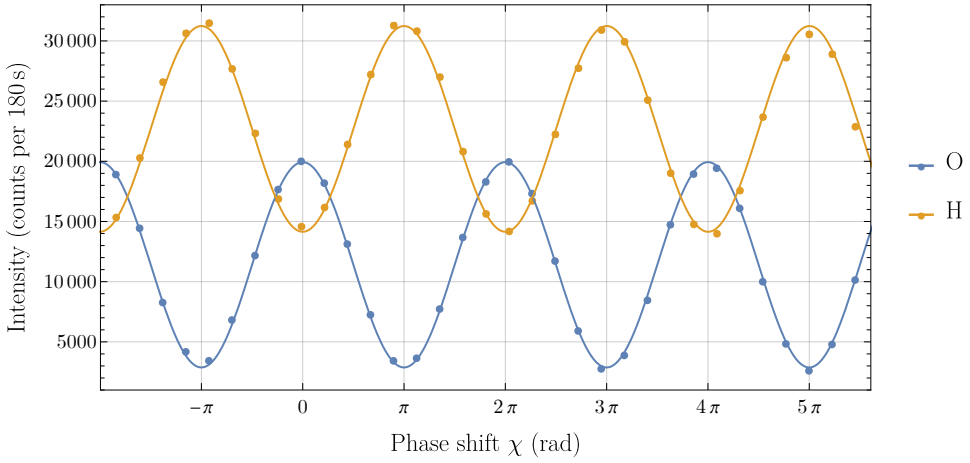

FIG. 5.3 – Interferogram for C_{31} with 1 mm In absorber: measured counts in 180 s and corresponding fit curves for detectors O (blue) and H (orange).

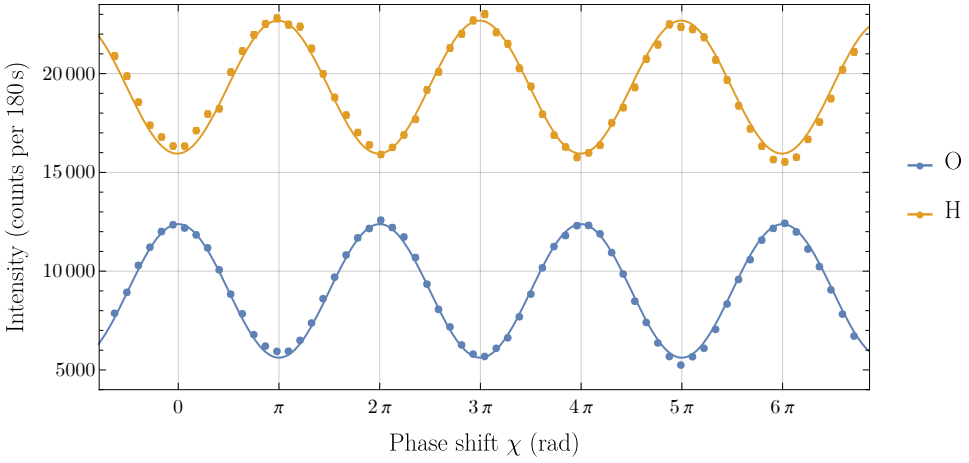

FIG. 5.4 – Interferogram for C_{31} with 3 mm In absorber: measured counts in 180 s and corresponding fit curves for detectors O (blue) and H (orange).

TAB. 5.3 – Fit parameters of the interferogram curves $I(\eta) = y_0 + a\cos(f\eta + \varphi)$ for C_{31} measurements with phase shifter angle η and In absorber of thickness d.

d	–	1 mm	3 mm	
y_0	5422 ± 16	11 403 ± 35	9000 ± 21	O
a	4362 ± 22	8526 ± 49	3380 ± 30	O
f	3.600 ± 0.003	3.579 ± 0.003	3.600 ± 0.004	O
φ	15.909 ± 0.106	19.455 ± 0.124	16.150 ± 0.182	O
y_0	10 032 ± 17	22 692 ± 75	19 316 ± 36	H
a	4411 ± 25	8544 ± 106	3365 ± 52	H
f	3.603 ± 0.003	3.577 ± 0.006	3.597 ± 0.008	H
φ	18.910 ± 0.116	35.235 ± 0.265	19.400 ± 0.318	H

5.2.2 C_{21}

For the C_{21} correlator, measuring non-invasively is not important, since there are no successive measurements in this setup [56]. C_{21} is independent of χ because the sub-beams are not recombined, and therefore no interference occurs. One pencil detector was mounted on a linear translation stage (see SEC. 3.2.1.5 and FIG. 5.5), and afterwards cross-checked with two pencil detectors mounted successively behind a pinhole aperture for further accuracy.

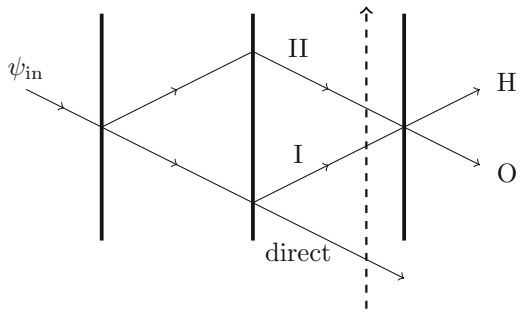

FIG. 5.5 – Path of the C_{21} measurements. The dashed line indicates the direction of detector movement, passing first through the direct beam, then through paths I and II.

The correlator is calculated as follows

$$C_{21} = \frac{N_{2+1+} - N_{2-1+}}{N_{2+1+} + N_{2-1+}} \,. \tag{5.12}$$

The counts N_{2+1+} and N_{2-1+} are obtained via a Gaussian fit to the resulting raster scan, and taking the maximum value of the corresponding peak for paths I and II. These measurements and the respective Gauss fit curves are shown in FIG. 5.6 for measurement without In, FIG. 5.7 for 1 mm In and FIG. 5.8 for 3 mm In with two pencil detectors. The differences in peak position for the three measurements are due to the limitations of the translation stage and varying position of the rastering detector between the plates of the interferometer and are not problematic since the counts for the correlators are normalised. The results are given in TAB. 5.4.

TAB. 5.4 – Results of the C_{21} measurements for In absorber of thickness d and measuring time T.

d	N_{2-1+}	N_{2+1+}	T	C_{21}
–	1061 ± 33	1403 ± 37	10 s	0.139 ± 0.020
1 mm	1511 ± 39	4472 ± 67	30 s	0.495 ± 0.011
3 mm	2061 ± 45	$40\,439 \pm 201$	300 s	0.903 ± 0.002

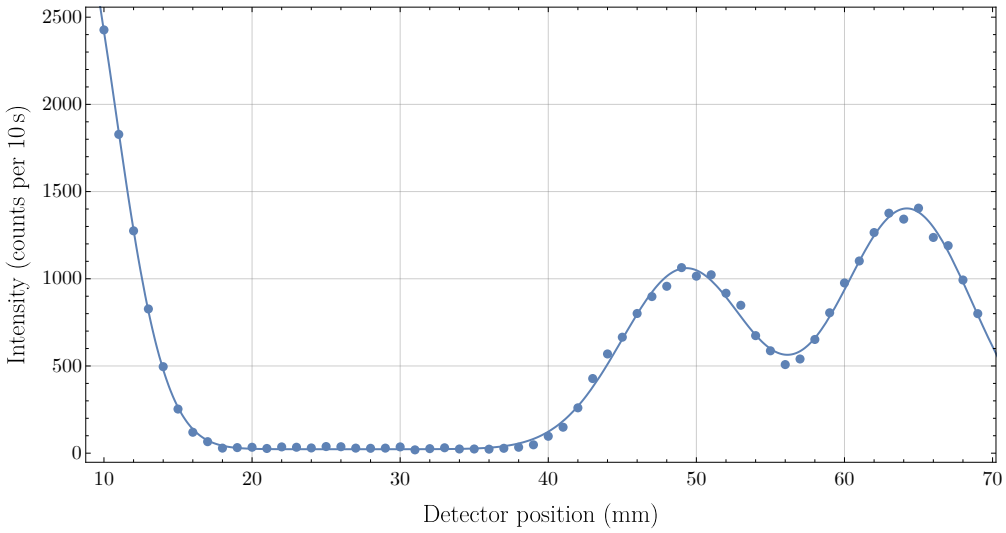

FIG. 5.6 – Raster scan for C_{21} without In in path I. Count values per 10 s and resulting fit curve are shown. The spatial separation between paths I and II is clearly visible, as well as part of the direct beam ψ_{in} (to the left).

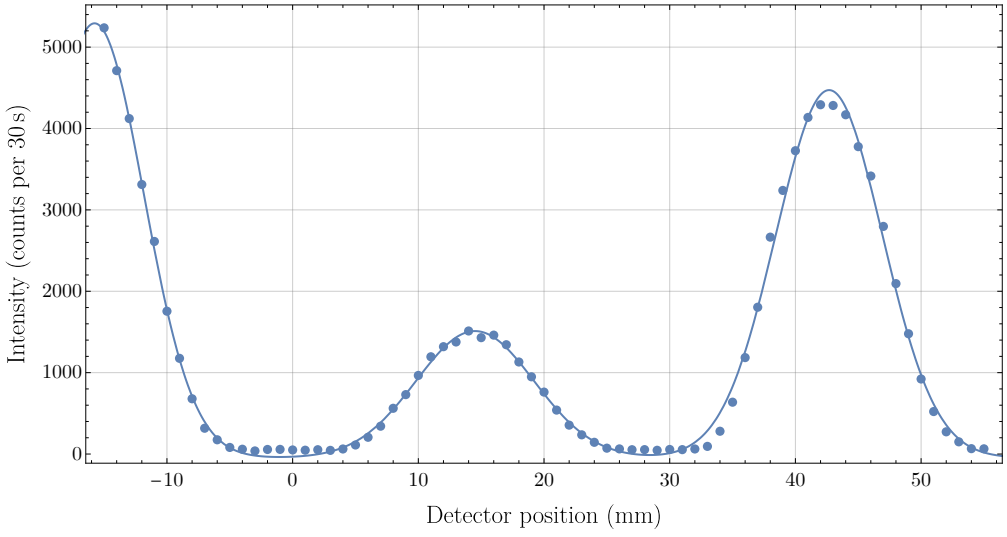

FIG. 5.7 – Raster scan for C_{21} with 1 mm In in path I. Count values per 30 s and resulting fit curve are shown.

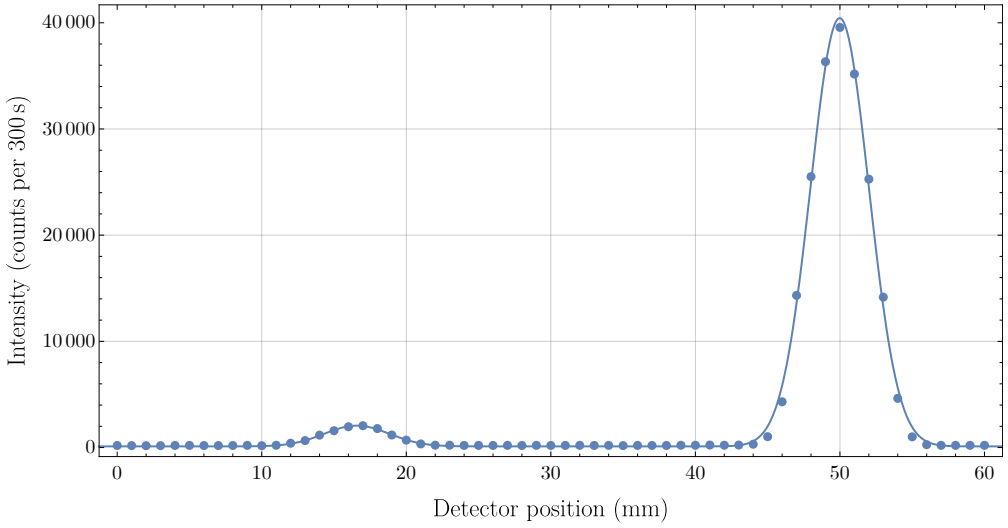

FIG. 5.8 – Raster scan for C_{21} with 3 mm In in path I. Count values per 300 s and resulting fit curve are shown. The diminished intensity and therefore longer measuring time is due to the presence of the second pencil detector and pinhole aperture.

5.2.3 C_{32}

This correlator is the most complex one. For this measurement, both the Cd blockers and the In absorber are used. One of the neutron paths, either I or II, is blocked (indicated by $2\pm$) and the total counts in the O and H beam (indicated by $3\pm$) are recorded (see also SEC. 2.2.1.2). Since there is no neutron at -1, the corresponding probabilities are zero, and C_{32} from eq. (5.5) becomes

$$C_{32} = P(+,+,+) + P(-,-,+) - P(+,-,+) - P(-,+,+)\,. \tag{5.13}$$

Non-invasive measurement in region 2 is crucial for this correlator. The minus sign in eq. (5.10) accounts for the fact that the *absence* of the neutron in a specific path (due to the Cd blocker) is recorded, not the signal of the neutron itself. With the four necessary neutron count rates, C_{32} is calculated as

$$C_{32} = \frac{N_{3+2-} + N_{3-2+} - N_{3+2+} - N_{3-2-}}{N_{3+2-} + N_{3-2+} + N_{3+2+} + N_{3-2-}}\,. \tag{5.14}$$

The $N_{3\pm2\pm}$ correspond to the following cases: N_{3-2-} are the counts in detector H with Cd blocker in path II (since the neutron has to take path I $\widehat{=}\,2+$); N_{3-2+} are the counts in detector H with Cd blocker in path I; and N_{3+2+} and N_{3+2-} are the counts in detector O with Cd blocker in path I and II, respectively. A schematic of the setup for this measurement is shown in FIG. 5.9.

The results are presented in TAB. 5.5. For the three cases without In, with 1 mm In and 3 mm In in path I, the neutron counts of the O and H detector for a given measuring time are recorded for the Cd beam blocker in path I and II. This table also shows the fundamental asymmetry of the two paths in the MZI: in the measurement with no In absorber, the counts in the O detector are

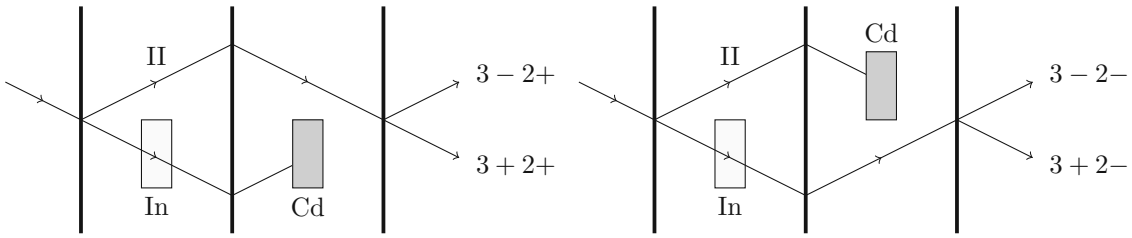

(A) Cadmium blocker in path I.

(B) Cadmium blocker in path II.

FIG. 5.9 – Setup for the measurement of C_{32}. The In absorber is positioned in path I. (A) Cd blocker in path I: the neutron has to take path II (2+). (B) Cd blocker in path II: the neutron has to take path I (2−).

the same regardless of the position of the Cd blocker, while the counts in the H detector differ in the two cases. Note that the values do not match the ones given in SEC. 2.2.1.2. A possible explanation for this is that the interferometer used for the measurements was compromised due to a collision with the translation robot and had to undergo re-etching [33] (also mentioned in SEC. 3.2.1.2).

TAB. 5.5 – Results of the C_{32} measurements with In absorber thickness d and measuring time T.

d	Cd in path	counts O	counts H	T	C_{32}
–	I	2584 ± 51	5819 ± 76	60 s	-0.131 ± 0.008
	II	2464 ± 50	3781 ± 61		
1 mm	I	2628 ± 51	5802 ± 76	60 s	-0.229 ± 0.009
	II	1216 ± 35	1771 ± 42		
3 mm	I	$26\,787 \pm 164$	$59\,232 \pm 243$	600 s	-0.343 ± 0.002
	II	2285 ± 48	3278 ± 57		

5.2.4 Leggett–Garg parameter K

Taking the correlators C_{ij} discussed in the above sections and putting them in eq. (5.1),

$$K = C_{21} + C_{32} - C_{31}\,, \tag{5.15}$$

gives the results presented in the following figures. For the measurement without the In absorber, shown in FIG. 5.10, a violation is not possible. In FIG. 5.11 and FIG. 5.12 the violation of the Leggett–Garg inequality is clearly visible for an absorber thickness of 1 mm In and 3 mm In in beam I, respectively.

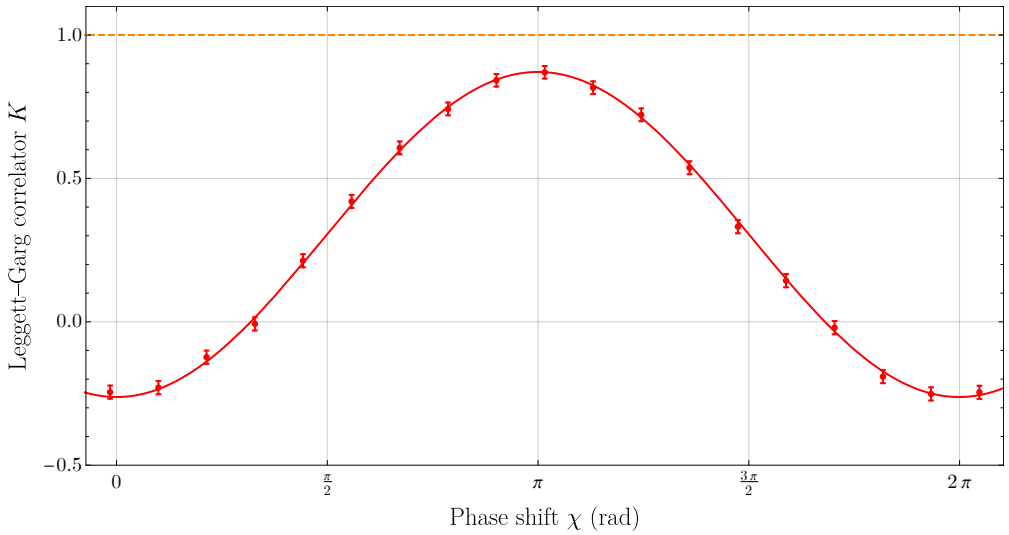

FIG. 5.10 – Parameter K for the measurement without an In absorber in path I. The measured neutron counts and corresponding fit function are shown in red. No violation of the LGI (limit indicated by the dashed orange line) is observed.

In TAB. 5.6, the results for the Leggett–Garg measurements are presented. For 1 mm and 3 mm In, as well as without an absorber, the three correlators C_{ij} and the resulting parameter K are given, as well as the distance of standard deviations n_σ from the measured K to the theoretical maximum of 1. The maximum possible violation for a two-level system is $K = 1.5$ [57].

TAB. 5.6 – Overview of the results of the three correlators C_{ij} and the Leggett–Garg parameter K for the different thickness d of the In absorber in path I.

d	C_{21}	C_{32}	C_{31}	K	n_σ
–	0.139 ± 0.020	-0.131 ± 0.008	-0.863 ± 0.004	0.871 ± 0.022	–
1 mm	0.495 ± 0.011	-0.229 ± 0.009	-0.831 ± 0.003	1.097 ± 0.014	7.2
3 mm	0.903 ± 0.002	-0.343 ± 0.002	-0.603 ± 0.005	1.162 ± 0.006	28.5

These results clearly show a violation for the cases where it is in principle possible to observe. Both 1 mm and 3 mm In foils change the beam splitter from its initial 50:50 ratio, resulting in $K > 1$, which shows that the quantum mechanical MZI is, indeed, not classical.

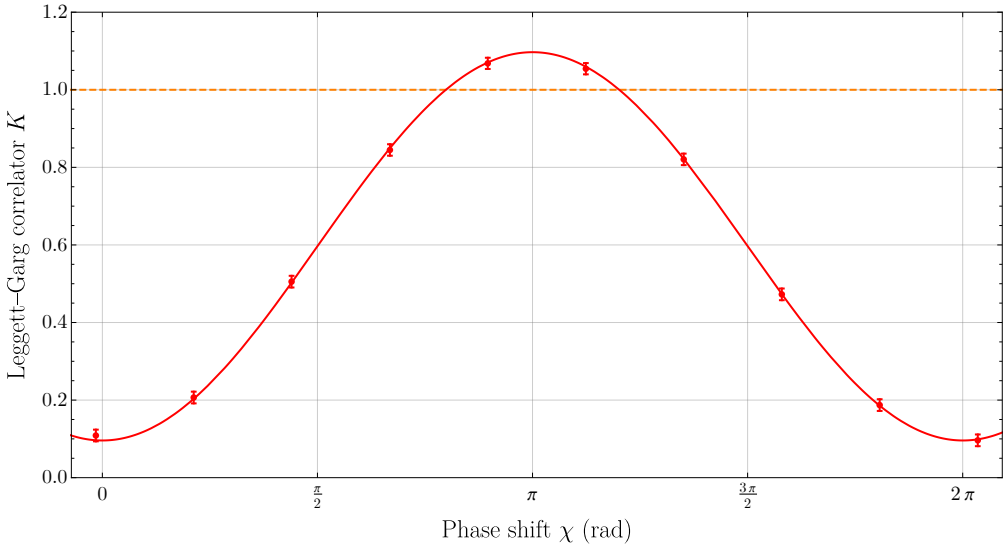

FIG. 5.11 – Parameter K for the measurement with 1 mm In absorber in path I. The measured neutron counts and corresponding fit function are shown in red. A violation of the LGI of more than $7\,\sigma$ (limit indicated by the dashed orange line) is clearly visible.

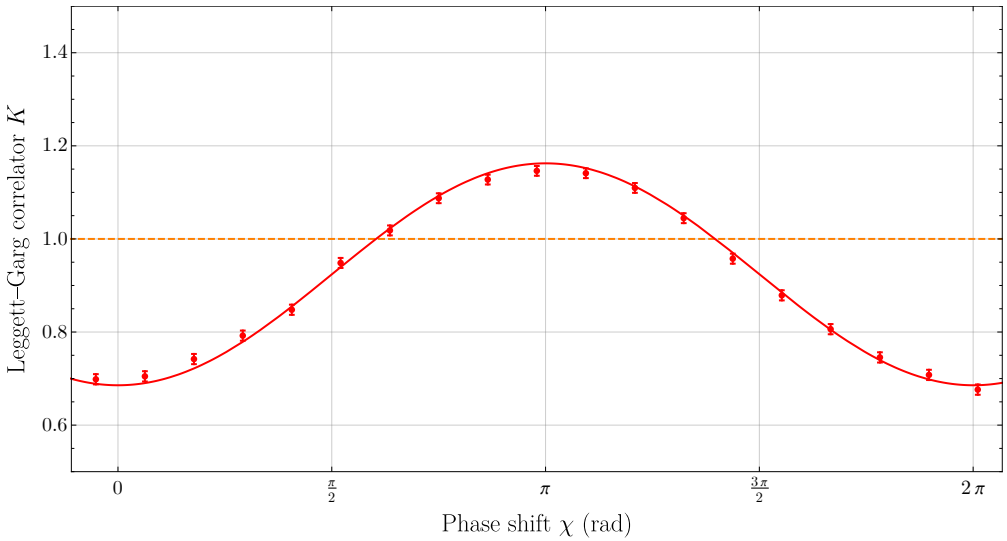

FIG. 5.12 – Parameter K for the measurement with 3 mm In absorber in path I. The measured neutron counts and corresponding fit function are shown in red. A violation of the LGI of more than $28\,\sigma$ (limit indicated by the dashed orange line) is clearly visible.

5.2.5 Calculation of C_{ij} and K via interferometer parameters A and B

To check the consistency of the achieved correlators C_{ij}, one can compare them to a calculation, starting from the interferometer parameters A and B of the O and H beam intensities. The intensities I detected by the O and H detectors, as given in eq. (2.14), change when an absorber is present in one of the neutron beam paths. In FIG. 5.13, a schematic of a single beam splitter (interferometer plate) with an absorber (thickness d) in the transmitted direction is shown. The partial wave in path II is not influenced by the presence of the absorber.

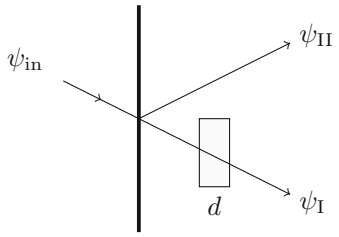

FIG. 5.13 – Schematic of a single beam splitter with absorber of thickness d in path I (transmitted beam).

With consideration of the Beer–Lambert law eq. (2.8), the amplitudes for the partial waves for the transmitted (ψ_{I}) and reflected (ψ_{II}) beam can be written as follows

$$\begin{aligned} \psi_{\mathrm{II}} &= r\,\psi_{\mathrm{in}} \\ \psi_{\mathrm{I}} &= t\;\mathrm{e}^{-\frac{1}{2}\Sigma d}\,\psi_{\mathrm{in}}\,, \end{aligned} \tag{5.16}$$

with reflection and transmission amplitudes r and t, respectively. The factor $\frac{1}{2}$ is due to the fact that the Beer–Lambert law applies to intensities, while we consider amplitudes. Using $\alpha^2 = \mathrm{e}^{-\Sigma d}$, the intensity for the O beam becomes

$$I_{\mathrm{O}} = |\psi_{\mathrm{I,O}} + \psi_{\mathrm{II,O}}|^2 = \left|t\alpha r r\,\psi_0\;\mathrm{e}^{\mathrm{i}\chi_1} + r r t\,\psi_0\;\mathrm{e}^{\mathrm{i}\chi_2}\right|^2\,, \tag{5.17}$$

resulting in

$$I_{\mathrm{O}} = A\left(\frac{1+\alpha^2}{2} + \alpha\,C\,\cos\chi\right) \tag{5.18}$$

where $A = 2\,|\psi_0|^2|t|^2|r|^4 = A_{\mathrm{I}} + A_{\mathrm{II}}$ as before (both paths contribute equally), and C the contrast. This corresponds to eq. (2.12), where no absorber is present (see SEC. A.1 for a detailed derivation).

Doing the same for the H beam (see eq. (2.13) without absorber) gives

$$I_{\mathrm{H}} = |\psi_{\mathrm{I,H}} + \psi_{\mathrm{II,H}}|^2 = \left|t\alpha r t\,\psi_0\;\mathrm{e}^{\mathrm{i}\chi_1} + r r r\,\psi_0\;\mathrm{e}^{\mathrm{i}\chi_2}\right|^2 \tag{5.19}$$

and

$$I_{\mathrm{H}} = |\psi_0|^2\left(\alpha^2|t|^4|r|^2 + |r|^6\right) - A\,\alpha\,C\,\cos\chi = B_{\mathrm{I}} + B_{\mathrm{II}} - A\,\alpha\,C\,\cos\chi\,, \tag{5.20}$$

with different contributions for paths I and II, signified by the parameters B_{I} and B_{II}, which again shows the fundamental asymmetry of the MZI - for the O beam, both paths contribute equally ($A_{\mathrm{I}} = A_{\mathrm{II}}$). With $d = 0 \Rightarrow \alpha = 1$, these intensities take the form of eq. (2.18) which has already been discussed in SEC. 2.2.1.1. The absorber is only present after the first interferometer plate (region 2−), thus α has to be considered only for the first transmission.

From eq. (5.18), the contrast in presence of an absorber can be calculated as

$$C_d(\alpha) = \frac{2\,\alpha\,C}{1+\alpha^2}\,, \tag{5.21}$$

which results in $C_{1\,\mathrm{mm}} = 0.746$ and $C_{3\,\mathrm{mm}} = 0.468$ and differs from the contrast values in TAB. 5.2: $C_{1\,\mathrm{mm}} = 0.748$ and $C_{3\,\mathrm{mm}} = 0.375$. In other words, these measured contrast values correspond to an In foil thickness d of 0.998 mm and 3.74 mm, respectively.

With the neutron counts from the C_{32} measurements (see TAB. 5.5) for the case where no In absorber is present as well as the typical initial interferometric contrast of $C = 80\,\%$, one obtains for a measuring time of 60 s $B_\mathrm{I} = 3800$, $B_\mathrm{II} = 5800$, $A_\mathrm{I} = A_\mathrm{II} = 2500$, and the detected intensities become

$$\begin{aligned} I_\mathrm{O}(60\,\mathrm{s}, \alpha = 0) &= 5000\ (1 + 0.8\ \cos\chi) \\ I_\mathrm{H}(60\,\mathrm{s}, \alpha = 0) &= 9600\ - 4000\ \cos\chi\,. \end{aligned} \tag{5.22}$$

The resulting curves are shown in FIG. 5.14. Using the macroscopic cross section for indium $\Sigma = 7.43\,\mathrm{cm}^{-1}$ (discussed in SEC. 2.1.4.2), the resulting curves for an absorber of thickness 1 mm and 3 mm are shown in FIG. 5.15 and FIG. 5.16, respectively. For both these cases, the simulation curve (eq. (5.22)) has to be multiplied by a factor of three to account for the triple measuring time. For 1 mm In, measured and simulated curves are in good agreement, while a slightly larger discrepancy is observed for 3 mm In. This is due to the fact that the thickness of the used In foil is not precisely determined.

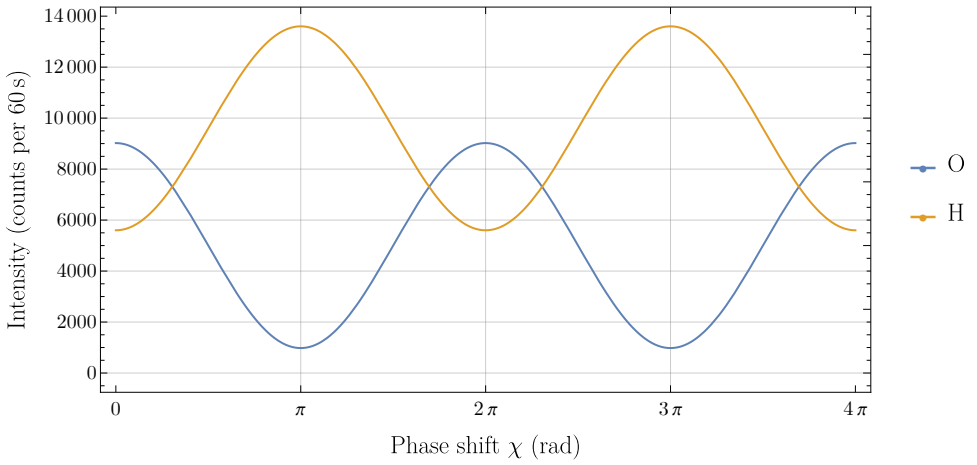

FIG. 5.14 – Simulation of an interferogram with no absorber present. Blue denotes the O detector, orange the H detector.

From these curves, the correlator C_{31} can be determined. The maximum value (and maximum violation of the LGI) is achieved at π, giving

$$C_{31}(A_\mathrm{I}, A_\mathrm{II}, B_\mathrm{I}, B_\mathrm{II}, \alpha, C, \chi) = \frac{I_\mathrm{O}(\pi) - I_\mathrm{H}(\pi)}{I_\mathrm{O}(\pi) + I_\mathrm{H}(\pi)}\,, \tag{5.23}$$

with $I_\mathrm{O}(\pi) = I_\mathrm{O}(A_\mathrm{I}, A_\mathrm{II}, B_\mathrm{I}, B_\mathrm{II}, \alpha, C, \pi)$ and likewise for I_H, as given in eq. (5.18) and eq. (5.20). The results of the simulated C_{31} in comparison to the directly measured values are shown in TAB. 5.7.

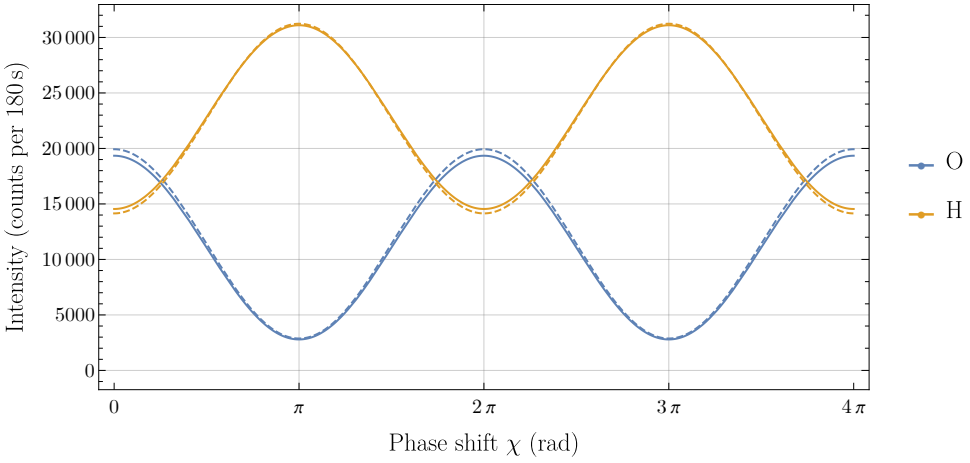

FIG. 5.15 – Simulation (solid) and measurement (dashed) of an interferogram with 1 mm In in path I. Blue curves denote the O detector, orange the H detector.

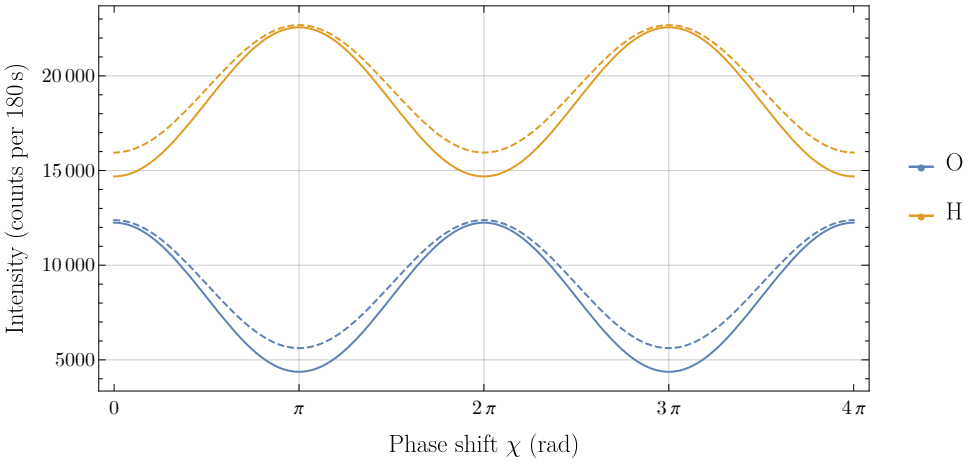

FIG. 5.16 – Simulation (solid) and measurement (dashed) of an interferogram with 3 mm In in path I. Blue curves denote the O detector, orange the H detector.

TAB. 5.7 – Comparison of the simulated and measured correlator C_{31} for different thickness d of the In absorber.

d	C_{31} simulated	C_{31} measured
–	-0.863	-0.863 ± 0.004
1 mm	-0.835	-0.831 ± 0.003
3 mm	-0.675	-0.603 ± 0.005

The correlator C_{32} is calculated as

$$C_{32}(A_\mathrm{I}, A_\mathrm{II}, B_\mathrm{I}, B_\mathrm{II}, \alpha) = -\frac{A_\mathrm{I}\alpha^2 - B_\mathrm{I}\alpha^2 - A_\mathrm{II} + B_\mathrm{II}}{A_\mathrm{I}\alpha^2 + B_\mathrm{I}\alpha^2 + A_\mathrm{II} + B_\mathrm{II}}\,, \tag{5.24}$$

and the resulting comparison of simulated and measured values is presented in TAB. 5.8. Since the neutron counts from this measurement were used to calculate the intensities I_{detector}, the accordance is expected. The deviations are due to rounding errors and the thickness of the In foil which is not sufficiently precisely determined, and grow with increasing In thickness d.

TAB. 5.8 – Comparison of the simulated and measured correlator C_{32} for different thickness d of the In absorber.

d	C_{32} simulated	C_{32} measured
–	-0.137	-0.131 ± 0.008
1 mm	-0.237	-0.229 ± 0.009
3 mm	-0.352	-0.343 ± 0.002

To determine the correlator C_{21}, another measurement is needed. For this, the raster scan of the setup without In at a measuring time of 10 s (shown in FIG. 5.6) is used, giving $N_{2+1+} = 1400$ and $N_{2-1+} = 1060$. The correlator is calculated as follows

$$C_{21} = \frac{N_{2+1+} - N_{2-1+}\alpha^2}{N_{2+1+} + N_{2-1+}\alpha^2}, \tag{5.25}$$

and the results are shown in TAB. 5.9. The slight rounding error accounts for the discrepancies between the measured and simulated value for the setup without In absorber.

TAB. 5.9 – Comparison of the simulated and measured correlator C_{21} for different thickness d of the In absorber.

d	C_{21} simulated	C_{21} measured
–	0.138	0.139 ± 0.020
1 mm	0.470	0.495 ± 0.011
3 mm	0.849	0.903 ± 0.002

Finally, the combination of the previous results and calculation of the the Leggett–Garg parameter $K = C_{21} + C_{32} - C_{31}$ is presented in TAB. 5.10. The values for K differ slightly, but the overall behaviour clearly shows that a violation of eq. (5.1) is not possible without an absorber, while it is observed for both 1 mm and 3 mm In absorbers.

TAB. 5.10 – Comparison of the simulated and measured Leggett–Garg parameter K for different thickness d of the In absorber.

d	K simulated	K measured
–	0.864	0.871 ± 0.022
1 mm	1.068	1.097 ± 0.014
3 mm	1.173	1.162 ± 0.006

A density plot for the areas in which a violation can be achieved is shown in FIG. 5.17: The smaller the initial contrast, the smaller the possible transmission of the In in path I (i.e. a larger thickness d is needed) where a violation of the LGI is still possible. Higher initial contrast allows

for LGI violations with smaller values of d. The neutron counts used in this simulation are still the ones described above, from measurements of C_{32} and C_{21}. The dashed line corresponds to $K = 1$, the classical limit of the LGI.

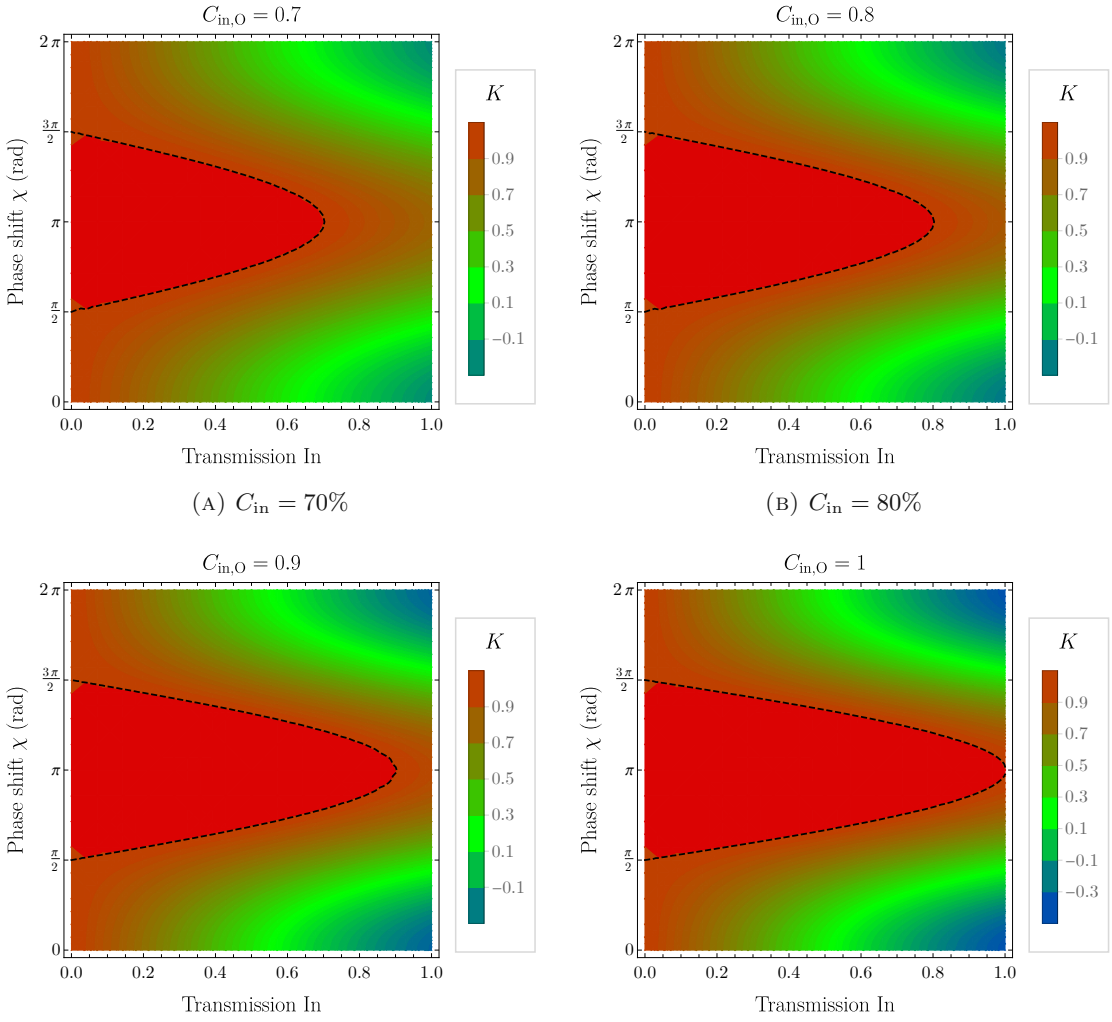

(A) $C_{\text{in}} = 70\%$ (B) $C_{\text{in}} = 80\%$

(C) $C_{\text{in}} = 90\%$ (D) $C_{\text{in}} = 100\%$

FIG. 5.17 – For different values of the initial contrast in the O beam, the resulting values of the K parameter are shown (red to green to blue). The solid red area to the left, separated by a dashed curve, denotes the area in which the LGI is violated, i.e. K reaches values greater than 1.

5.2.6 Visualisation of the probability amplitudes

For the measurements with In in path I, the diminution of the contrast due to the presence of the absorber has to be taken into account, which can be compensated by increasing the respective measuring times. This chapter discusses the situation for the O detector, where the contributions to paths I and II are equal when no absorber is present (two reflections r and one transmission t in each path). A useful visualisation tool is the Bloch sphere FIG. 5.18.

Paths I and II constitute the eigenstates $|\mathrm{I}\rangle$, $|\mathrm{II}\rangle$ of the two-level system, and are located at the poles of the Bloch sphere. Measurement takes place in the xy plane, and a superposition of the two possible neutron paths is recorded. Each state on the Bloch sphere can be described as

$$|\psi\rangle = c_\mathrm{I}\,|\mathrm{I}\rangle + c_\mathrm{II}\,|\mathrm{II}\rangle = \cos\frac{\vartheta}{2}\,|\mathrm{I}\rangle + \mathrm{e}^{\mathrm{i}\chi}\sin\frac{\vartheta}{2}\,|\mathrm{II}\rangle\ , \tag{5.26}$$

or

$$\vec{a} = \begin{pmatrix} r\sin\vartheta\cos\chi \\ r\sin\vartheta\sin\chi \\ r\cos\vartheta \end{pmatrix}\ , \tag{5.27}$$

with radius $r = 1$, polar angle ϑ and azimuthal angle χ. This χ represents the phase shift between the partial waves in the interferogram. Without an absorber (FIG. 5.18A), both paths contribute equally, with the orange Bloch vector

$$|\psi\rangle = \frac{1}{\sqrt{2}}\,|\mathrm{I}\rangle + \frac{1}{\sqrt{2}}\,\mathrm{e}^{\mathrm{i}\chi}\,|\mathrm{II}\rangle \tag{5.28}$$

or

$$\vec{a} = \begin{pmatrix} \cos\chi \\ \sin\chi \\ 0 \end{pmatrix}\ , \tag{5.29}$$

precessing along the dashed orange line, the equator of the Bloch sphere. In the presence of an absorber in path I however, the partial wave ψ_I collects an additional factor $\alpha = \mathrm{e}^{-\frac{1}{2}\Sigma d}$ (see eq. (5.17)), which changes both the length and the angle ϑ of the Bloch vector. The length changes to

$$r(\alpha) = \sqrt{\frac{1}{2}\left(1+\alpha^2\right)}\,, \tag{5.30}$$

and the new polar angle is

$$\vartheta(\alpha) = 2\arccos\left(\frac{\alpha}{\sqrt{2}}\right)\ . \tag{5.31}$$

This situation is shown in FIG. 5.18B. Grey arrow and dashed grey circle at the equator of the Bloch sphere show the case without an absorber for reference. For the two absorbers used during measurements for this thesis, 1 mm In and 3 mm In in path I, the resulting Bloch vectors are shown in orange, and their respective precession circles indicated by the dashed orange line. The reduction in interferometric contrast is due to both the diminished length of the Bloch vector (which does not end on the surface of the Bloch sphere), as well as its projection on the xy plane. The red arrow shows the case for a completely blocked path I: no interference fringes can be observed (the angle χ does not play a role in the vector position since $\vartheta = \pi$ and therefore $\sin\vartheta = 0$), and the total intensity is half the original intensity.

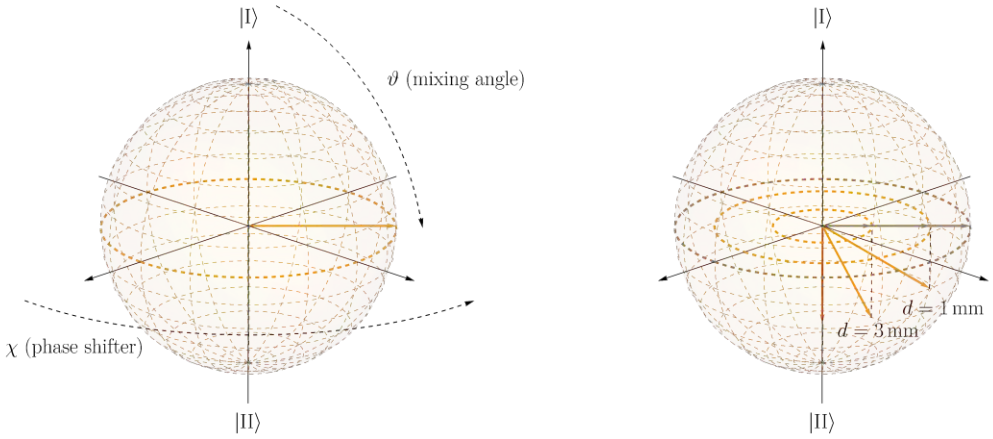

(A) Without absorber. (B) With In absorber of thickness d in path I.

FIG. 5.18 – Bloch sphere.(A) Without absorber, $|\mathrm{I}\rangle$ and $|\mathrm{II}\rangle$ contribute equally. The superposition (orange arrow) precesses in the xy plane (dashed orange line). (B) With absorber, the precession circles of the projection (dashed black lines) of the Bloch vectors (orange arrows) onto the xy plane are smaller than the original (absorber-less) case. The resulting Bloch vectors for an In foil of 1 mm and 3 mm in path I, as well as for a completely blocked path I (red arrow) are shown.

6 Conclusion

Based on the use of arrival time postselection for contrast enhancement and reduction of phase uncertainty in neutron interferometry by Zawisky et al. [36], their setup at the Atominstitut in Vienna has been expanded and improved. In addition to the O beam (transmitted direction), this thesis used the H beam as well, both with pencil ^{3}He detectors whose smaller volume (compared to the old BF_3 barrel detectors) along with the implementation of a 40 MHz FPGA card for data processing allowed for a more accurate determination of neutron arrival times. Steps to reduce vibrations of the setup were taken by rebuilding to uncouple the phase shifter and its stepper motor from the optical bench. This resulted in an increase to the initial contrast from 40 % to almost 70 % for the O detector, and from 22 % to over 40 % for the H detector.

These measurements were then repeated at the Institut Laue–Langevin (ILL) in Grenoble, where higher count rates allowed a more in-depth study of the behaviour of the contrast with the selection of neutron arrival times. The initial contrast of 82 % for the O beam could be raised to over 97 % while still retaining over 40 % of the recorded data.

Since the recording of these measurements, more improvements to the setup in Vienna were made, and new translation stages for the O and H collimators were installed in 2020.

Furthermore, the violation of a Leggett–Garg inequality (LGI) was measured at the ILL. Macrorealism and non-invasive measurability are quantified with the Leggett–Garg parameter $K \leq 1$, and a violation shows the quantum mechanical nature of the neutron interferometer. Ideal negative measurements were used, as well as an In absorber in one of the partial beams inside the interferometer to realise a non-50:50 beam splitter with the first plate. With an In foil of 1 mm thickness, K resulted in 1.097 ± 0.014, which is a violation of over $7\,\sigma$, and with 3 mm In foil, $K = 1.162 \pm 0.006$, a clear violation of more than $28\,\sigma$.

Appendix

A Additional calculations

A.1 Beam intensities in the neutron interferometer

In order to derive eq. (2.14), it is first necessary to look at the action of a single 50:50 beam splitter in the interferometer with two input modes with amplitudes a_1, a_2 and two output modes with amplitudes a_1', a_2'. This situation is depicted in FIG. A.1.

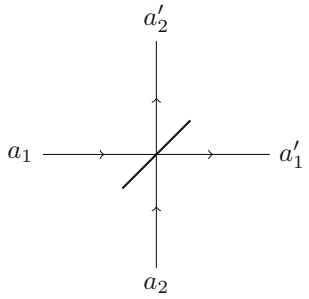

FIG. A.1 – Schematic of a single beam splitter. The amplitudes of the two input modes are denoted a_1, a_2, output modes a_1', a_2'.

The action of the beam splitter can be described as [68, pp. 103–105]

$$\begin{pmatrix} a_1' \\ a_2' \end{pmatrix} = \begin{pmatrix} t_1 & r_2 \\ r_1 & t_2 \end{pmatrix} \begin{pmatrix} a_1 \\ a_2 \end{pmatrix} , \tag{A.1}$$

with a unitary transformation matrix. Due to conservation of energy in a lossless beam splitter, the following identity has to hold:

$$\begin{aligned} |a_1|^2 + |a_2|^2 &= (t_1 a_1' + r_2 a_2') (t_1 a_1' + r_2 a_2')^* + (r_1 a_1' + t_2 a_2') (r_1 a_1' + t_2 a_2')^* \\ &= \left(|t_1|^2 + |r_1|^2\right) |a_1'|^2 + \left(|t_2|^2 + |r_2|^2\right) |a_2'|^2 + a_1' a_2'^* \left(t_1 r_2^* + r_1 t_2^*\right) + a_1'^* a_2' \left(t_1^* r_2 + r_1^* t_2\right) \\ &\stackrel{!}{=} |a_1'|^2 + |a_2'|^2 . \end{aligned} \tag{A.2}$$

Comparison of coefficients yields the following relations

$$\begin{aligned} |t_1|^2 + |r_1|^2 &= 1 \\ |t_2|^2 + |r_2|^2 &= 1 \\ t_1 r_2^* + r_1 t_2^* &= 0 \\ t_1^* r_2 + r_1^* t_2 &= 0\,. \end{aligned} \tag{A.3}$$

With the choice of $r_1 = r_2 = r$ and $t_1 = t_2 = t$, this becomes

$$\begin{aligned} |t|^2 + |r|^2 &= 1 \\ r t^* &= -r^* t\,, \end{aligned} \tag{A.4}$$

which can now be used to derive eq. (2.14). For the intensity in the O beam, one starts from eq. (2.12),

$$\begin{aligned} I_\mathrm{O} &= \left| trr\,\psi_0\, \mathrm{e}^{\mathrm{i}\chi_1} + rrt\,\psi_0\, \mathrm{e}^{\mathrm{i}\chi_2} \right|^2 \\ &= |\psi_0|^2 |t|^2 |r|^4 \left| \mathrm{e}^{\mathrm{i}\chi_1} + \mathrm{e}^{\mathrm{i}\chi_2} \right|^2 . \end{aligned} \tag{A.5}$$

With the definition $\chi = \chi_2 - \chi_1$,

$$\begin{aligned} \left| \mathrm{e}^{\mathrm{i}\chi_1} + \mathrm{e}^{\mathrm{i}\chi_2} \right|^2 &= \mathrm{e}^{\mathrm{i}\chi_1}\,\mathrm{e}^{-\mathrm{i}\chi_1} + \mathrm{e}^{-\mathrm{i}\chi_1}\,\mathrm{e}^{\mathrm{i}\chi_2} + \mathrm{e}^{\mathrm{i}\chi_1}\,\mathrm{e}^{-\mathrm{i}\chi_2} + \mathrm{e}^{\mathrm{i}\chi_2}\,\mathrm{e}^{-\mathrm{i}\chi_2} \\ &= 1 + \mathrm{e}^{\mathrm{i}(\chi_2-\chi_1)} + \mathrm{e}^{-\mathrm{i}(\chi_2-\chi_1)} + 1 \\ &= 2 + 2\cos\chi\,, \end{aligned} \tag{A.6}$$

and eq. (A.5) becomes

$$I_\mathrm{O} = \underbrace{2\,|\psi_0|^2 |t|^2 |r|^4}_{A}\,(1 + \cos\chi)\,. \tag{A.7}$$

For the H beam intensity, eq. (2.13),

$$\begin{aligned} I_\mathrm{H} &= \left| trt\,\psi_0\, \mathrm{e}^{\mathrm{i}\chi_1} + rrr\,\psi_0\, \mathrm{e}^{\mathrm{i}\chi_2} \right|^2 \\ &= |\psi_0|^2 |r|^2 \left| tt\,\mathrm{e}^{\mathrm{i}\chi_1} + rr\,\mathrm{e}^{\mathrm{i}\chi_2} \right|^2 . \end{aligned} \tag{A.8}$$

Using again the definition $\chi = \chi_2 - \chi_1$, as well as eq. (A.4),

$$\begin{aligned} \left| tt\,\mathrm{e}^{\mathrm{i}\chi_1} + rr\,\mathrm{e}^{\mathrm{i}\chi_2} \right|^2 &= |t|^4 + |r|^4 + ttr^*r^*\,\mathrm{e}^{-\mathrm{i}(\chi_2-\chi_1)} + t^*t^*rr\,\mathrm{e}^{\mathrm{i}(\chi_2-\chi_1)} \\ &= |t|^4 + |r|^4 - 2|t|^2|r|^2\cos\chi\,, \end{aligned} \tag{A.9}$$

resulting in

$$I_\mathrm{H} = \underbrace{|\psi_0|^2\left(|t|^4|r|^2 + |r|^6\right)}_{B} - \underbrace{2\,|\psi_0|^2|t|^2|r|^4}_{A}\cos\chi\,. \tag{A.10}$$

With the addition of a neutron absorber in one of the paths to realise a non-50:50 beam splitter, these beam intensities are discussed in SEC. 5.2.5.

A.2 Reflection curves for a Mach–Zehnder neutron interferometer

For dynamical diffraction theory, it is useful to define two new unitless parameters (presented here without further introduction): A for the characterisation of the plate thickness D in the interferometer, and y to quantify the deviation from the Bragg angle. This discussion is valid for the Laue case, without a phase shifter in the interferometer, and when absorption by the interferometer plates is neglected. More detailed descriptions of dynamical diffraction theory in neutron interferometry can be found in [30, 37], where this chapter is taken from, and [69].

The ratio of the intensity $I = |\psi|^2$ for reflected ψ_r to incoming beam ψ_{in} for a single plate can be written as

$$\frac{I_r}{I_{\text{in}}} = \frac{\sin^2(A\sqrt{1+y^2})}{1+y^2} \tag{A.11}$$

with zeroes at $A\sqrt{1+y^2} = n\pi$. This is called Pendellösung (German for 'pendulum solution'), because the intensity oscillates (German: 'pendelt') between the O and H directions. The central maximum for $y = 0$ lies at $A = \pi$, and allows the definition of the Pendellösung period,

$$\Delta_0 = \pi\frac{D}{A}\,, \tag{A.12}$$

which is about 6×10^{-2} mm for $\lambda = 2$ Å for the $\{2, 2, 0\}$ reflection in the symmetric Laue case [30]. The plate thickness of the used interferometer is $D = 3\,\text{mm} \gg \Delta_0$, so that we can take the average of the sine function (thick crystal approximation). Because the number of particles has to be conserved, the intensity ratio for the transmitted beam ψ_t is

$$\frac{I_t}{I_{\text{in}}} = 1 - \frac{\sin^2(A\sqrt{1+y^2})}{1+y^2}\,, \tag{A.13}$$

and, with $\langle\sin^2(\cdot)\rangle$, the averaged curves are

$$\begin{aligned} \langle I_r(y)\rangle &= \frac{1}{2}\frac{1}{1+y^2} \\ \langle I_t(y)\rangle &= 1 - \frac{1}{2}\frac{1}{1+y^2}\,, \end{aligned} \tag{A.14}$$

using the shorthand $\langle I\rangle = \langle I/I_{\text{in}}\rangle$. In FIG. A.2 the resulting intensities for two slightly different thin crystals (blue and orange curves), as well as the averaged function for a thick crystal (dashed curve) are shown. The reflectivity is defined as the area beneath the reflection curve,

$$R = \int_{-\infty}^{\infty} \frac{I_r(y)}{I_{\text{in}}(y)}\,\mathrm{d}y\,. \tag{A.15}$$

In the Triple-Laue (LLL) interferometer, both partial waves for the O beam are reflected twice and transmitted once (rrt), resulting in

$$I_{\text{O,I}}(y) = I_{\text{O,II}}(y) = \frac{\sin^4(A\sqrt{1+y^2})}{(1+y^2)^2}\left(1 - \frac{\sin^2(A\sqrt{1+y^2})}{1+y^2}\right)\,, \tag{A.16}$$

with the average

$$\langle I_{\text{O,I}}\rangle = \langle I_{\text{O,II}}\rangle = \frac{1+6y^2}{16\,(1+y^2)^3}\,. \tag{A.17}$$

This again uses the shorthand I for I/I_{in}. For the H beam, however, path I is reflected three times (rrr), while path II is reflected once and transmitted twice (rtt), giving

$$\begin{aligned} I_{\mathrm{H,I}}(y) &= \frac{\sin^6(A\sqrt{1+y^2})}{(1+y^2)^3} \\ I_{\mathrm{H,II}}(y) &= \frac{\sin^2(A\sqrt{1+y^2})}{1+y^2}\left(1-\frac{\sin^2(A\sqrt{1+y^2})}{1+y^2}\right)^2 \end{aligned} \tag{A.18}$$

with the averages

$$\begin{aligned} \langle I_{\mathrm{H,I}}(y)\rangle &= \frac{8y^4+4y^2+1}{16\,(1+y^2)^3} \\ \langle I_{\mathrm{H,II}}(y)\rangle &= \frac{5}{16\,(1+y^2)^3} \end{aligned} \tag{A.19}$$

Curves for two different (thin) plates (blue and orange) and their respective averages (thick crystal; dashed) for the three different partial beams (since for O, the contributions from path I and II are the same) are shown in FIG. A.3.

The overall intensity in the interferometer is $I_{\mathrm{ifm}} = I_{\mathrm{O}} + I_{\mathrm{H}}$, with

$$I_{\mathrm{O}} = |\psi_{\mathrm{O}}|^2 = |\psi_{\mathrm{O,I}} + \psi_{\mathrm{O,II}}|^2 = |2\psi_{\mathrm{O,I}}|^2 = 4\,|\psi_{\mathrm{O,I}}|^2 \tag{A.20}$$

and, with consideration of the phase shift π between the two partial beams in H due to the different number of reflections,

$$I_{\mathrm{H}} = |\psi_{\mathrm{H}}|^2 = \frac{\sin^2(A\sqrt{1+y^2})}{1+y^2}\left(1-2\,\frac{\sin^2(A\sqrt{1+y^2})}{1+y^2}\right)^2, \tag{A.21}$$

giving the averages

$$\begin{aligned} \langle I_{\mathrm{O}}(y)\rangle &= \frac{1+6y^2}{4\,(1+y^2)^3} \\ \langle I_{\mathrm{H}}(y)\rangle &= \frac{2y^4-2y^2+1}{4\,(1+y^2)^3} \\ \langle I_{\mathrm{ifm}}(y)\rangle &= \frac{1}{2}\,\frac{1}{1+y^2}\,. \end{aligned} \tag{A.22}$$

The resulting curves are shown in FIG. A.4 for the empty interferometer as well as with path I or path II blocked. Contributions of the O beam are shown in blue, orange for the H beam, and the total intensity for both beams is shown in green. Note that the overall intensity in the interferometer is lower when path II is blocked than when path I is blocked – this is due to the much-discussed asymmetry of the beam paths.

Integrating over the curves in eq. (A.17) and eq. (A.19), as well as eq. (A.22) gives the respective reflectivities which are shown above in TAB. 2.2 (SEC. 2.2.1.2), normalised to the total reflectivity

$$R_{\mathrm{ifm}} = \int_{-\infty}^{\infty} \frac{1}{2}\,\frac{1}{1+y^2}\,\mathrm{d}y = \frac{\pi}{2}\,. \tag{A.23}$$

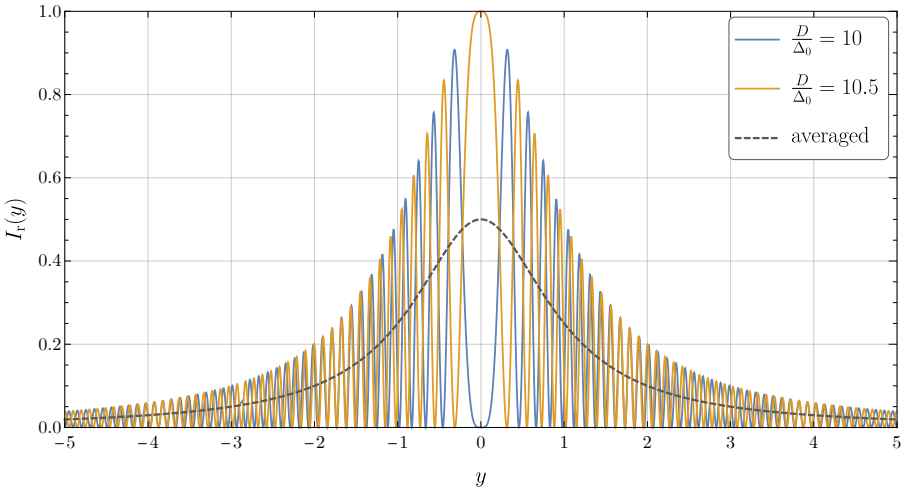

(A) Single reflection.

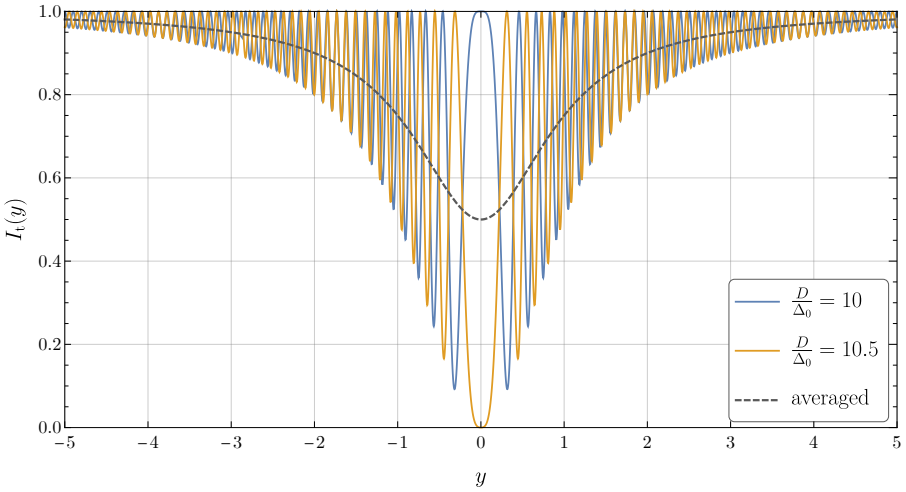

(B) Single transmission.

FIG. A.2 – Pendellösung for varying plate thickness A with the dashed line indicating the resulting average (thick crystal), and the blue and orange curves illustrating the difference in a small variation of the plate thickness, normalised to the incoming intensity for a single (A) reflection and (B) transmission.

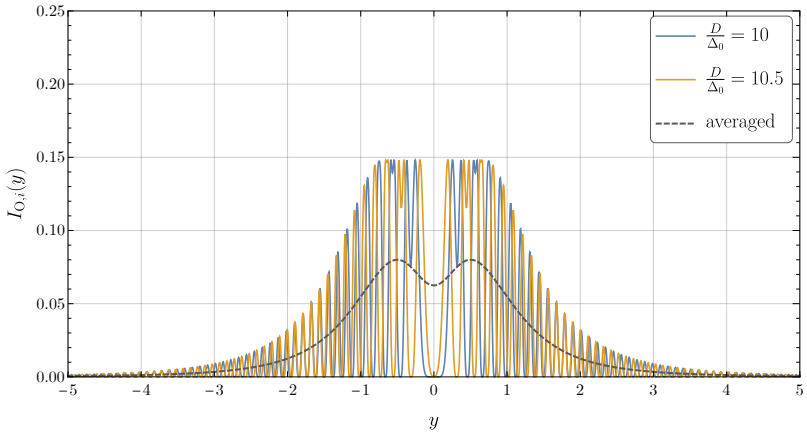

(A) Partial beam $O_{I,II}$.

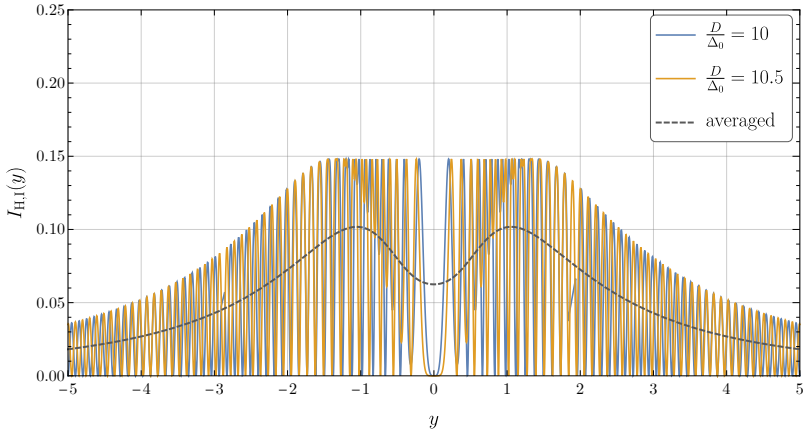

(B) Partial beam H_I.

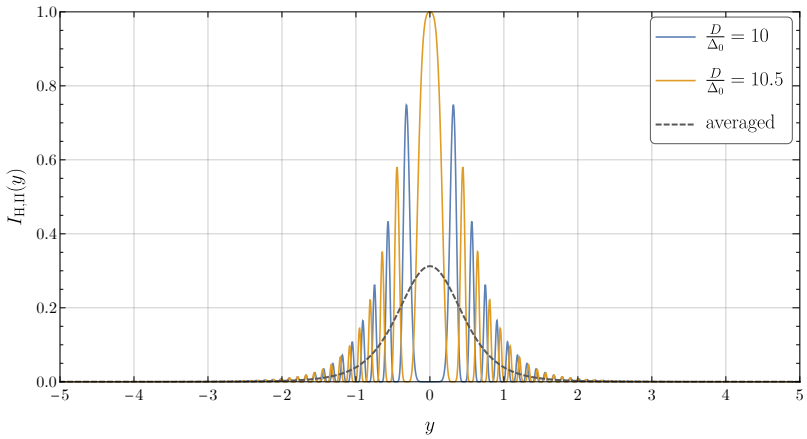

(C) Partial beam H_{II}.

FIG. A.3 – Intensities in the O and H detector partial beams for a small variation in the plate thickness (blue and orange curves). The dashed line indicates the averaged function (thick crystal). (A) O detector: partial beams for paths I and II are equal (*rrt*). (B) Partial beam for path I in the H detector (*trt*) and (C) Partial beam for path II in the H detector (*rrr*) – due to the asymmetry in the beam paths, these two contributions are not equal.

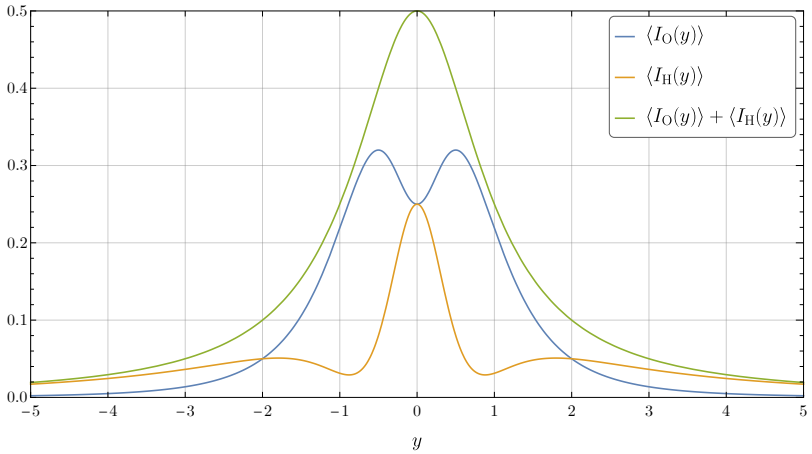

(A) Empty interferometer.

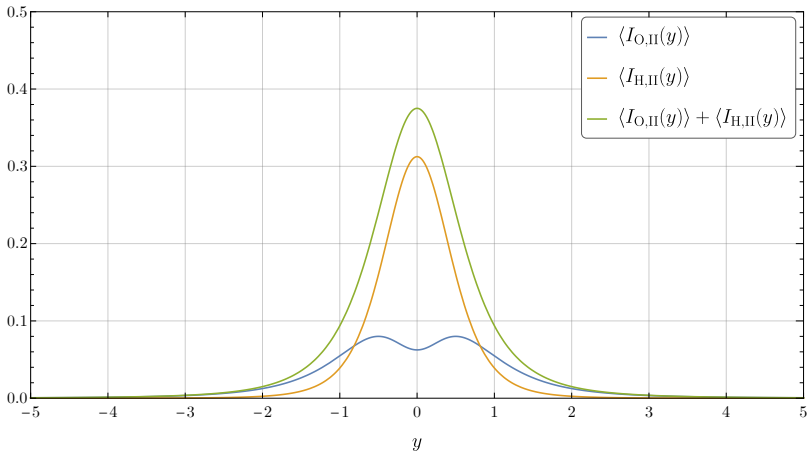

(B) Path I blocked.

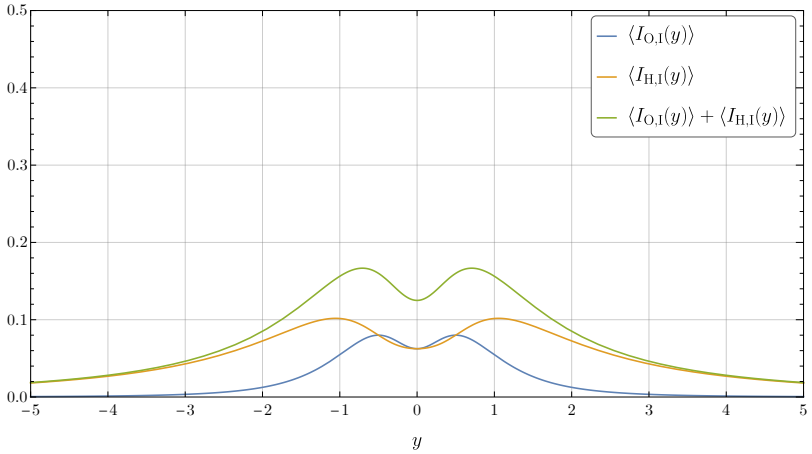

(C) Path II blocked.

FIG. A.4 – Reflection curves for an ideal empty interferometer with contrast $C = 1$. Blue denotes the intensity for the O detector, orange for the H detector, and green the sum of both detectors. (A) Empty interferometer. (B) With blocked path I. (C) With blocked path II.

List of Figures

List of Tables

Bibliography

[1] J. Chadwick. 'Possible Existence of a Neutron'. In: *Nature* **129** (1932), p. 312. doi: 10.1038/129312a0.

[2] H. Rauch, W. Treimer and U. Bonse. 'Test of a single crystal neutron interferometer'. In: *Physics Letters A* **47.5** (1974), pp. 369–371. doi: 10.3390/atoms4010011.

[3] H. Rauch et al. 'Verification of coherent spinor rotation of fermions'. In: *Physics Letters A* **54.6** (1975), pp. 425–427. doi: https://doi.org/10.1016/0375-9601(75)90798-7.

[4] G. Badurek, H. Rauch and J. Summhammer. 'Time-Dependent Superposition of Spinors'. In: *Phys. Rev. Lett.* **51** (1983), pp. 1015–1018. doi: 10.1103/PhysRevLett.51.1015.

[5] J. Summhammer et al. 'Direct observation of fermion spin superposition by neutron interferometry'. In: *Phys. Rev. A* **27** (1983), pp. 2523–2532. doi: 10.1103/PhysRevA.27.2523.

[6] H. Rauch and S. A. Werner. 'Neutron Interferometry. Lessons in Experimental Quantum Mechanics, Wave-Particle Duality, and Entanglement'. 2nd ed. Oxford University Press (2015).

[7] S. A. Werner, R. Colella, A. W. Overhauser and C. F. Eagen. 'Observation of the Phase Shift of a Neutron Due to Precession in a Magnetic Field'. In: *Phys. Rev. Lett.* **35** (1975), pp. 1053–1055. doi: 10.1103/PhysRevLett.35.1053.

[8] U. Bonse and T. Wroblewski. 'Measurement of Neutron Quantum Interference in Noninertial Frames'. In: *Phys. Rev. Lett.* **51** (1983), pp. 1401–1404. doi: 10.1103/PhysRevLett.51.1401.

[9] R. Colella, A. W. Overhauser and S. A. Werner. 'Observation of Gravitationally Induced Quantum Interference'. In: *Phys. Rev. Lett.* **34** (1975), pp. 1472–1474. doi: 10.1103/PhysRevLett.34.1472.

[10] Y. Aharonov, D. Z. Albert and L. Vaidman. 'How the result of a measurement of a component of the spin of a spin-1/2 particle can turn out to be 100'. In: *Phys. Rev. Lett.* **60** (1988), pp. 1351–1354. doi: 10.1103/PhysRevLett.60.1351.

[11] S. Sponar et al. 'Weak values obtained in matter-wave interferometry'. In: *Phys. Rev. A* **92** (2015), p. 062121. doi: 10.1103/PhysRevA.92.062121.

[12] R. Wagner et al. 'Direct experimental test of commutation relation via imaginary weak value'. In: *Phys. Rev. Research* **3** (2021), p. 023243. doi: 10.1103/PhysRevResearch.3.023243.

[13] H. Lemmel et al. 'Quantifying the presence of a neutron in the paths of an interferometer'. In: *Phys. Rev. Research* **4** (2022), p. 023075. DOI: 10.1103/PhysRevResearch.4.023075.

[14] T. Denkmayr et al. 'Observation of a quantum Cheshire Cat in a matter-wave interferometer experiment'. In: *Nature Communications* **5** (2014), p. 4492. DOI: 10.1038/ncomms5492.

[15] H. Lemmel et al. 'Neutron interference from a split-crystal interferometer'. In: *Journal of Applied Crystallography* **55.4** (2022), pp. 870–875. DOI: 10.1107/S1600576722006082.

[16] A. J. Leggett and A. Garg. 'Quantum mechanics versus macroscopic realism: Is the flux there when nobody looks?' In: *Phys. Rev. Lett.* **54** (1985), pp. 857–860. DOI: 10.1103/PhysRevLett.54.857.

[17] A. Garg. 'Experimental tests of macrorealism: an assessment'. In: *Current Science* **109.11** (2015), pp. 1958–1964. (Accessed on 06/08/2022).

[18] M. Tanabashi et al. (Particle Data Group). 'Review of Particle Physics'. In: *Phys. Rev. D* **98** (2018), p. 030001. DOI: 10.1103/PhysRevD.98.030001.

[19] E. Tiesinga, P. J. Mohr, D. B. Newell and B. N. Taylor. 'The 2018 CODATA Recommended Values of the Fundamental Physical Constants'. National Institute of Standards and Technology (2019).

[20] J. Byrne. 'Neutrons, Nuclei and Matter. An Exploration of the Physics of Slow Neutrons'. Dover Publications (2011).

[21] L. V. de Broglie. 'Recherches sur la théorie des quanta' (1924). English translation: J. W. Haslett. In: *Am. J. Phys.* **40** (1972), pp. 1315–1320.

[22] A. Furrer, J. Mesot and T. Strässle. 'Neutron Scattering in Condensed Matter Physics'. World Scientific (2009). DOI: 10.1142/4870.

[23] N. Carron. 'An Introduction to the Passage of Energetic Particles Through Matter'. CRC Press (Nov. 2006).

[24] R. Golub, D. Richardson and S. Lamoreaux. 'Ultra-Cold Neutrons'. Taylor & Francis (1991).

[25] K. Beckurts and K. Wirtz. 'Neutron Physics'. Springer (1964).

[26] M. Wang et al. 'The AME2016 atomic mass evaluation (II). Tables, graphs and references'. In: *Chin. Phys. C* **41.3** (2017), p. 030003. DOI: 10.1088/1674-1137/41/3/030003.

[27] A. Ziegler and H. Allelein. 'Reaktortechnik. Physikalisch-technische Grundlagen'. Springer (2013).

[28] European Spallation Source. URL: https://europeanspallationsource.se/ (accessed on 17/09/2019).

[29] G. Knoll. 'Radiation Detection and Measurement'. 3rd ed. Wiley (2000).

[30] D. Petrascheck and H. Rauch. 'Grundlagen für ein Laue-Neutroneninterferometer. Teil 1: Dynamische Beugung'. 3rd ed. AIAU 74405b (internal report). Atominstitut Wien (1976).

[31] W. M. Haynes, ed. 'CRC Handbook of Chemistry and Physics'. 95th ed. CRC Press, Taylor & Francis Group (2014).

[32] V. F. Sears. 'Neutron scattering lengths and cross sections'. In: *Neutron News* **3.3** (1992), pp. 26–37. DOI: 10.1080/10448639208218770.

[33] H. Geppert. 'Errichtung der Neutronen-Interferometer-Station am Atominstitut Wien'. Diploma thesis. Technische Universität Wien (2012).

[34] M. Hafner. 'Untersuchungen zur wechselwirkungsfreien Messung im Neutroneninterferometer'. Diploma thesis. Technische Universität Wien (1996).

[35] M. Zawisky. 'Die Phasenunschärfe im Neutroneninterferometer'. Diploma thesis. Technische Universität Wien (1987).

[36] M. Zawisky, H. Rauch and Y. Hasegawa. 'Contrast enhancement by time selection in neutron interferometry'. In: *Phys. Rev. A* **50** (1994), pp. 5000–5006. DOI: 10.1103/PhysRevA.50.5000.

[37] D. Petrascheck and H. Rauch. 'Grundlagen für ein Laue-Neutroneninterferometer. Teil 2: Theorie des Interferometers'. AIAU 76401 (internal report). Atominstitut Wien (1976).

[38] Y. Hasegawa et al. 'Violation of a Bell-like inequality in single-neutron interferometry'. In: *Nature* **425** (2003), pp. 45–8. DOI: 10.1038/nature01881.

[39] S. Sponar et al. 'Tests of fundamental quantum mechanics and dark interactions with low-energy neutrons'. In: *Nature Reviews Physics* **3** (2021), pp. 1–19. DOI: 10.1038/s42254-021-00298-2.

[40] S. Ross. 'Stochastic processes'. 2nd ed. Wiley series in probability and statistics: Probability and statistics. Wiley (1996).

[41] P. Bevington and D. Robinson. 'Data Reduction and Error Analysis for the Physical Sciences'. 3rd ed. McGraw-Hill Higher Education. McGraw-Hill Education (2003).

[42] R. J. Glauber. 'Photon statistics'. In: *Fundamental Problems in Statistical Mechanics II*. Edited by E. G. D. Cohen. North-Holland Publishing Company (1968), pp. 140–187.

[43] Technische Universität Wien - Atominstitut. 'Der TRIGA Mark-II Reaktor'. URL: https://ati.tuwien.ac.at/reaktor/ (accessed on 04/09/2019).

[44] M. C. Both. 'Aufbau eines vertikal fokussierenden Monochromators für die Interferometrie'. Diploma thesis. Technische Universität Wien (2010).

[45] Institut Laue–Langevin. 'Reactor and safety'. URL: https://www.ill.eu/reactor-and-safety/ (accessed on 26/09/2019).

[46] Institut Laue–Langevin. 'S18 instrument description'. URL: https://www.ill.eu/users/instruments/instruments-list/s18/characteristics/ (accessed on 04/09/2019).

[47] P. A. M. Dirac. 'Quantum theory of emission and absorption of radiation'. In: *Proc. Roy. Soc. Lond. A* **114** (1927), p. 243. DOI: 10.1098/rspa.1927.0039.

[48] P. Carruthers and M. M. Nieto. 'Phase and Angle Variables in Quantum Mechanics'. In: *Rev. Mod. Phys.* **40** (1968), pp. 411–440. DOI: 10.1103/RevModPhys.40.411.

[49] H. Rauch, J. Summhammer, M. Zawisky and E. Jericha. 'Low-contrast and low-counting-rate measurements in neutron interferometry'. In: *Phys. Rev. A* **42** (1990), pp. 3726–3732. DOI: 10.1103/PhysRevA.42.3726.

[50] M. Zawisky et al. 'Phase estimation in interferometry'. In: *Journal of Physics A: Mathematical and General* **31.2** (1998), pp. 551–564. DOI: 10.1088/0305-4470/31/2/015.

[51] Y. Hasegawa, M. Zawisky, H. Rauch and A. I. Ioffe. 'Geometric phase in coupled neutron interference loops'. In: *Phys. Rev. A* **53.4** (1996), pp. 2486–2492. DOI: 10.1103/PhysRevA.53.2486.

[52] M. Zawisky, J. Springer and H. Lemmel. 'High angular resolution neutron interferometry'. In: *Nuclear instruments & methods in physics research. Section A, Accelerators, spectrometers, detectors and associated equipment* **634** (2011), S46–S49. DOI: 10.1016/j.nima.2010.06.092.

[53] R. Haun et al. 'Precision Measurement of the Neutron Scattering Length of ^{4}He Using Neutron Interferometry'. In: *Phys. Rev. Lett.* **124** (2020), p. 012501. DOI: 10.1103/PhysRevLett.124.012501.

[54] W. E. Wallace, D. L. Jacobson, M. Arif and A. Ioffe. 'Application of neutron interferometry to the measurement of thin film density'. In: *Applied Physics Letters* **74.3** (1999), pp. 469–471. DOI: 10.1063/1.123038. eprint: https://doi.org/10.1063/1.123038.

[55] A. J. Leggett. 'Testing the limits of quantum mechanics: motivation, state of play, prospects'. In: *Journal of Physics: Condensed Matter* **14.15** (2002), R415–R451. DOI: 10.1088/0953-8984/14/15/201.

[56] C. Emary, N. Lambert and F. Nori. 'Leggett–Garg inequality in electron interferometers'. In: *Phys. Rev. B* **86** (2012), p. 235447. DOI: 10.1103/PhysRevB.86.235447.

[57] C. Emary, N. Lambert and F. Nori. 'Leggett–Garg inequalities'. In: *Reports on Progress in Physics* **77.1** (2013), p. 016001. DOI: 10.1088/0034-4885/77/1/016001.

[58] A. J. Leggett. 'Macroscopic Quantum Systems and the Quantum Theory of Measurement'. In: *Progress of Theoretical Physics Supplement* **69** (1980), pp. 80–100. DOI: 10.1143/PTP.69.80. eprint: https://academic.oup.com/ptps/article-pdf/doi/10.1143/PTP.69.80/5356381/69-80.pdf.

[59] A. Palacios-Laloy et al. 'Experimental violation of a Bell's inequality in time with weak measurement'. In: *Nature Physics* **6.6** (2010), pp. 442–447. DOI: 10.1038/nphys1641.

[60] A. K. Pan. 'Interference experiment, anomalous weak value, and Leggett–Garg test of macrorealism'. In: *Phys. Rev. A* **102** (2020), p. 032206. DOI: 10.1103/PhysRevA.102.032206.

[61] J. P. Groen et al. 'Partial-Measurement Backaction and Nonclassical Weak Values in a Superconducting Circuit'. In: *Phys. Rev. Lett.* **111** (2013), p. 090506. DOI: 10.1103/PhysRevLett.111.090506.

[62] V. Athalye, S. S. Roy and T. S. Mahesh. 'Investigation of the Leggett-Garg Inequality for Precessing Nuclear Spins'. In: *Phys. Rev. Lett.* **107** (2011), p. 130402. DOI: 10.1103/PhysRevLett.107.130402.

[63] A. M. Souza, I. S. Oliveira and R. S. Sarthour. 'A scattering quantum circuit for measuring Bell's time inequality: a nuclear magnetic resonance demonstration using maximally mixed states'. In: *New Journal of Physics* **13.5** (2011), p. 053023. DOI: 10.1088/1367-2630/13/5/053023.

[64] M. E. Goggin et al. 'Violation of the Leggett–Garg inequality with weak measurements of photons'. In: *Proceedings of the National Academy of Sciences* **108.4** (2011), pp. 1256–1261. DOI: 10.1073/pnas.1005774108. eprint: https://www.pnas.org/doi/pdf/10.1073/pnas.1005774108.

[65] J. Dressel, C. J. Broadbent, J. C. Howell and A. N. Jordan. 'Experimental Violation of Two-Party Leggett-Garg Inequalities with Semiweak Measurements'. In: *Phys. Rev. Lett.* **106** (2011), p. 040402. DOI: 10.1103/PhysRevLett.106.040402.

[66] G. C. Knee et al. 'Violation of a Leggett–Garg inequality with ideal non-invasive measurements'. In: *Nature Communications* **3** (2012), p. 606. DOI: 10.1038/ncomms1614.

[67] J. Kofler and Č. Brukner. 'Condition for macroscopic realism beyond the Leggett–Garg inequalities'. In: *Phys. Rev. A* **87** (2013), p. 052115. DOI: 10.1103/PhysRevA.87.052115.

[68] L. E. Ballentine. 'Quantum Mechanics'. Prentice Hall (1990).

[69] M. Suda. 'Quantum Interferometry in Phase Space. Theory and Applications'. Springer (2006).